Hydroclimate variations in the Caspian Sea region from the late Quaternary to the future

- A model perspective -

Sri Durgesh Nandini-weiß

Hydroclimate variations in the Caspian Sea region from the late Quaternary to the future

- A model perspective -

DISSERTATION

submitted in partial fulfilment of the requirements for the
Doctoral degree in Natural Sciences (Dr. rer. nat.) at the Department
of Geosciences at the University of Bremen

by

Sri Durgesh Nandini-weiß

MARUM - Center for Marine Environmental Sciences
and Faculty of Geosciences, University of Bremen

June 2019

Reviewers

Prof. Dr. Michael Schulz
MARUM and Faculty of Geosciences
University of Bremen

Prof. Dr. Martin Claussen
MPI, University of Hamburg

Date of colloquium: September 10, 2019

The research leading to this thesis has received funding from the European Union's Horizon 2020 research and innovation programme under the Marie Sklodowska-Curie grant agreement No 642973.

"Do not be intimidated by what you do not know. That can be your greatest strength and make sure you do things differently than anyone else."
Sara Blakely

Dedicated to my parents
and Thomas

Versicherung an Eides Statt / Affirmation in lieu of an oath

gem. § 5 Abs. 5 der Promotionsordnung vom 18.06.2018 /
according to § 5 (5) of the Doctoral Degree Rules and Regulations of 18 June, 2018

Ich / I, _____
(Vorname / First Name, Name / Name, Anschrift / Address, ggf. Matr.-Nr. / student ID no., ifapplicable)

versichere an Eides Statt durch meine Unterschrift, dass ich die vorliegende Dissertation selbständig und ohne fremde Hilfe angefertigt und alle Stellen, die ich wörtlich dem Sinne nach aus Veröffentlichungen entnommen habe, als solche kenntlich gemacht habe, mich auch keiner anderen als der angegebenen Literatur oder sonstiger Hilfsmittel bedient habe und die zu Prüfungszwecken beigelegte elektronische Version (PDF) der Dissertation mit der abgegebenen gedruckten Version identisch ist.
/ With my signature I affirm in lieu of an oath that I prepared the submitted dissertation independently and without illicit assistance from third parties, that I appropriately referenced any text or content from other sources, that I used only literature and resources listed in the dissertation, and that the electronic (PDF) and printed versions of the dissertation are identical.

Ich versichere an Eides Statt, dass ich die vorgenannten Angaben nach bestemWissen und Gewissen gemacht habe und dass die Angaben der Wahrheit entsprechen und ich nichts verschwiegen habe.
/ I affirm in lieu of an oath that the information provided herein to the best of my knowledge is true and complete.

Die Strafbarkeit einer falschen eidesstattlichen Versicherung ist mir bekannt, namentlich die Strafandrohung gemäß § 156 StGB bis zu drei Jahren Freiheitsstrafe oder Geldstrafe bei vorsätzlicher Begehung der Tat bzw. gemäß § 161 Abs. 1 StGB bis zu einem Jahr Freiheitsstrafe oder Geldstrafe bei fahrlässiger Begehung.
/ I am aware that a false affidavit is a criminal offence which is punishable by law in accordance with § 156 of the German Criminal Code (StGB) with up to three years imprisonment or a fine in case of intention, or in accordance with § 161 (1) of the German Criminal Code with up to one-year imprisonment or a fine in case of negligence.

_____ _____
Ort / Place, Datum / Date Unterschrift / Signature

Own contribution: The first study has been designed by the candidate and her supervisor. She and a co-author prepared new forcing data sets and performed eight model simulations. She has carried out all analysis, created all figures and interpretation of the model output data. Additionally, she has produced new modeling results for the late Quaternary period, that constraint the timings and identify the climate conditions favourable for major Caspian Sea transgressions and regressions in comparison with the geological reconstructions. This manuscript has been prepared by the candidate with contributions from all co-authors and is ready for submission in the Journal of Climate of the Past. The second study has been developed by the candidate with contributions from all co-authors. She has solely performed all five model simulations, as well as analysing all model outputs. She created new results to evaluate different model horizontal resolutions and model setups and identify the model that best represents the Caspian Sea climate, as well as presenting Caspian Sea levels under two new emission scenarios by 2100. The candidate prepared the manuscript and produced all figures (from the first draft to the final revised version resubmitted in the Journal of international Climatology) with contributions from all co-authors. In the third study, the candidate developed and changed the ocean and land component of the global earth system model to successfully generate four new surface areas of the Caspian Sea. She and a co-author designed four model simulations during a research stay at the University of Reading. As climate models do not include a correct Caspian Sea surface area, the new results generated from this study notably aid in evaluating model performance when including inaccurate CS surface area. The candidate and a co-author have carried out the model output analysis and prepared all figures. She has authored the manuscript as a first draft (in preparation for the Journal of Geophysical Research: Atmospheres). All co-authors contributed to revising the manuscript.

Abstract

The northern hemispheric glacial-interglacial climate states during the late Quaternary period drove Caspian Sea level (CSL) changes of up to ~150 m and can be used as an analogue for assessing present and future climate impacts. Geologic reconstructions of these paleo-lake levels and potential links with different climate events remain complex while future declines in modelled lake levels vary widely and are uncertain. The key drivers for such CSL include variations in the water budget balance between precipitation and evaporation (P-E). This thesis employs a climate modeling approach to investigate long-term changes in the Caspian Sea (CS) hydroclimate during different climate states from the late Quaternary to the end of the 21st century. The new results from the Community Earth System Model (CESM1.2.2), contribute to an improved interpretation of reconstructed paleo-lake levels with respect to changing P-E patterns and identify key drivers for future CSL changes. This study produced new modeling results for the late Quaternary period, that constrain the timings and identify the climate conditions favourable for major CS transgressions and regressions, in comparison with selected geological reconstructions; under three glacial (Marine Isotope 3 (MIS3), Last Glacial Maximum (LGM), Heinrich event 1 (H1)) and two interglacial (last interglacial (LIG) and early Holocene (EH)) climate states. The two interglacial climate states suggest favourable climate conditions (higher temperature and precipitation) for the CS that result in a positive water budget (LIG-P-E anomalies of 14.6 meter/1000 years and the EH-P-E anomalies ~5 meter/1000yr). The results propose a transgression was initiated by the summer large-scale and convective precipitation, triggered by enhanced summer insolation and the associated wind anomalies. The warmer and wetter MIS3 interstadial climate is identified as being responsible for a transgression with P-E anomalies of 16 meter/1000yr. The colder and drier LGM climate favours a regression with P-E of -12 meter/ 1000yr. These P-E anomalies and climate conditions agree with the reconstructions. However, our simulated P-E anomalies (for the H1); do not capture the magnitude of the reconstructed highstands during the deglaciation, and it is clear that meltwater into the CS is responsible for this highstand; and as our model does not include a sophisticated meltwater routing into the CS; hence comparisons with selected reconstructions remain complicated. This study also assessed different CESM horizontal resolutions and model setups to identify the best version that can represent the CS climate and climate modes of variability such as North Atlantic Oscillation (NAO) for the period 1850-2000 CE, as well as presenting new CSL under two new emission scenarios by the end of the 21st century. CESM1.2.2 with 1° CAM5 is identified as the best skill in simulating the NAO and its effects on CS catchment hydrology. Projections under the Representative Concentration Pathways RCP4.5 and RCP8.5 confirm the winter NAO remains the major winter variability with a significant impact on the Caspian catchment hydroclimate. However, under global warming, the evaporation over the sea is the key driver for a CSL decrease of about 9 m and 18 m between 2020 and 2100 for the RCP4.5 and RCP8.5 scenarios, respectively. The new CSL values are larger than previous projections of CSL, and include an overestimated total evaporation due to a larger CS surface area in CESM. Despite the clear

potential for this, current global climate models neglect to include accurate representations of CS area. This study generated new results to notably aid in evaluating the impacts of different CS surface areas on the regional and large-scale climate. Regionally, the presence of a larger CS area has a clear impact as higher evaporation over the sea and higher precipitation over the south-west catchment, while reducing (summer) and increasing (winter) surface air temperatures and vice versa for smaller CS area. Most importantly, this summer temperature disturbs the upper atmospheric circulation (at the 200 hPa and the 500 hPa level) with a southward shift and increase in speed of the summer jet stream. This leads to enhanced summer precipitation over central Asia and increased winter warming over the north-western Pacific. An accurate Caspian Sea area representation is thus vital in global climate models for paleo and future scenarios and share serious implications for expanding coastal communities, agricultural activities, fisheries and the ecosystem.

Zusammenfassung

Die Klimazustände der nördlichen Hemisphäre zwischen den Gletschern während der späten Quartärperiode verursachten Veränderungen des Kaspischen Meeres (CSL) von bis zu ~ 150 m und können als Analogon für die Beurteilung der gegenwärtigen und zukünftigen Klimaauswirkungen herangezogen werden. Geologische Rekonstruktionen dieser Paläoseenebenen und mögliche Zusammenhänge mit verschiedenen Klimaereignissen bleiben komplex, während die zukünftigen Rückgänge der modellierten Seenebenen stark variieren und ungewiss sind. Die Hauptgründe für eine solche CSL sind Schwankungen im Wasserbudget zwischen Niederschlag und Verdunstung (P-E). In dieser Arbeit wird ein Klimamodellierungsansatz verwendet, um langfristige Veränderungen des Hydroklimas im Kaspischen Meer (CS) während verschiedener Klimazustände vom späten Quartär bis zum Ende des 21. Jahrhunderts zu untersuchen. Die neuen Ergebnisse des Community Earth System Model (CESM1.2.2) können zu einer verbesserten Interpretation rekonstruierter Paläoseepegel in Bezug auf sich ändernde P-E-Muster beitragen und Schlüsseltreiber für zukünftige CSL-Änderungen identifizieren. Diese Studie lieferte neue Modellierungsergebnisse für die späte Quartärperiode, die den zeitlichen Ablauf einschränken und die Klimabedingungen identifizieren, die im Vergleich zu ausgewählten geologischen Rekonstruktionen für größere CS-Überschreitungen und -Rückgänge günstig sind. unter drei glazialen (Marine Isotope 3 (MIS3), letzten glazialen Maximum (LGM), Heinrich Event 1 (H1)) und zwei interglazialen (letzten interglazialen (LIG) und frühen holozänen (EH)) Klimazuständen. Die beiden interglazialen Klimazustände deuten auf günstige Klimabedingungen (höhere Temperatur und Niederschlag) für die CS hin, die zu einem positiven Wasserbudget führen (LIG-P-E-Anomalien von 14,6 m / 1000 Jahre und EH-P-E-Anomalien ~ 5 m / 1000 Jahre). Die Ergebnisse deuten darauf hin, dass eine Überschreitung durch die Kombination von großräumigem Winter- und Sommerniederschlag und konvektivem Niederschlag ausgelöst wird, ausgelöst durch eine verbesserte Sommersonneneinstrahlung und die damit verbundenen Windanomalien. Das wärmere und feuchtere interstadiale MIS3-Klima ist nachweislich für eine Überschreitung mit P-E-Anomalien von 16 Metern / 1000 Jahren verantwortlich. Das kältere und trockenere LGM-Klima begünstigt eine Regression mit einem KGV von -12 Metern / 1000 Jahren. Diese P-E-Anomalien und Klimabedingungen stimmen mit den Rekonstruktionen überein. Unsere simulierten P-E-Anomalien (für das späte Stadium im ersten Halbjahr); erfasst den rekonstruierten Hochstand während der Enteisung nicht, und es ist klar, dass das Schmelzwasser in den CS für diesen Hochstand verantwortlich ist; und da unser Modell kein ausgeklügeltes Schmelzwasser enthält, das in die CS geleitet wird; Vergleiche mit ausgewählten Rekonstruktionen bleiben daher kompliziert. In dieser Studie wurden auch verschiedene horizontale CESM-Auflösungen und Modellkonfigurationen bewertet, um die beste Version zu ermitteln, die das CS-Klima und die Klimamodi der Variabilität wie North Atlantic Oscillation (NAO) für den Zeitraum 1850-2000 CE darstellen kann, sowie neue CSL unter zwei neue Emissionsszenarien bis zum Ende des 21. Jahrhunderts. CESM1.2.2 mit 1 ° CAM5 gilt als die beste Fähigkeit zur Simulation des NAO und seiner Auswirkungen auf die CS-Einzugsgebietshydrologie. Projektionen im Rahmen der repräsentativen Konzentrationspfade RCP4.5 und RCP8.5 bestätigen, dass die Winter-NAO die größte Variabilität im Winter darstellt, die sich erheblich auf das kaspische Einzugsgebiet des Hydroklimas auswirkt. Bei der globalen Erwärmung ist jedoch die Verdunstung über dem Meer der Hauptgrund für eine Verringerung der CSL um etwa 9 m und 18 m zwischen 2020 und 2100 für die Szenarien RCP4.5 und RCP8.5. Die neuen CSL-Werte sind größer als die vorherigen Projektionen von CSL und enthalten eine überschätzte Gesamtverdunstung aufgrund einer größeren CS-Oberfläche in CESM. Trotz des klaren Potenzials dafür wird in aktuellen globalen Klimamodellen die genaue Darstellung des CS-Bereichs vernachlässigt. Diese Studie lieferte neue Ergebnisse, um insbesondere die Auswirkungen verschiedener CS-Oberflächen auf das regionale und großräumige Klima zu bewerten. In der Region wirkt sich das Vorhandensein eines größeren CS-Gebiets eindeutig auf eine höhere Verdunstung über dem Meer und höhere Niederschläge im südwestlichen Einzugsgebiet aus, während die Oberflächentemperaturen im Sommer und im Winter sinken und im kleineren CS-Gebiet umgekehrt. Am wichtigsten ist, dass diese Sommertemperatur die obere atmosphärische Zirkulation (bei 200 hPa und 500 hPa) mit einer Verschiebung nach Süden und einer Erhöhung der Geschwindigkeit des Sommerstrahlstroms stört. Dies führt über Zentralasien zu vermehrten Sommerniederschlägen und über dem Nordwestpazifik zu verstärkter Wintererwärmung. Eine genaue Darstellung des Kaspischen Meeres ist daher in globalen Klimamodellen für Paläo- und Zukunftsszenarien von entscheidender Bedeutung und hat

schwerwiegende Auswirkungen auf die Ausweitung der Küstengemeinden, die landwirtschaftlichen Aktivitäten, die Fischerei und das Ökosystem.

Contents

List of Abbreviations

°C	Degrees Celsius
AMOC	Atlantic Meridional Overturning Circulation
AOGCMs	Atmosphere-Ocean General Circulation Models
CAM4	Community Atmosphere Model version 4
CAM5	Community Atmosphere Model version 5
CESM1.2.2	Community Earth System Model version 1.2.2
CICE4	Community Ice Code version 4
CLM4	Community Land Model version 4
CMIP3	Coupled Model Intercomparison Project (Phase 3)
CMIP5	Coupled Model Intercomparison Project (Phase 5)
CMIP6	Coupled Model Intercomparison Project (Phase 6)
CO_2	Carbon dioxide two
CPL7	Coupler version 7
CS	Caspian Sea
CSL	Caspian Sea Level
DJF	December-January-February
EA	East Atlantic Pattern
ECMWF	European Centre for Medium Range Weather Forecasts
EEP	Eastern European Plains
EH	Early Holocene
eH1	Early Heinrich Stadial 1
ENSO	El Niño-Southern Oscillation
EOF	Empirical Orthogonal Function
FWF	Fresh Water Flux
GHG	Greenhouse Gas
GLAC-1D	Landice-1 Dimension
H1	Heinrich Stadial 1
hPa	Hectopascals
IPCC	Intergovernmental Panel on Climate Change

kyr BP	1000 years Before Present
LGM	Last Glacial Maximum
lH1	Late Heinrich Stadial 1
LIG	Last Interglacial
MIS3	Marine Isotope Stage 3
MIS3_ist	MIS3 Interstadial
MIS3_st	MIS3 Stadial
MIS5e	Marine Isotope Stage 5e
NAO	North Atlantic Oscillation
NCAR	National Centre for Atmospheric Research
NCEP	National Centre for Environmental Prediction
P-E	Precipitation minus Evaporation
PI	Pre-Industrial
POP2	Parallel Ocean Program version 2
RCP	Representative Carbon Pathways
RTM	River Transport Model
SCA	the Scandinavia Pattern
SLP	Sea-level pressure
Sv	Sverdrup
T2m	2-meter temperature

List of Figures

List of Tables

Chapter 1

1 Introduction

The regional paleo-hydroclimate variations in the Caspian Sea and the Caspian Sea level (CSL) are often attributed to the large-scale climate processes over the Northern Hemisphere during glacial-interglacial climate states (Rodionov, 1994). Paleoclimate reconstructions regarding the CSL reveal substantial sea level changes of ~150 m during the past ~130 thousand years before present, hereafter kyr BP. Compared with the present CSL (~28 m below global mean sea level), the CSL is considered to fluctuate between ~50 m higher to ~>90 m lower between glacial and interglacial periods and >3 m in the last century (Arpe & Leroy, 2007; Arslanov *et al.*, 2016; Forte & Cowgill, 2013; Kakroodi *et al.*, 2015; Krijgsman *et al.*, 2019; Naderi *et al.*, 2013; Yanina, 2014). The Caspian Sea has experienced higher and more rapid sea level changes compared to the global ocean and serves as an ideal niche for scrutinizing these changes under extreme climate events that can be used as an analogue for assessing future climate impacts. Climate model projections for the Caspian Sea level vary widely, with a potential extreme decline of up to 9 m projected to occur by the end of the 21st century (Elguindi & Giorgi, 2006a).

The key drivers for the above-mentioned Caspian Sea level range as well as future changes are largely uncertain, but most geologic and climate modeling studies agree that physical mechanisms between the northern hemispheric glacial-interglacial climate states and the regional water budget changes between precipitation and evaporation control the sensitive sea level changes (Rodionov, 1994). Owing to this sensitivity, future risk assessment and developing adaptive strategies are of particular importance for the CS region; especially for coastal communities (e.g. expanding cities), the economy (agricultural activities and fishery) and the ecosystem (biodiversity changes). This thesis employs a modeling approach to improve our understanding of the physical processes that drive changes in the Caspian Sea hydroclimate during the cold and warm climate states from the late Quaternary to the end of the 21st century. The results presented here also serve as a case study for comparisons with other large semi-isolated lake systems (e.g., mega lake Chad and the North American Great Lakes). As such our modeling results can contribute much valued interpretations on extensive climate processes;

especially in absence of or due to sparse geologic reconstructions and are the only tool available for identifying the physical mechanisms for future CSL.

1.1 The Caspian Sea

1.1.1 The current biogeographical and climate context

The present-day Caspian Sea is sited between Russia in the North, Azerbaijan and the Caucasus to the West, Iran in the South, and Kazakhstan and Turkmenistan to the East and is equivalent to the area of Germany (Leroy et al., 2019) (Fig. 1.1). It is located amid the semi-arid Central Asian regions, the flat arid northern terrains, and the humid high mountain ranges of Eurasia. The shallow northern area (water depth of ~ 6 m) and Kara-Bogaz-Gol span an area of 80 000 km^2, while the middle area (water depth of ~80-200m) covers 138 000 km^2, and the southern area (water depth of ~1025m) straddles 168 400 km^2 (Rodionov, 1994). The current Caspian Sea is a surviving fragment of the ancient Paratethys sea (until ~6 Million years ago) and developed as an semi-isolated lake basin during the Pliocene (Forte & Cowgill, 2013). During the late Quaternary, climatic driven episodic periods of isolation and overflow in the Black-Caspian Sea region are considered to cause changes in biodiversity (Yanina, 2014). Geologic reconstructions propose the last overflow from the Caspian Sea into the Black Sea occurred at ~15-11 kyr BP (Chepalyga, 2007).

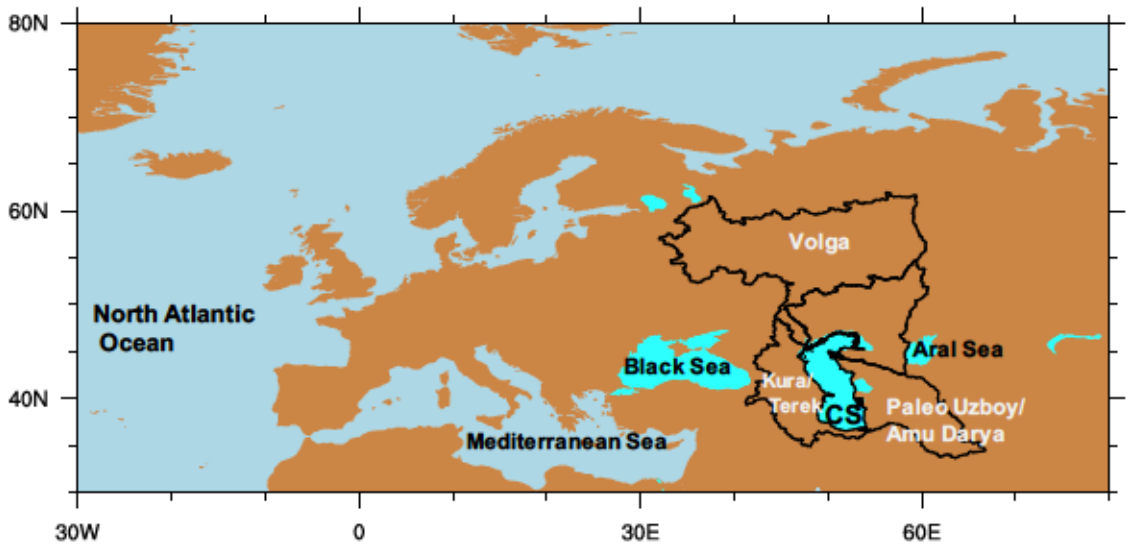

Figure 1.1: Schematic view of the present-day Caspian Sea. The black line denotes present day Caspian catchment area and the major river basins at present and past.

The modern Caspian Sea is the world's largest inland sea, located in a closed catchment area with no outlet. It is within a vast endorheic catchment area (3.6 x 10^6 km^2) which is fed by

~130 rivers, the major ones being the Volga, Kura, Ural, and Terek (Rodionov, 1994). The key inflow source (80%) is the Volga river (1.4×10^6 km^2) that enters the flat northern Caspian Sea area (Arpe & Leroy, 2007; Kroonenberg *et al.*, 2008). The secondary flow comes from the Ural Mountains, while smaller contributions arise from the western rivers of Kura, Terek and Kuma. Other rivers, extinct at present, (for e.g. Amu and Sur Darya) are suggested to contribute significantly by flowing via the Aral Sea into the Caspian Sea (Leroy *et al.*, 2019; Leroy *et al.*, 2014). Hence, the Caspian Sea retains a good sedimentary archive for examining the above-mentioned rapid sea level changes.

The regional CS climate is driven by the northern hemispheric atmospheric circulation patterns such as the mid-latitude westerly winds, the Azores high pressure system, and the polar and subtropical jet stream systems (Rodionov, 1994). These include the northern cold Arctic air and the moist temperate air masses initiating over the Atlantic Ocean and transported over the Caspian region by the westerlies. From the southwest, warm subtropical air masses arise from the Black Sea and Iran while cold and dry continental air masses arise from the East (Kazakhstan). The climate is also governed by the widely complex topography over this region (from high mountain ranges of the Caucasus and Alborz on the southwestern CS and covering the vast northern steep). The climate differs on an annual to seasonal time scales dependent on the location of the polar and subtropical jet stream during summer and winter. Hence, the northern Caspian Sea climate lies in a continental climate zone, whereas the middle and southern CS lie in a warm and dry continental belt.

The Caspian Sea is home to a multitude of endemic species of flora and fauna (Kosarev, 2005; Kosarev *et al.*, 1994). The entire catchment area is rich in valuable biological diversity in terms of ecosystems, natural habitats, large river systems, major wetlands with high level of species endemism and diversity. Specifically, the northern site embodies the highest diversity of both habitat and species, as the Volga and Ural rivers create a region with freshwater and marine dynamics for a high natural productivity. However, in a future warming world, it is highly likely that the shallow northern Caspian Sea may dry out (Chen *et al.*, 2017; Elguindi & Giorgi, 2007), which would have grave implications on its biodiversity.

1.1.2 Caspian Sea Hydroclimate during the Past, Present and Future

In order to understand potential future climate changes in the Caspian Sea catchment area, it is necessary to comprehend the changes during the recent geological past and from present

periods. Since, fluctuations in the CS hydroclimate are a result of interactions between regional and global climate processes, they should be considered in the context of large-scale physical mechanisms over the entire Northern Hemisphere (Rodionov, 1994). When examined closely, regional changes in the Caspian Sea surface area (transgressions/ regressions) appear to broadly coincide with the late Quaternary global warm and cold conditions (Yanina *et al.*, 2018; Yanina, 2012). However, the correlation between these transgression and regression and the late Quaternary climate events is challenging due to multi-disciplinary methods for age estimates and the application of inconsistent stratigraphic schemes (Arslanov *et al.*, 2016; Kroonenberg *et al.*, 1997; Leroy *et al.*, 2014; Yanina, 2014). Hence, this leads to the question of how the major Caspian Sea transgressions and regressions developed during such global glacial and interglacial climate state. Importantly, climate modeling results can contribute in constraining the timing, and the climate conditions favourable for the occurrences of such transgressions and regressions; in comparison with the reconstructions.

The abrupt climatic changes during the last glacial period is considered to include several major CS transgressive and regressive stages. The late Marine Isotope Stage 3 (MIS3) at ~ 35-25 kyr BP period is associated with a transgression that lasted until ~10 kyr BP with a maximum CSL of ~+50m above mean sea level (m.a.s.l) but the age dating is unclear (Arslanov *et al.*, 2016; Svitoch, 2007; Tudryn *et al.*, 2016; Yanina, 2012; Yanina, 2014). Generally, transgressions are proposed to be driven by high freshwater inputs into the Volga river basin, which result from the melting of the Eurasian Ice Sheet in the Eastern European Plains (Arslanov *et al.*, 2016; Tudryn *et al.*, 2016) or the paleo Amu Darya river basin (Leroy *et al.*, 2019; Leroy *et al.*, 2014). Consequently, atmospheric precipitation, enhanced by winter teleconnections (such as the North Atlantic Oscillation) or summer teleconnections (Indian Summer Monsoon) are equally responsible for generating larger CS surface areas. A major regression is suggested to occur during the cold climate conditions of the Last Glacial Maximum (LGM at ~19kyr BP) (Arpe *et al.*, 2018; Bezrodnykh & Sorokin, 2017; Kislov & Toropov, 2007; Sorokin, 2011). Modeling studies highlight this regression with a negative water budget (i.e., higher evaporation than precipitation rates relative to present day) and as a CSL of ~-50 m below mean sea level (Kislov & Toropov, 2007). Following this regression, extreme climatic conditions prevailed during the deglaciation of the Scandinavian ice sheet (~18-13 kyr BP). Tudryn *et al.* (2016) proposes that a highstand resulted by the melting of the ice sheet which routed freshwater into Volga catchment area. But, its extent is linked with uncertainties in the ice-sheet retreat. This period is broadly associated with the Henrich event 1 (H1), which is connected to the release of

freshwater into the North Atlantic Ocean. This is debated to trigger changes in the strength of the Atlantic Meridional Overturning Circulation (AMOC), that transports heat northward. A slowdown of the AMOC can cause the North Atlantic Ocean to cool as less heat is transported northward with resultant changes in temperature and precipitation over northern Europe (Broecker *et al.*, 1992; Broecker *et al.*, 1990). Moreover, a climate modeling approach for assessing the potential relationship between the North Atlantic H1 and the regional CS water budget has yet not been examined, but is considered to result in a very different climate condition when compared to the LGM.

In contrast to the aforementioned glacial conditions, the interglacial climate states represent warmer conditions compared to present day. For instance, the last interglacial period (~130-116 kyr BP) is suggested to be globally warmer (~1 °C) compared to 20th century (McKay *et al.*, 2011; Otto-Bliesner Bette *et al.*, 2013), whereas during the early Holocene (~10.5 to ~8.4 kyr BP) global annual mean surface air temperatures were higher by ~ 0.5°C compared to 20th century but this is also region dependent (Liu *et al.*, 2014; Otto-Bliesner *et al.*, 2006). The reconstructions suggest a transgression for the last interglacial period. However, conditions over the CS is expected to differ substantially for the early Holocene, as some reconstructions suggest a regression that lasted longer for the northern CS (Bezrodnykh *et al.*, 2014; Bezrodnykh & Sorokin, 2017) and others debate it ended earlier for the middle and southern CS (Leroy *et al.*, 2019; Leroy *et al.*, 2014). Both, the last interglacial period and the early Holocene are important for assessing regional changes in the Caspian Sea development as a similar climate for the end of the 21st century is projected by current research (Flato *et al.*, 2013). The timing and the favourable climate conditions responsible for the above changes still remain uncertain. To date, regional changes in the Caspian Sea water budget for the above interglacial climate states have yet not been investigated with climate models. Such an approach could, however, help to clarify the following open questions:

1) *Are regional changes in the Caspian Sea water budget (i.e., precipitation and evaporation) influenced by global glacial and interglacial climate conditions?*
2) *Can a climate model capture the reconstructions for the transgressions and regressions of the Caspian Sea in terms of only water budget changes involving precipitation and evaporation?*

In addition, the major winter North Atlantic atmospheric teleconnection patterns, such as the North Atlantic Oscillation (NAO), the East Atlantic (EA) pattern and the Scandinavian (SCA) pattern play an important role regarding the Caspian Sea water budget changes (P-E). Correlation analyses between these teleconnections and the Caspian Sea water budget based on current and future climate model simulations remain poorly elucidated. The NAO is the leading mode of North Atlantic winter climate variability and is characterized by a north-south dipole in sea level pressure anomalies approximately centred over Iceland and the Azores (Hurrell, 1995; Hurrell & Deser, 2009). The positive and negative phases are linked to changes in the intensity and location of the jet stream, storm tracks, and patterns of meridional and zonal heat and moisture transport. Strong positive phases depict above-average values in air temperature, precipitation and wind velocity across northern Europe and Scandinavia, and below-average values in southern/central Europe. The EA pattern, first described by Wallace & Gutzler (1981), is the second mode affecting climate over the North Atlantic and Europe and has its major centre of action over the mid-latitude North Atlantic (Barnston & Livezey, 1987). Its positive phase is associated with above average surface temperatures in eastern Europe (Comas-Bru & McDermott, 2014). The third mode is the SCA pattern (previously referred to as Eurasia-1 pattern by Barnston & Livezey, 1987). A positive SCA phase is related to a positive sea level pressure anomaly over Scandinavia and may be related to major blocking anticyclones. Examining these effects remain challenging as much depends on the climate model versions and resolutions, which include key underlying assumptions and could hence lead to different results. In general, this raises a number of questions that should be clarified:

1) *Are the different climate model versions and resolutions able to capture North Atlantic winter teleconnection patterns when compared with reanalysis data?*
2) *How does the NAO influence the Caspian Sea hydroclimate and sea level changes at present and future time-scales?*

The future CSL changes remain a matter of debate and are linked to the projected impacts from global warming of 1.5°C above pre-industrial levels (Hoegh-Guldberg *et al.*, 2018). In particular, the comparison between climate model and reanalysis data constitutes an important evaluation process, as the ability to capture reanalysis data with a climate model enhances the overall confidence in the simulated changes shown for present and future projections of the Caspian Sea catchment area. This evaluation process depicts a key model bias, seen in all

models which relates to an inaccurate CS surface area. Mimicking precise Caspian Sea surface areas in climate models remain challenging as models still prescribe an unrealistic Caspian Sea area, often resulting in an over or under estimation of several key processes (e.g., evaporation that affects the water budget). Globally, the present day Caspian Sea has the highest variation in the surface area on interannual-decadal time-scales (Arpe *et al.*, 2018). Climate modeling studies agree that changing surface areas of lakes affect regional and large scale climates (e.g., Farley-Nichols & Toumi (2013) for the Caspian Sea, Contoux *et al.* (2013) for mega lake Chad). These studies suggest associated strong seasonal changes in temperature, evaporation, and precipitation with corresponding seasonal changes in the upper atmospheric circulation and the location of the subtropical jet stream, with increased frequency and strength of cyclones (Notaro *et al.*, 2013; Sousounis & Fritsch, 1994). Hence, an accurate inclusion of the Caspian Sea area in climate models is key to identifying the interactions between the regional and large-scale climate processes and in calculating the future CSL. Nevertheless, some open questions still remain:

1) *Are regional hydroclimate changes in the catchment area solely driven by changing Caspian Sea surface areas?*
2) *How significant are the impacts from different Caspian Sea surface areas on upper atmospheric circulation patterns and the subtropical Jet Stream?*

1.2 Thesis Objectives and Outline

Continuing from recent modeling studies on the Caspian Sea region, this thesis aims to identify and contribute to the physical mechanisms that drive the Caspian Sea hydroclimate and the CSL, as an element of the global climate system; for the recent geological past, present and by the end of the 21st century. Different climate model resolutions and setups are tested to assess the skills for the best model version that represents the Caspian Sea climate variability.
The following three hypotheses are tested to address the research questions stated in section 1.1.2:

1) *The Caspian Sea hydroclimate (i.e., precipitation and evaporation) in the late Quaternary and early Holocene is driven by interglacial-glacial climate conditions and Heinrich events.*

This hypothesis is tested in chapter 3, which examines the impacts from past climate conditions (glacial-interglacial) and Heinrich event1 on the CS hydroclimate. In particular, the climate

model is used to interpret the changes in CS; solely based on changes between evaporation and precipitation that can constrain the timing and climate conditions favorable for the occurrence of the major transgression and regression events based on selected geologic reconstructions.

2) *The Caspian Sea hydroclimate (i.e., precipitation and evaporation) is affected by North Atlantic winter climate for the present and by the end of the 21st century.*

This hypothesis is tested in chapter 4, which evaluates the impact of the historical (1850-2000 CE) and future (2020-2100 CE) North Atlantic winter teleconnections on the CS catchment area water balance of precipitation minus evaporation. Different version and resolutions of the climate model performance have been validated by comparing the present-day climate to reanalysis and observational datasets. This chapter provides key insights on the influence of the North Atlantic on Caspian Sea level by the end of the 21st century.

3) *Changes in the Caspian Sea surface area impact large-scale atmospheric circulation patterns.*

This hypothesis is tested in chapter 5, which assesses the influence of different CS surface areas on the regional atmospheric water budget as well as the large-scale atmospheric circulation patterns like changes in the location of the subtropical jet stream, when compared to a no Caspian Sea scenario. This chapter provides key insights on how different surface areas of CS influences present day climate.

Chapter 2

2 A Modeling Approach

The widely-used Community Earth System Model version 1.2.2 (CESM1.2.2) is employed. CESM1.2.2 is a fully coupled global climate model that provides state-of-the-art computer simulations for the Earth's past, present and future (Hurrell *et al.*, 2013). The development of this model is coordinated by the National Centre for Atmospheric Research (NCAR) in Boulder, Colorado, USA. The CESM1.2.2 coupled components consist of a physics based atmospheric model, a land-surface model, an ocean model, a sea ice model and of a River Transport Model. The models are coupled through a central flux coupler which uses the Model Coupling Toolkit (MCT) and coordinates the exchange of information between these models (Hurrell *et al.*, 2013).

In this thesis, two versions of the Community Atmosphere Model (CAM), i.e., versions 4 (CAM4; (Neale *et al.*, 2010) and 5 (CAM5; (Neale *et al.*, 2012) are used to understand the response of the atmospheric climate and of Caspian Sea hydrology interactions. CAM4 includes improvements in the convection parameterization scheme and in the Arctic cloud formation, leading to a realistic polar response compared to CAM3. CAM5 differs significantly from CAM4 with an improved representation of physical processes; by simulating more realistic full aerosol-cloud interactions and hence indirect radiative effects. It includes improved moist turbulence, shallow convection, cloud micro- and macrophysics, and aerosol schemes (see Neale *et al.*, 2010, for details).

The Community Land Model, version 4 (CLM4; (Lawrence *et al.*, 2011) is quite densely parameterized and consists of several embedded models such as a carbon-nitrogen biogeochemical model with dynamic vegetation, a modified terrestrial hydrology, land cover and land use algorithms, snow and soil sub models as well as human dimensions and ecosystem dynamics. These adjustments (compared to CLM3.5) lead to improved simulations of land surface processes like soil water storage, evapotranspiration, precipitation, vegetation types, surface albedo and permafrost. CLM4 also embeds the River Transport Model (Gent *et al.*,

2011) to transport runoff per grid cell to the ocean. CLM4 aims to develop an understanding between global climate, the terrestrial ecosystem and humans.

The ocean component model is based on the Parallel Ocean Program version 2 (POP2; (Smith *et al.*, 2010)), which solves ocean dynamics 3-D equations using the hydrostatic and Boussinesq approximations. Overall, it shows improvement in reducing sea-surface temperature and sea-surface salinity biases in the North Atlantic relative previous CESM versions (Gent *et al.*, 2011). In POP2, the Caspian Sea is considered as an ocean. The sea ice component is based on version 4 of the Los Alamos National Laboratory Community Ice Code (CICE4) sea ice model (Hunke & Lipscomb, 2010). CICE4 includes a shortwave radiative transfer scheme, enhancing the representation of sea ice and radiative impacts of aerosols on sea ice. This model also explicitly accounts for enhanced Antarctic and Arctic sea-ice distributions (including sea ice thickness, areal extent and spatial patterns).

The CESM1.2.2 ocean and ice models share the same horizontal grid, whereby the atmosphere, land and river runoff models can be on different grids. Here, both 1° and 2° horizontal grids for CAM4 and the 1° horizontal grid for CAM5 are used. The ~1° horizontal grid consists of 199 x 288 latitude/longitude grid cells and uses a uniform resolution of 0.9° x 1.25° in longitude. The ~2° horizontal grid consists of 96 x 144 latitude/longitude grid cells with a uniform resolution of 1.9° x 2.5° in longitude. The atmosphere model has a finite volume core with a uniform horizontal resolution, which is shared with the land model grid. The vertical of the atmosphere model is divided into 26 layers, which are equally distributed. The ocean model grid consists of 60 vertical levels. The horizontal resolution varies and is higher around Greenland, with the North pole being displaced into Greenland, as well as around the equator. Here, a nominal 1° horizontal resolution of the ocean/sea ice grid with 320 x 384 grid points is used.

All numerical simulations were performed at the North-German Supercomputing Alliance (HLRN-III) and on the same machine (Cray XC30/40 of HLRN-III). The simulations were designed in accordance with the guidelines of the Coupled Model Intercomparison Project Phase 5 (CMIP5; (Taylor *et al.*, 2011) and the Paleoclimate Modeling Intercomparison Project Phase 3 (PMIP3; (Braconnot *et al.*, 2012). All analyses were performed with the NCAR Command Line (NCL) software.

2.1 Changing Caspian Sea surface areas in CESM1.2.2 simulations

One of the goals of this thesis was to successfully incorporate realistic modelled CS surface areas to understand the relationship with regional and large-scale climates. Four simulations are designed by changing the surface area of the Caspian Sea. The procedure below outlines multi-step modifications for implementing CESM1.2.2 1° pre-industrial simulations involving different CS surface areas in a fully coupled configuration. This includes changing technical aspects of CESM1.2.2 input and initial conditions (e.g. a land-sea mask) by running and modifying scripts from a Paleo Toolkit developed by the Paleo working group of NCAR, that has been applied to various studies.

For the initial conditions changes in the input files of surface topography, ocean bathymetry and basins, land cover and in the ocean, coupler, land and atmosphere components had to be performed. These were modified from specific default CESM1.2.2 files, which had been set-up using a pre-industrial control configuration. At first, new CS surface areas (big, current, small) were produced with a 5-arc minute ETOPO1 digital elevation model (DEM) and ArcGIS software, by defining the DEM bathymetry (0 m, -90m, -27m). The resultant CS areas were overlaid onto the CESM1.2.2 default ocean model domain file to identify which land and ocean grid points need to be modified. For example, if the water level of a grid point (ocean grid cell) is higher than the mean bathymetry of the grid, this grid point is set to be on land and vice versa. In addition, a no CS surface area was produced, where all ocean grid points corresponding to the CS have been removed and have subsequently been replaced with land grid points.

At first, the new ocean bathymetry was computed. Based on the above-mentioned CS surface areas, a new CESM1.2.2 ocean bathymetry (a 2D binary field called KMT denoting the number of active depth levels at each grid point) was created to reflect changes made to land/ocean areas. The second step involved the creation of mapping files, which serve to interpolate from the POP grid to the CAM grid and vice versa as well as to map river runoff from the land to the ocean. The overall CESM1.2.2 ocean is kept in a pre-industrial state, whereby only changes to the Caspian Sea have been performed. Afterwards, new domains were generated for all components. The next step involved the computation of surface topography and new land surface conditions to account for the newly created land-sea mask and ocean region mask files.

For all simulations, the surface characteristics of the new land grid cells (e.g. plant functional types like grasslands and soil properties) were interpolated using the nearest neighbour grid cell. The surface land characteristics were recalculated for each simulation of CS surface area. Since the model is sensitive to changes between the land-sea masks of various model components, CESM1.2.2 was run for 5 days to check for a successful production of initial conditions. Subsequently, initial land surface conditions were interpolated (using the Interpinic-a CESM tool) onto the newly defined land surface. With this new land-sea mask, topography, mapping files, domain files and initial conditions for the land model were obtained. However, these interpolated initial conditions are not in equilibrium with the local climate (e.g. land cover and vegetation change). Hence the last step was to implement a new CESM1.2.2 pre-industrial control simulation including the above-mentioned configuration, which was spun up for ~100 years to reach equilibrium in the near surface climate conditions. Each time the CS surface area changed, the above steps were repeated.

2.2 CESM1.2.2 simulations outline

The main modeling aspects of chapters 3-5 are stated (Table 2.1).

Additionally, two Intergovernmental Panel on Climate Change (IPCC) scenario-based 1° CAM5 projections of atmospheric composition relative to pre-industrial conditions named Representative Concentration Pathways (RCPs) 4.5 and 8.5 were simulated. The RCPs project radiative forcing based on the forcing of different greenhouse gases until the end of the 21st century. The RCP8.5 is categorized as a high-range scenario with continuously rising greenhouse gas emissions throughout the 21st century, ending up with an additional radiative forcing of 8.5 W/m^2 at the end of the century (Lamarque *et al.*, 2011). The RCP4.5 is a mid-range scenario that stabilises and does not exceed the total radiative forcing of 4.5 W/m^2 by the year 2100 (Meinshausen *et al.*, 2011). Utilising RCP4.5 and RCP8.5 provides a range of forcings to explore the long-term response of the climate and Caspian Sea catchment area system to the anthropogenic components of radiative forcing by the end of this century.

Table 2.1: CESM1.2.2. simulations.

Time	Version	CO_2 (ppm)	CH_4 (ppb)	N_2O (ppb)	Eccentricity	Obliquity (degrees)	Precession (degrees)
127 kyr - Last Interglacial	2° CAM4	275	685	255	0.0393	24	275
35 kyr - MIS3 Stadial, *Fresh water Forcing (FWF)* (100mSv)	2° CAM4	203	512	203	0.0146	22.7	248
35 kyr - MIS3 Interstadial	2° CAM4	203	512	203	0.0146	22.7	248
21 kyr - Last Glacial Maximum	2° CAM4	190	357	200	0.0189	22.9	114
18 kyr - Early Heinrich Event 1, *FWF* (100mSv)	2° CAM4	190	357	200	0.0189	22.9	114
15.2 kyr - Late Heinrich Event 1, *FWF* (100mSv)	2° CAM4	223	474	212	0.0196	23.8	209
9 kyr - Early Holocene	2° CAM4	265	680	260	0.0191	24.2	319
1850 Pre-Industrial (PI)	2° CAM5	280	760	270	0.0167	23.4	102
1850 PI *	1° CAM5	280	760	270	0.0167	23.4	102
1850-2005	2° CAM4	**Transient historical green-house gas forcing branched from 1850 conditions.**					
1850-2005	1° CAM4						
1850-2005	1° CAM5						
2005-2100	1° CAM5	**Transient green-house gas branched from 2005 conditions and for RCP4.5 and RCP8.5.**					
2005-2100	1° CAM5						

*Has been repeated 4 times with the different CS surface areas.

3 Hydroclimatic constraints on Late Quaternary transgressions and regressions of the Caspian Sea: a model study

Sri D. Nandini-weiß [1], Matthias Prange[1], Pepijn Bakker[1,*], Klaus Arpe[2], Suzanne A. G. Leroy[3] and Michael Schulz[1]

[1] MARUM –Center for Marine Environmental Sciences and Faculty of Geosciences, University of Bremen, Germany.

[2] Max-Planck-Institute for Meteorology, Hamburg, Germany.

[3]Aix Marseille Univ, CNRS, Minist Culture, LAMPEA, UMR 7269, 5 rue du Château de l'Horloge, 13094 Aix-en-Provence, France.

[4]Vrije Universiteit Amsterdam, Department of Earth Sciences, Netherlands.

Abstract

The major Caspian Sea transgressions and regressions during the Late Quaternary remain poorly constrained as reconstructions greatly differ amongst studies. It is hypothesized that changes in Caspian Sea transgressions and regressions were driven by changes in precipitation minus evaporation (P-E). By using a modeling approach, we test the interpretation of paleo-lake level reconstructions with respect to changing P-E patterns. The hydroclimate of the Caspian Sea catchment area is simulated under three glacial (Marine Isotope 3 (MIS3) 35kyr BP, Last Glacial Maximum (LGM) 21kyr BP, Heinrich event 1 (H1)) and two interglacial (last interglacial (127 kyr BP) and early Holocene (9kyr BP)) climate states, using the Community Earth System Model version 1.2.2. Results show a positive P-E occurred during the MIS3 interstadial stage due to warmer and wetter climate compared to the MIS3 stadial stage. A CS negative P-E occurred during the LGM due to a colder and drier climate over the entire Volga basin. Our model suggests different climate conditions between the early (18 kyr BP) and late (15.2 kyr BP) stages in H1 affect the Caspian Sea catchment area differently. Compared to the previous LGM climate, the early H1 results in a negative P-E, while a positive P-E occurs for the late H1. The last interglacial and early Holocene climates suggest warmer and wetter climate resulting in positive water budget changes of P-E. Although the P-E changes do not capture the large magnitude of all the reconstructions, our model results provide constraints on the selected major transgressions and regressions, based on the interaction between the large-scale North Atlantic climate and the regional hydroclimate variations in the larger Caspian Sea catchment area.

3.1 Introduction

The current Caspian Sea Level (CSL) is ~28 m below global mean sea level. At present, the Caspian Sea (CS) is the largest inland sea (~386 400 km^2, excluding the Kara-Bogaz-Gol), located in an endorheic basin, sited in Eurasia and fed by ~130 rivers (Arpe *et al.*, 2018; Leroy *et al.*, 2019; Rodionov, 1994) (Fig. 3.1). Owing to its closed nature, the CS is very sensitive to river discharge and hydroclimate (precipitation and evaporation over the CS) changes in its large catchment area (~3600 000 km^2) (Kosarev, 2005; Leroy *et al.*, accepted). The present-day summer precipitation over the northern CS catchment of the Volga river is the key contributor (80 to 90%) to changes in CSL (Arpe & Leroy, 2007; Arpe *et al.*, 2012). Today, the CS nestles amid the complex topography of humid towering mountain ranges in Eurasia, the vast northern steppe terrains (the Russian Plain, also known as the East European Plain) and the semi-arid eastern Central Asian regions. As such, the entire CS catchment area covers a climatically diverse region (Chen & Chen, 2013) and in particular, presents a good source of sedimentary archives, aiding in the understanding of rapid sea-level changes under extreme climate events (Leroy *et al.*, accepted).

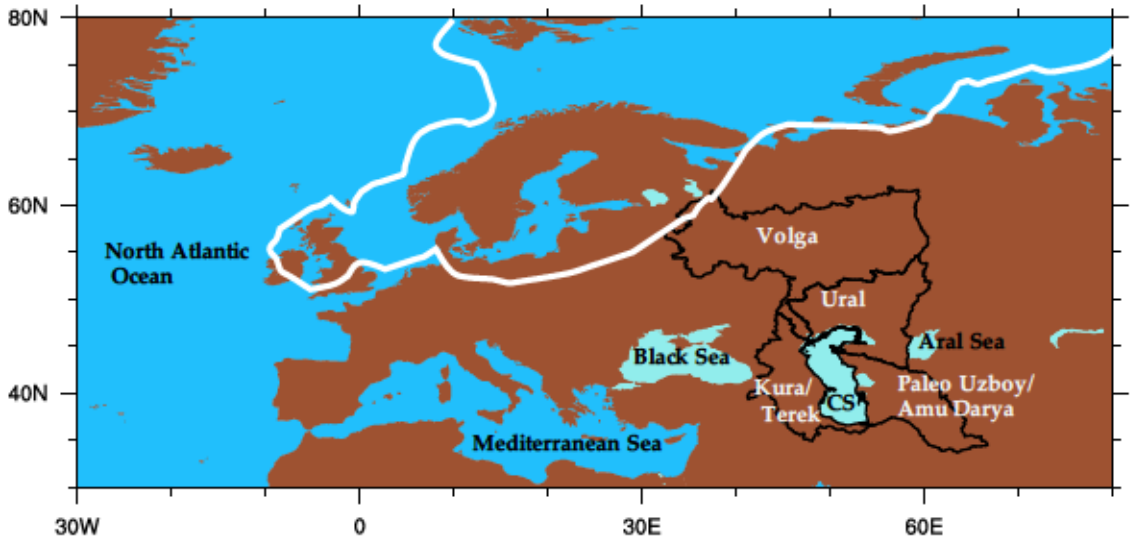

Figure 3.1: The Caspian Sea (CS) and neighbouring areas. The black lines signify the Caspian Sea catchment area and the white line indicates the extent of the Last Glacial Maximum ice sheet based on the GLAC-1D dataset (Briggs et al., 2014; Tarasov et al., 2012; Ivanovic et al., 2016).

Throughout the last glacial cycle, the CS has experienced severe sea level changes varying by >150 m which are poorly identified and not well understood as reconstructions differ amongst literature (Leroy *et al.*, accepted). Compared with the present CSL, past CSL are suggested to have been between ~50 m higher and ~100 m lower (Yanina, 2014). During the

Holocene the CSL can have fluctuated by several tens of meters (Kroonenberg *et al.*, 1997; Rychagov, 1997; Yanina, 2014). These CSL changes were likely driven by contrasting climatic conditions which resulted in large changes in the regional water budget (precipitation minus evaporation; P-E). However, correlation between climatic events and major transgressions and regressions is hampered by large age uncertainties and the application of indirect stratigraphic schemes amongst studies (e.g. CS fossil molluscan fauna) (Leroy *et al.*, accepted). A transgressive phase is generally recognizable from dating ancient shorelines (Yanina, 2014), however, a regressive phase is difficult to date since it results in a sedimentation hiatus along the coast due to successive transgressions (Kroonenberg *et al.*, 2008; Kroonenberg *et al.*, 1997; Leroy *et al.*, 2014). Moreover, further complication arises as several repeated short-lived transgressions and regressions were embedded in the major phases. As such, geologic studies often contradict the age and extent of the CS transgressions/ regressions (Arslanov *et al.*, 2016; Kakroodi *et al.*, 2015; Kroonenberg *et al.*, 2008; Leroy *et al.*, accepted; Leroy *et al.*, 2014; Tudryn *et al.*, 2016; Yanina, 2014). It is therefore still largely unknown what kind of climatic conditions favored the development of major CS transgressions and regressions in the geological past.

To address this question, we designed different equilibrium simulations based on transient transgressive and regressive stages as suggested by geological reconstructions (cf. Table 3.1 and 3.2). Additionally, our climate simulations can be used to investigate on what kind of large-scale climate conditions were favorable for the major CS transgressions and regressions. The relatively warm era of the Last Interglacial (LIG; ~130-116 kyr BP; also known as Marine Isotope Stage 5e (MIS5e)) has been proposed to involve the late *Khazarian* minor transgression (of ~-10m highstand (relative to ~-28m) by Yanina, 2012) with large age estimates (~140-76 kyr BP) varying amongst literature cited in Yanina (2014) (Table 3.1). Recently, Krijgsman *et al.* (2019) connected the late *Khazarian* transgression phase between 127-122 kyr BP. Until now, climate models have not been used to investigate if the LIG climatic conditions favored a CS transgression or not.

Geological reconstructions suggest that most likely several major CS transgressive and regressive stages occurred during the last glacial period (~115-11.7 kyr BP). Many geologists agree that the Marine Isotope Stage (MIS) 3 (~35-25 kyr BP) reflects the initial expansion phase of its greatest transgression called the *Khvalynian* (Arslanov *et al.*, 2016; Krijgsman *et al.*, 2019; Yanina, 2014) which continued until the deglaciation (~13 kyr BP) (Table 3.1). The

Khvalynian includes a probable highstand of ~+50m, but includes large age uncertainities for the maximum stage and is based on regional stratigraphic schemes (without stratotypes) (Arslanov *et al.*, 2016). However, it is unclear whether this stage was linked to a stadial or an interstadial event. Also, climates models have not yet identified the main freshwater sources or favourable climatic conditions for this transgression. It is generally accepted that the *Khvalynian* phase was divided by a major regression (*Elton or Enotaevka?*) with a lowstand of >100m (undated) which covers the Last Glacial Maximum (LGM; Table 3.1). Nevertheless, the age for the maximum stage remains unclear and subject of discussion (Yanina, 2014). Climate modeling studies suggest a lowstand (Arpe *et al.*, 2011) and indeed show a negative water balance anomaly (i.e., higher evaporation than precipitation rates relative to present-day) resulting in a CSL of ~ -50 m below msl by Kislov & Toropov (2007) and -32/33 m below msl by Arpe at el. (2018). Following this regression, the *Khvalynian* transgression is considered to continue into the extreme climatic conditions of the early and late stages in the deglaciation (~18-14 kyr BP) (Table 3.1). The best studied example involves radiocarbon dating on mollusk shells show two high stands of +35 m at 16 kyr and +22 m at 14 kyr BP (Arslanov *et al.*, 2016). Recently, Tudryn et al. (2016) have confirmed that the *Khvalynian* transgression resulted from high freshwater into Volga river basin driven by the melting of the Eurasian Ice Sheet on the Eastern European Plains (EEP). However, its extent is still debated, and linked to uncertainties in ice-sheet retreat. This deglaciation stage generally coincides with the abrupt cooling episode of Heinrich Event 1 (H1; ~18-15 kyr BP) (Broecker *et al.*, 1992; Broecker *et al.*, 1990). During H1 the release of freshwater into the North Atlantic Ocean due to the melting of icebergs likely resulted in a slowdown of the Atlantic Meridional Overturning Circulation (AMOC), which in general transports heat northward. Hence, changes in the AMOC strength during H1 can trigger substantial temperature and precipitation changes over northern Europe and the CS catchment area. A climate modeling approach for assessing the above has not been examined yet, but is speculated to result in very different climate conditions compared to the LGM.

Lastly, it has been confirmed that the *Mangyshlak* regression occurred in the CS during early the Holocene (~-113m lowstand) (Bezrodnykh & Sorokin, 2017; Kroonenberg *et al.*, 1997; Leroy *et al.*, 2019; Yanina, 2014). This lowstand has been established at c. 11.5-10.5 kyr BP in the middle CS (Leroy *et al.*, 2014) and at >11.7-11.2 kyr BP in the southern CS (Leroy *et al.*, 2013). The age limits for this lowstand are longer in the shallow northern CS (12-9 kyr BP) (Bezrodnykh & Sorokin, 2016). Here, we study the subsequent transgression called the post-

Mangyshlak highstand (Leroy *et al.*, 2019) coinciding with the early Holocene climate (Table 3.1). In particular, there remains uncertainty regarding the age and the potential freshwater sources (inactive paleo rivers and channels e.g. Amu Darya) contributing to this subsequent highstand. To date, regional changes in the CS water budget for the early Holocene have not been examined with climate models.

The above show there is evidence of CS high and low stands but the age uncertainties of the analogous transgressions and regressions are huge and highly debated in the literature. Hence, we apply a modeling approach to constrain the timings of the major CS transgression/ regression. Since it is still not fully known what kind of climate conditions favored the major CS transgressions and regressions, we use our modeling approach to assess whether these transgressions and regressions are linked to the general climatic conditions (i.e. warm and cold climates). In particular, we aim to identify the climate processes over the Northern hemisphere that impact changes in the CS water budget involving precipitation and evaporation; leaving aside potential changes in river hydrography, and compare our time-slice model results with selected geological reconstructions which are transient in nature.

3.2 Methods

3.2.1 CESM1.2.2

We used the Community Earth System Model version 1.2.2 (Hurrell *et al.*, 2013). The CESM coupled components include an atmospheric model, i.e., the Community Atmospheric Model CAM4 (Neale *et al.*, 2010), a land-surface model, i.e., the Community Land Model CLM4 (Lawrence *et al.*, 2011), an ocean model, i.e., the Parallel Ocean Program, POP2 (Smith *et al.*, 2010) a sea ice model, i.e., the Community Ice CodE, (CICE4) and a River Transport Model, RTM (Gent *et al.*, 2011). The components are coupled through a flux coupler. The atmosphere model uses a finite volume grid with a 1.9° x 2.5° uniform horizontal resolution, which is shared with the land model grid. The atmosphere grid has 26 vertical levels. The CESM1.2.2 ocean and sea ice models are assigned the same nominal 1° resolution horizontal grid. The ocean model grid has 60 levels in the vertical.

3.2.2 Experimental setup

Table 3.1: CS transgressions/ regressions. Most probable reconstructed stages of Caspian Sea transgressions and regressions relative to present day.

Mean CSL Phase	Period	CESM Simulations	Estimated age (kyr BP)	Key Reconstructions
Late *Khazarian* **Transgression** (High stand of ~-10m)	Last interglacial/ Marine Isotope Stage 5e	LIG (MIS5e)	~140-76 ~127	Rychagov, 1997; Yanina, 2014; Dolukhanov et al., 2009 Krijgsman *et al.* (2019)
Early Khvalynian **Transgression**	Late Marine Isotope Stage 3	MIS3 (st and ist)	~35-25	Yanina 2014
Elton? **Regression** (~lowstand)	Last Glacial Maximum	LGM	~23-19	Yanina, 2014
Late Khvalynian **Transgression** (High stand of~ +50 m)	Deglaciation phase	eH1 lH1	~16 (+35m) ~14 (+22m)	Arslanov *et al.*, 2016
Mangyshlak **Regression** post-*Mangyshlak* **Highstand**	Early Holocene	EH	12-9 11.5-10 ~8.5-8	(Bezrodnykh & Sorokin, 2017; Rychagov, 1997; Yanina, 2014) (North CS) Leroy *et al.*, 2013; 2014 (middle and south CS) Leroy *et al.*, 2019
~ -28 m	Present day	PI	0	Arpe *et al.*, 2018

Table 3.2: CESM simulations with atmospheric composition and freshwater hosing.

Time	CESM simulations	CO_2 (ppm)	CH_4 (ppb)	N_2O (ppb)	FWF
Last Interglacial (LIG)	127 kyr	275	685	255	
MIS3_Stadial (MIS3st)	35 kyr	203	512	203	100mSv
MIS3 Interstadial (MIS3ist)	35 kyr	203	512	203	
Last Glacial Maximum (LGM)	21 kyr	190	357	200	
Early Heinrich Stadial 1 (eH1)	21 kyr	190	357	200	100mSv
Late Heinrich Stadial 1 (lH1)	15.2 kyr	223	474	212	100mSv
Early Holocene (EH)	9 kyr	265	680	260	
Pre-Industrial (PI)	1850	280	760	270	

In total, we performed eight time-slice simulations (Table 3.2) in order to get insight into the paleo-hydroclimatic conditions during several key transgressive/regressive phases of the CS (Table 3.1). A standard pre-industrial (PI) control simulation was carried out following the

PMIP3 (Paleoclimate Modeling Intercomprison Project 3) guidelines (Braconnot *et al.*, 2012). The PI control run was spun up from modern initial conditions and ran for 1000 years until a climate equilibrium was reached. In all paleoclimate simulations the ozone and aerosol distributions as well as the solar constant were kept the same as in the PI. Analysis of these quasi equilibrium states are based on the last 50 year mean climatologies of each experiment.

We set up two interglacial climate simulations representing the last interglacial (127 kyr BP; experiment LIG) and the early Holocene (9 kyr BP; experiment EH). Except for orbital parameters and greenhouse gas concentrations, all boundary conditions are identical to PI (Table 3.2). For both time slices the astronomical forcing produces northern hemisphere summer insolation close to maximum (Otto-Bliesner *et al.*, 2017). Both simulations were initialized from the PI control run and integrated for 800 years.

In total, five simulations for glacial conditions were performed (Table 3.2). All glacial simulations apply the same LGM-like land-sea mask based on Di Nezio *et al.* (2016). This land-sea mask reflects a glacial sea-level decrease of ca. 120 m compared to present day. As the resulting advance of oceanic coastlines was applied globally following a standard procedure and the CS is part of the ocean model in CESM1.2.2, the CS surface area is smaller in comparison with present day. The characteristics of exposed land surface grid cells are prescribed according to nearest-neighbor extrapolation based on present-day conditions. The applied ice-sheet configurations for all glacial time slices are based on the GLAC-1D ice sheet reconstructions (Briggs *et al.*, 2014; Ivanovic *et al.*, 2016; Tarasov *et al.*, 2012). The 35 kyr time slice was chosen to represent the late MIS3. This simulation was initialized from the >1 kyr long equilibrium LGM run of Di Nezio *et al.* (2016) and run for 200 years with MIS3 climate conditions. The resulting MIS3 climate is characterized by a relatively strong AMOC with a volume transport of ~22 Sv (1 Sv = 10^6 m^3/s), which is comparable to the PI AMOC. Therefore, this climate state most likely represents an interstadial state (experiment MIS_ist) as seen also from (Zhang *et al.*, 2014). In order to obtain a stadial state with reduced AMOC (experiment MIS_st), we perturbed the ocean circulation by introducing a freshwater flux of 100 mSv into the North Atlantic over the so-called Ruddiman Belt (approximately between 41 and 50°N). The hosing (stadial) experiment was initialized with the MIS3 interstadial climate and the freshwater forcing was continuously applied for 200 years resulting in an AMOC volume flux of only 10 Sv. As a consequence, mean annual surface air temperature over Greenland drops by about 8°C compared to the unperturbed MIS3 simulation, which is in reasonable agreement with reconstructed Greenland temperature differences between

interstadial and stadial states (Huber *et al.*, 2006; Kindler *et al.*, 2014). Therefore, examining the perturbed and the unperturbed MIS3 states allows us to assess whether the early *Khvalynian* transgression was linked to stadial or interstadial climate. In order to compare the MIS3 climate with the full glacial state of the LGM, a 21 kyr simulation was performed (Table 3.2). The LGM simulation is also a continuation of the >1 kyr long equilibrium simulation by Di Nezio *et al.* (2016) and was run for additional 200 years. In an additional experiment, the LGM climate state was perturbed by North Atlantic freshwater hosing in the same way as in the MIS3 stadial experiment. This hosing experiment simulates the early phase of H1 (experiment eH1). To simulate the late phase of H1 (experiment lH1) changes in greenhouse gas concentrations, ice-sheet size and orbital forcing have to be considered. To this end, we performed a climate simulation with 15.2 kyr boundary conditions and a freshwater perturbation as in the other hosing experiments (Table 3.2). The hosed 15.2 kyr run was integrated for 200 years and initialized from an equilibrated non-hosed 15.2 kyr climate. The hosed LGM (eH1) and 15.2 kyr (lH1) experiments were studied to obtain insight into hydroclimatic processes during the last deglaciation which presumably coincides with the late *Khvalynian* transgression. Under the 35 kyr, 21kyr and 15.2 kyr simulations, the GLAD-1D ice sheet elevation and extent is different, especially close to the CS northern (Volga) catchment area (Fig. 3.2). At 35 kyr, the elevation is limited to~1000 meters above sea level (m.a.s.l) and is centered over Scandinavia. Compared to this, the ice sheet has maximum elevation at 21 kyr (> 2000 m.a.s.l) and gradually declines at 15.2 kyr (~1800 m.a.s.l); and extends to the western margin of the Volga catchment area.

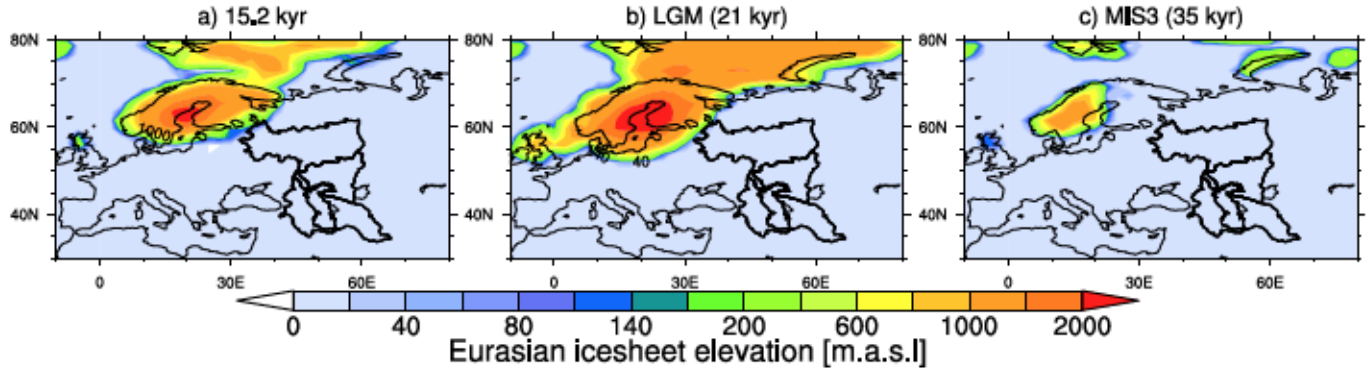

Figure 3.2: Eurasian ice sheet dynamics. GLAC-1 ice sheet elevation (meters above sea level) at **a)** 15.2kyr, **b)** 21 kyr and **c)** 35 kyr.

3.3 Results and discussion

Our new simulated results aim to provide an overview for the large-scale climate conditions responsible for variations in the CS water budget (P-E anomalies) that are associated with the

major transgressions and regressions during the Late Quaternary and compare them with selected geological reconstructions. Assessment for the ability of this model version to simulate key parameters of the North Atlantic and Caspian climate (temperature, precipitation, P-E) and major climate modes of winter variability (e.g., North Atlantic Oscillation) was carried out in Nandini et al., revised. Previous studies have shown that the size of the CS surface area has a major impact on the CS water budget mainly through its effect on evaporation (Arpe *et al.*, 2018; Farley-Nichols & Toumi, 2013; Nandini *et al.*, revised). Due to the different CS surface areas in our glacial and interglacial experiments (see Section 3.2.2) CS water budgets of the glacial simulations are not comparable to the water budgets of the interglacial simulations. Moreover, the CS surface area in the PI (and hence the LIG and EH) simulations is larger than the actual modern surface area since the default CESM1.2.2 land-sea mask, which assumes a CSL of 0 m rather than 28 m below global mean sea level, was used in all interglacial simulations. In particular, we consider this when discussing the transgressions and regressions stated in Table 3.1 with our 'quasi transient' equilibrium simulations.

3.3.1 Last Interglacial (LIG) climate anomalies and the late *Khazarian* transgression event

We present our simulated results for the last interglacial (LIG) to provide the timing and the climate conditions favorable for a larger CS surface area which is be presumably related to the late *Khazarian* transgression event (MIS5e) (Yanina, 2014). Our model results and discussion for the LIG climate are relative to the simulated pre-industrial (PI) conditions. The LIG annual mean air temperature at 2-meter height increased over the CS catchment area by >0.5°C with a peak over central Europe (Fig. 3.3a) that potentially results from a higher summer insolation. The annual mean precipitation anomalies include a north-south dipole pattern over the larger CS catchment area with decreases over the northern area (Volga basin) (~-0.4 to 0.2 mm/day) and increases for the middle and southern area (Fig. 3.3b). The resultant P-E pattern closely follow the above precipitation dipole pattern (Fig. 3.3c). Most of this region's annual precipitation is dominated by large-scale precipitation which is governed by water vapor fluxes transported by the North Atlantic westerlies; seen here as the annual total precipitable water in the atmosphere (Fig. 3.3d). An important point to consider is that the entire CS catchment area spans a large geographical area (latitude-longitude) and is influenced by major atmospheric teleconnections over differing climate states of the past; such as the winter North Atlantic Oscillation-NAO (Panin & Dianskii, 2014), the winter Artic oscillation-AO (Rodionov, 1994),

the Indian (and Asian) summer monsoon (ISM) (Leroy *et al.*, 2014) and the summer El Nino Southern Oscillation (ENSO) (Arpe *et al.*, 2000). Hence, it is not always clear which of these major climate systems contributed to the large-scale and the convective precipitation that is key in controlling CS surface area changes. Our results show that it is the summer precipitation anomalies that drive the north-south dipole pattern in the annual mean precipitation for the LIG (Fig. S3.1a). We discuss the winter variability for this region first, followed by the summer variability that contribute to the enhanced precipitation dipole pattern.

Since large-scale circulation patterns from the North Atlantic are known to play a key role in regional precipitation changes, we examine the winter sea level pressure (SLP) and the winter zonal wind at the 850 hPa level. Together, the enhanced pressure gradient and anomalous westerly wind brings more water vapor to southern CS, and leaves less precipitation in northern CS (Fig. 3.3e & 3.3f). There's a negative NAO-like pattern suggested by the weaker winter westerlies that result from the generally well-known north-south dipole in the SLP anomaly whereby the atmospheric pressure gradient at sea level between the Icelandic low and the Azores high is weaker than average. As a consequence, storms over this region tend to be weaker, and their tracks can be shifted southward compared to average storm tracks (Fig. S3.4a). This increases the probabilities of storms hitting central and southern parts of Europe. In this context, the annual precipitation pattern likely results from a combination of weakened winter westerlies and regional thermodynamics (Clausius-Clapeyron relationship) triggered by mid-latitude warming. However, it is also conceivable that the annual dipole pattern seen in precipitation, caused by the summer precipitation in response to the enhanced summer insolation, induced lower summer SLP and strengthen summer westerly anomalies (Fig. S3.5a & b). The summer SLP patterns and the summer westerlies contribute to the main patterns seen for the annual mean SLP and the annual mean zonal wind at 850 hPa level (Fig. S3.6a & S3.7a).

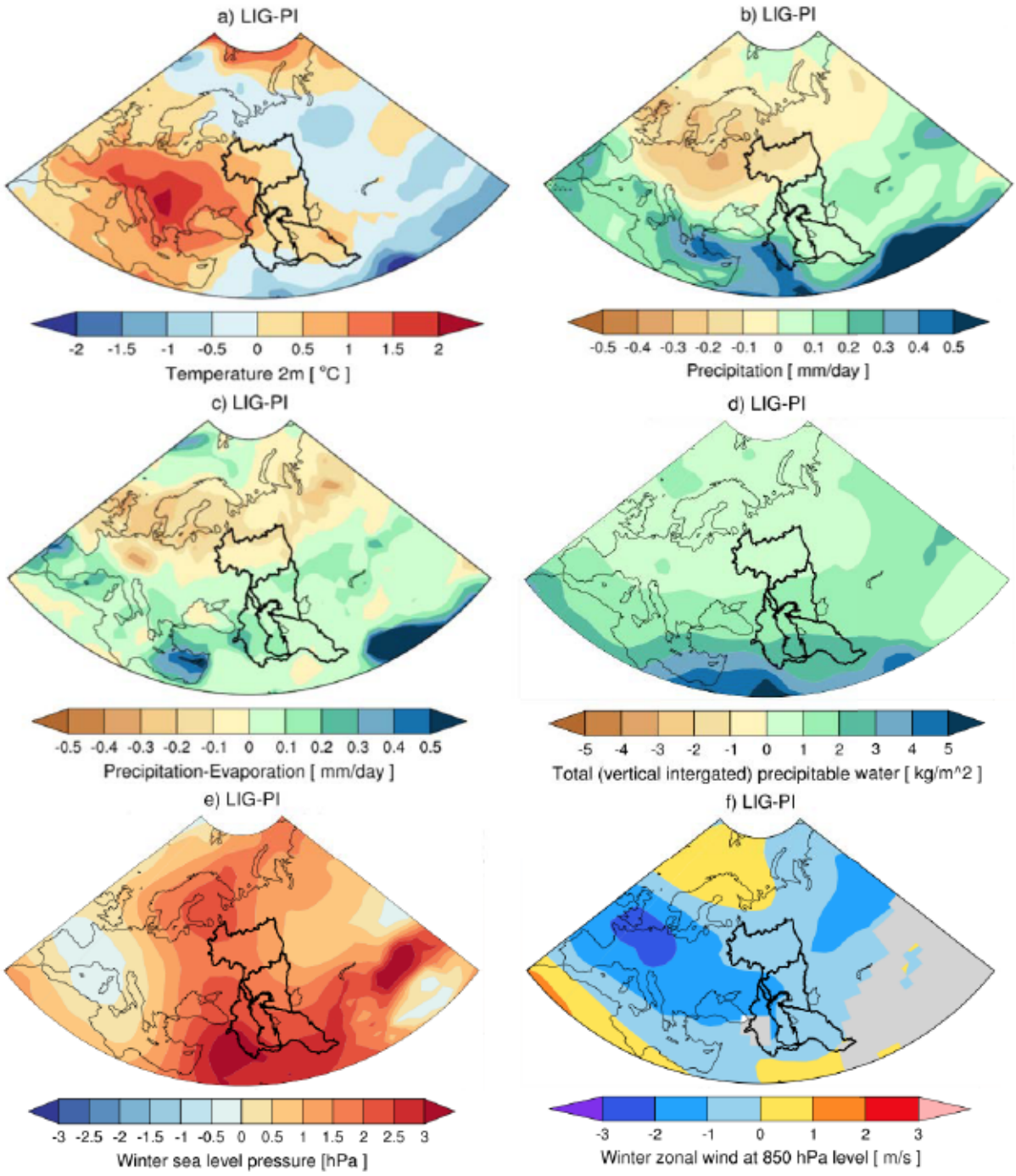

Figure 3.3: Climate conditions for the last interglacial. **a)** Annual mean 2-meter temperature (°C), **b)** precipitation (mm/day), **c)** precipitation minus evaporation (mm/day) and **d)** the total precipitable water (kg/m^2), **e)** winter sea level pressure (hPa) and **f)** winter zonal wind at 850 hPa (m/s) level relative to pre-industrial (PI) values. The black outline denotes the CS catchment area.

The LIG period shows a warmer and wetter (drier) climate over the southern (northern) CS catchment area that is primarily related to summer convective precipitation, triggered by the enhanced insolation that destabilizes the atmosphere. This period is studied as an analogue for a warmer future world (~1°C) and to evaluate climate model performance (Masson-Delmotte *et al.*, 2013; Otto-Bliesner Bette *et al.*, 2013; Otto-Bliesner *et al.*, 2017). However, the timing

of the thermal maximum across the globe remains to be precisely assessed due to different methods used in analyzing a variety of temperature proxies retrieved from paleoclimate (ice, marine and terrestrial) archives (Bakker & Renssen, 2014; McKay *et al.*, 2011). Our model results identify the LIG (127 kyr) climate conditions responsible for the occurrence of a larger CS surface area. Our time-slice simulated results agree with selected geological reconstructions that debate for a transgressive event during the LIG that corresponds to the late *Khazarian* period (Krijgsman *et al.*, 2019) that includes large age estimates based on the precision of the available dating methods (140-76 kyr BP) (Dolukhanov *et al.*, 2009; Tudryn *et al.*, 2013; Yanina, 2014). In particular, this period also included two major transgressions and regressions (Dolukhanov *et al.*, 2009; Yanina, 2014).

3.3.2 MIS3 Interstadial (MIS3_ist) versus stadial (MIS3_st) climate anomalies and the early *Khvalynian* transgression event

Our simulated results evaluate whether the early *Khvalynian* transgressive stage is linked to the stadial or interstadial MIS3 climate by considering the stadial as a perturbed (hosing) climate state and the interstadial as the unperturbed glacial climate state. Our results are discussed with a focus for the MIS3 interstadial relative to the MIS3 stadial climate conditions. The MIS3 glacial period consisted of rapid smaller growth and melting of ice sheet between warm and cold periods with opposing climate conditions over the mid-latitudes (Van Meerbeeck *et al.*, 2009). Compared to the stadial, the interstadial stage indicates a much warmer climate with higher temperatures over the North Atlantic (>22°C) and the CS catchment area (~8°C) (Fig. 3.4a). This strong warming over the North Atlantic is largely responsible for the enhanced large-scale precipitation for the MIS3 interstadial compared to the stadial climate (Van Meerbeeck *et al.*, 2009). Accordingly, the precipitation increases across the region; with the wettest conditions of >0.5mm/day over the North Atlantic, Europe, the Mediterranean the northern CS catchment area (Volga area) (Fig. 3.4b).

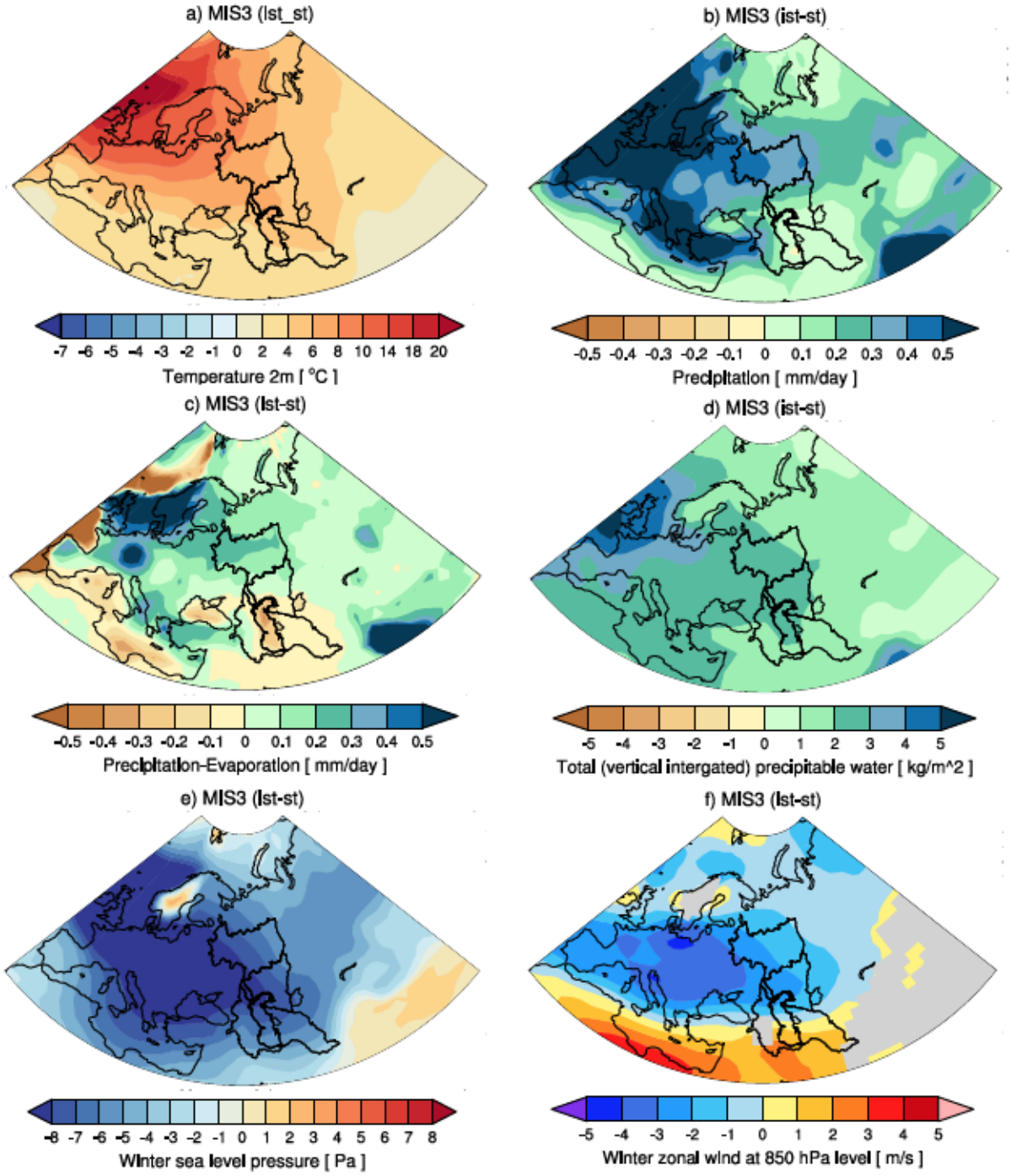

Figure 3.4: Climate conditions for the Marine Isotope Stage 3. Same as Fig. 3.3 but for the Marine Isotope Stage 3 interstadial (MIS_ist) relative to the stadial (MIS_st).

Our results suggest the enhanced winter precipitation controls the regional annual precipitation (Fig. S3.2b). Additionally, this strong thermal gradient also increases the corresponding evaporation pattern (Fig. S3.3b). In particular, this enhanced evaporation over the CS itself can lead to greater moisture availability for precipitation (recycling) especially over the northern CS catchment area; as seen from the P-E anomalies. The annual P-E anomalies exceed >0.5mm/day over Europe and 0.2-0.3mm/day over the northern CS catchment area,

with a decrease in P-E for the middle and southern areas (Fig. 3.4c). Upon integrating the annual P-E anomalies for the entire CS catchment area, we present a positive water budget of P-E = 16 meter/1000yr which is clearly influenced by higher precipitation over the Volga catchment area. This increase in precipitation is attributed to the increase in total precipitable water transported from the Atlantic towards the CS catchment area (Fig. 3.4d) as well as thermal driven changes in the winter atmospheric SLP anomalies (-6 hPa over the entire CS catchment area) and the corresponding lower atmospheric circulation like the winter weaker westerlies over northern CS (-4 m/s) compared to southern area (2 m/s) (Fig. 3.4e & f). The winter patterns for SLP and the westerlies clearly control the annual mean patterns in SLP and westerlies (Fig. S3.6b & S3.7b), further confirming the role of winter variability driven by the thermal gradient (e.g. the contrast in temperatures between the Artic and the equator).

Apart from the shifts in the large-scale atmospheric circulations, the warmer MIS3 interstadial is also associated with abrupt changes in large-scale ocean circulation like the AMOC strength which is linked with the ice sheet meltwater discharge into the North Atlantic. Our study showed that the AMOC is stronger for the MIS3 interstadial compared to the stadial by ~16Sv (Fig. S3.9b). This simulated strengthened AMOC is generally considered to transport warm and salty water into the subpolar North Atlantic, reducing the sea ice which includes a range of self-amplifying feedbacks that is debated to influence the atmospheric moisture levels (Srokosz *et al.*, 2012; Van Meerbeeck *et al.*, 2011). The role of the Eurasian ice sheet melting as key for CS transgression during the second part of the MIS3 remains unproven and recently rejected by Tudryn *et al.* (2016) as ice sheet growth was smaller during MIS3 (when compared with the LGM and MIS4). In addition, the GLAC-1D data used in our study also suggest a smaller Eurasian ice sheet and agree with the previous study as well as Van Meerbeeck *et al.* (2009); Van Meerbeeck *et al.* (2011). Our result indeed suggests that the maximum ice sheet margin was too far from the Volga catchment area to have a large impact during this period (Fig. 3.2c).

We identify MIS3 interstadial as responsible for the occurrence of a CS transgressive event. The climatic conditions during the interstadial (compared to the stadial) shows a warmer and wetter (drier) climate over the CS northern (southern) catchment area. Our results suggest the enhanced thermal driven precipitation over the North Atlantic and the larger CS region as the main factor for the onset of favourable conditions of the early *Khvalynian* transgression (~33-36 kyr BP) that could have reached an extreme CSL (~+50 m.asl) (Arslanov *et al.*, 2016;

Yanina, 2014). However, the precise timing and extent of this high stand is heavily contested, with no existing radiocarbon dating of the maximum extent, and is argued to be closely followed by a low stand. Recently, Sorokin *et al.* (2018) also linked the warmer MIS3 interstadial (30-21 kyr BP) to increased river discharge into the CS that ensured the onset for early *Khvalynian* transgression stage. In the next section, our modeling results focus on the geological conclusions of the *Elton* regression; that is recognized to divide the early and late *Khvalynian* transgressive phase (Dolukhanov *et al.*, 2009; Yanina, 2014).

3.3.3 LGM climate anomalies and the *Elton?* regression event

We compare the colder LGM conditions to the previous warmer MIS3 interstadial so that our simulated results can constrain the timing and the climate conditions favorable for a smaller CS surface area during the LGM, which presumably corresponds to the *Elton* regression. Concerning the glacial climate of the LGM, our study confirms an east-west dipole in surface temperatures with colder, more arid conditions over the CS catchment area compared to the previously discussed MIS3 interstadial (Fig. 3.5). The LGM reveals colder temperatures of up to <-12°C around Europe and the Eurasian ice sheet, as well as the entire CS catchment area (with temperatures ranging between -10 and 1°C) (Fig. 3.5a). The Eurasian ice sheet elevation (Fig. 3.2b) clearly affect the precipitation anomalies, resulting in a north (drier)-south (wetter) dipole pattern over the ice sheet location (>0.5mm/day along the southern ice sheet margin) as well as over the CS catchment area (Fig. 3.5b); as drier over the Volga basin (-0.2mm/day) and wetter over the southern area (0.2mm/day).

The annual decreased evaporation over southern ice sheet margin and enhanced over the North Atlantic (Fig. S3.3c) lead to the associated changes in the P-E that indicate an increase in precipitation over Europe (with P-E values >0.5mm/day) (Fig. 3.5c). Over the CS catchment area P-E over the Volga decreases (with P-E values ~-0.4mm/day) and the southern CS experience higher P-E values. We attribute this to a climatically low precipitation over the northern CS catchment area that is linked with changes in the ice sheet elevation and perhaps a slightly stronger AMOC (~1-2Sv; Fig. S3.9c). The aridity of this region can be also explained by the declined total precipitable water in the atmospheric column (Fig. 3.5d). Interesting, the winter SLP depicts a different structure, with a more east-west alignment of the centres of action (similar to Justino & Peltier (2005)) with a stronger pressure gradient over the North Atlantic resulting in the corresponding enhanced east-west dipole patterns in the winter zonal

winds at the 850 hPa level (>5m/s) and vice versa for the southern CS catchment area (Fig. 3.5e & f). It is very interesting to note this east-west dipole SLP patterns under glacial climate, unlike the north-south dipole SLP patterns seen for present day interglacial climate. An explanation for this considers that at LGM, the ice sheet over Eurasia and the orbital enhanced snow and sea ice at higher latitude affect the mean winter SLP variability, that can result in this east-west SLP pattern (Otto-Bliesner *et al.*, 2006).

The LGM ice sheet is primarily responsible for controlling most of the northern hemisphere via the large-scale atmospheric and regional precipitation changes over the CS catchment area. Our results confirm the annual precipitation pattern is controlled by the winter precipitation (Fig. S3.2c) that is associated with a southward shift in the winter westerly winds (Fig. 3.5f), as well as the winter storm tracks (Fig. S3.4c) likely orographically forced by the ice sheet elevation. The winter SLP and zonal wind patterns at the 850 hPa level are responsible for the annual mean patterns seen in the SLP and the zonal wind (Fig. S3.6c & S3.7c). The strong cooling by the LGM ice sheet elevation is associated with a reduced atmospheric moisture over this region and southward shift of moist from the Atlantic flows towards the southern CS, leaving the northern area dry. A southward shift in the storm track is also apparent in various paleoclimate simulations (Kageyama *et al.*, 2013; Kageyama *et al.*, 1999; Pausata *et al.*, 2011) and despite the overall cooling during the LGM, can explain the enhanced precipitation over southern CS area.

Concerning the LGM ice sheet evolution for this region, the GLAC-1D data show that the maximum ice sheet was extending as far as the north-western Volga catchment margin with an elevation of >~2400 m.a.s.l (Fig. 3.2b). This agrees well with recent reconstructions that confirm the south-eastern extent of the Scandinavian Ice sheet (SIS) during the LGM (Akesson *et al.*, 2018; Hughes *et al.*, 2016; Stroeven *et al.*, 2016) and also continuous permafrost covered the Russian Plain, Volga catchment area up till the north CS shoreline (Tudryn *et al.*, 2016; Yanina, 2012). Our results present climate conditions favourable for a smaller CS surface area, with a negative water budget and is consistent with other modeling studies which indeed show a negative water budget for the CS during the LGM (Arpe *et al.*, 2011; Arpe *et al.*, 2018; Kislov & Toropov, 2007). Hence, our simulated climate conditions are favourable for the occurrence of a CS regression; similar to the reconstruction of Yanina (2014).

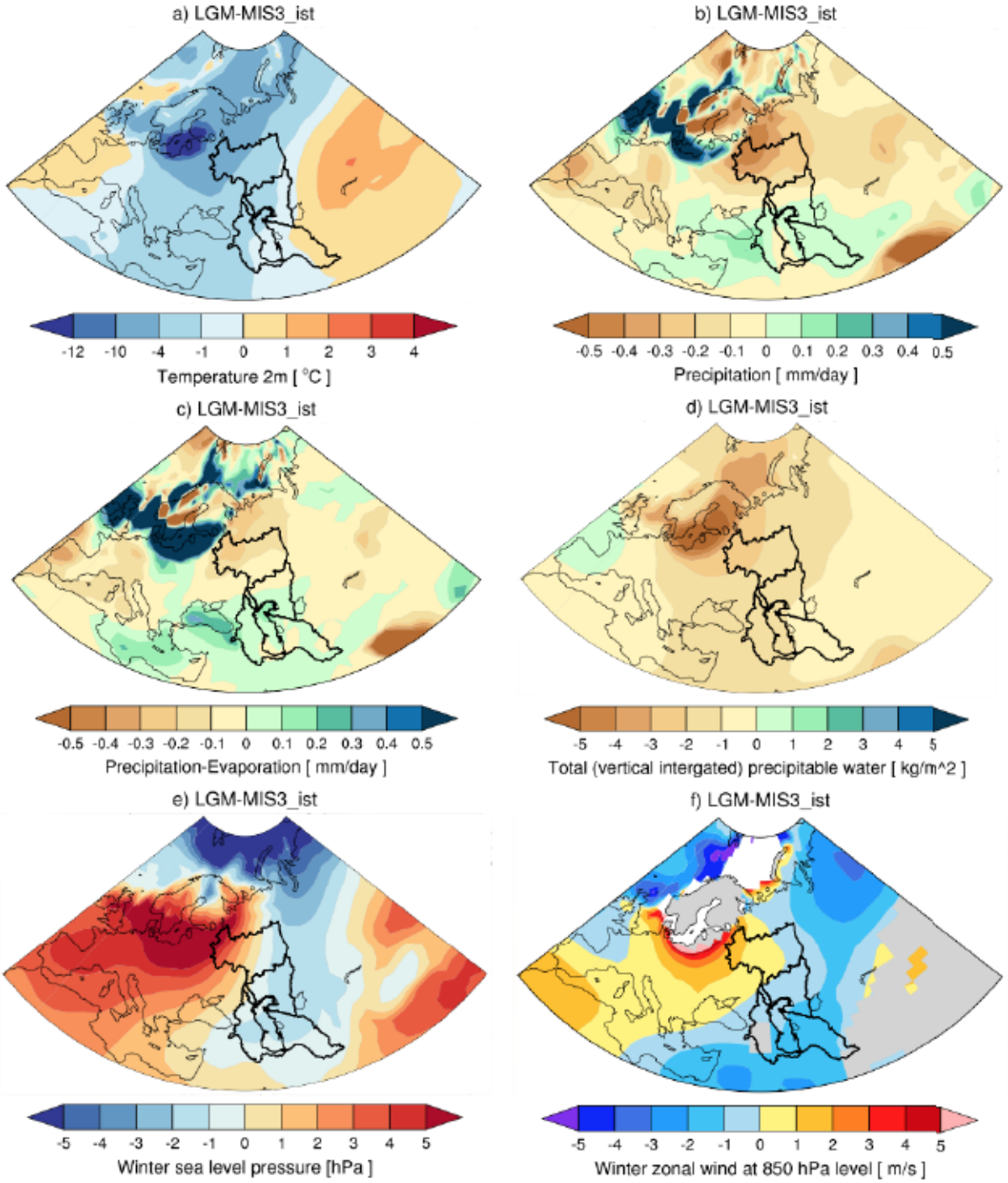

Figure 3.5: Climate conditions for the last Glacial Maximum. Same as Fig.3.3 but for the Last Glacial Maximum (LGM) relative to the MIS3_ist values.

3.3.4 Early and Late stages of H1 versus LGM climate anomalies and the late *Khvalynian* transgression event

Our next modeling results share key insights into climatic processes during the last deglaciation (which spans the early and late stages in the Heinrich event1 (H1)) that likely correspond to the late *Khvalynian* transgressive phase. Here, our simulated results for the early and late stages

of H1 are relative to mean changes in the simulated LGM climate. Quite interestingly, the early and late stages of H1 exhibit the strongest decrease in temperature and precipitation over the North Atlantic, Europe, the Volga basin and the CS catchment area (Fig. 3.6a-d). This is particularly true for the early stage H1 (when compared with the LGM or the late stage H1), implying enhanced cold and arid conditions over the CS. Since much of the Eurasian region underwent large changes in ice sheet melting, the different climate conditions during the early and late stages of H1 appear to be interesting for the CS hydrological development, relative to the previously seen LGM climate. During the early stage H1 climate conditions were colder and drier over the North Atlantic (>-20°C; >-0.5mm/day), Europe and the CS catchment area (>-8°C; <-0.2mm/day) (Fig. 3.6a, c); compared to the LGM climate. Compared to the early stage H1, the late stage of H1 shows a climate that was slightly warmer and less dry over the catchment area (~-4°C; <-0.1mm/day), but was still colder and drier almost everywhere in comparison with the LGM (Fig. 3.6b & d). When compared with the LGM climate, the P-E water budget during early stage H1 show lower P-E values over the Volga basin, the EEP, Europe and the North Atlantic (Fig. 3.6e), which is shifted to slightly higher values over the EEP and the Volga basin during late stage H1 (Fig. 3.6f). A catchment integrated P-E leads to a negative water budget for the early H1 and a slight positive water budget for the late H1 (Fig. S3.10). The water budget is associated to the availability of the total precipitable water in the atmospheric column during the early H1 (compared to the LGM) (Fig. 3.6g) and for the late H1 (compared with the LGM) (Fig. 3.6h). In both cases, this is likely related to the much-debated changes in the large-scale winter atmospheric circulation, in combination with the complex regional thermodynamics during the ice sheet melting. The annual precipitation pattern over ice sheet location is controlled by the summer precipitation (Fig. S3.1d & e) while the catchment area is dominated by the winter precipitation variability (Fig. S3.2d & e), which in turn is determined from the enhanced winter mean SLP (Fig. 3.6i & j) and north-south dipole strength in the winter westerlies over the northern and middle CS catchment area (Fig. 3.6k &l; at the 850 hPa level). From this, it is clear that a primary dipole exists over the ice sheet location, that can influence a secondary dipole seen for the intensified westerlies.

Of particular interest in the light of transgressions and regressions are the different climate states seen during the early and late stages of H1, which appear to impact the CS catchment climate and the CS surface area changes differently. Compared to the LGM climate, the early H1 suggests colder, drier climate over the larger CS catchment area, mainly driven by the ice sheet and a weakened AMOC (Fig. S3.9d). The late H1 stage, when compared to the LGM,

suggest slightly less cold, drier climate influenced by slightly warmer temperature and ice sheet melting. The implications from a reduction in the AMOC strength during H1 (Fig. S3.9d & e; ~>24Sv) are under intense debate and in-depth analysis have not been performed to link the effects on atmospheric moisture transport.

The reconstructed CS transgressions during the late Khvalynian transgression (~16-14 kyr BP with CSLs of +35 and +22 m a.s.l (Arslanov *et al.*, 2016)) is very likely driven by the melting from the SIS into the eastern part of the Russian plain during the deglaciation (which continued from the LGM and finished at 13.8 kyr BP) (Tudryn *et al.*, 2016). The age constraints for the (early and late stages) *Khvalynian* transgression event came to an end spanning the period 35 kyr BP - ~10kyr BP (Krijgsman *et al.*, 2019). These highstands are confirmed by an overflow of CS water into the Black Sea via the Kuma-Manysch strait (22m a.s.l) during this time that stopped at ~12.8 kyr BP (Chepalyga, 2007; Tudryn *et al.*, 2016). Examining this margin in our model, we see that the maximum ice sheet margin at 15.2 kyr was indeed into the eastern part of the EEP and overlapping the north-western CS catchment area. This potentially routes the melting water inside the Volga (northern CS catchment). Hence, it is clear that this meltwater is the main source for the highstands confirmed by reconstructions. Compared to the LGM, the early H1 suggest a CS regression, solely suggested by atmospheric arid conditions. The late H1 climate conditions are slightly warmer, and moist over the ice sheet location and appear to provide ideal conditions for deglaciation and is highlighted by the flowing of meltwater into the Volga catchment area which seems highly probable given our modelled and the GLAC-1D data (Fig. 3.2a; Fig. 3.6b, d). However, our simulated study did not account for meltwater routing into the CS that makes the comparisons with the selected reconstructions complicated. Despite the above limitation, the climatic conditions for the early stage H1 show colder, drier conditions (accounting for large shifts in mid latitude storm tracks), with a switch to less cold and arid conditions and less intense storm tracks during the late H1 stage when compared to the LGM (Fig. S3.4d & e).

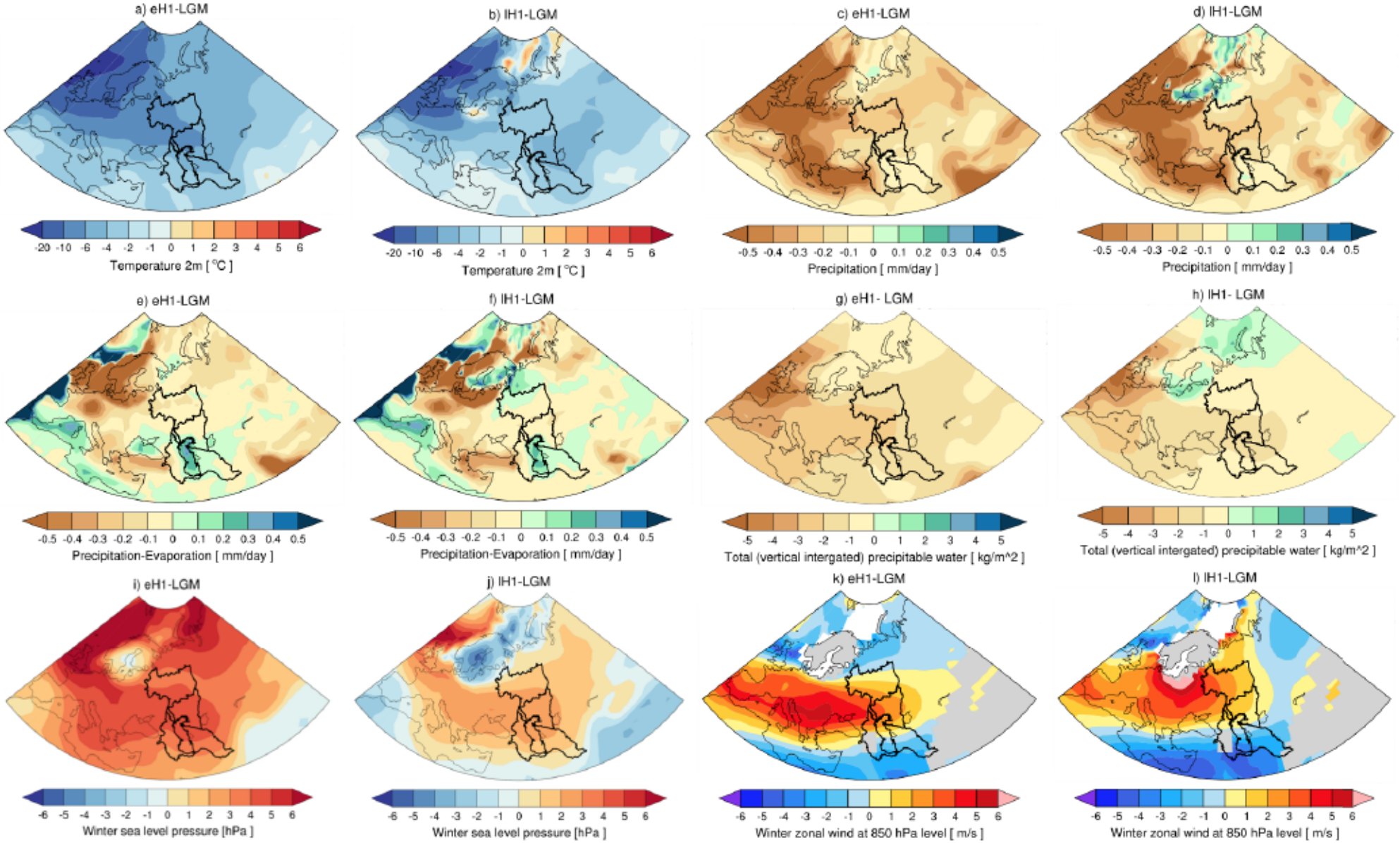

Figure 3.6: Same as Fig. 3.3 but for the early (left column) and late (right column) stages of Heinrich Event 1 (eH1; lH1) relative to the LGM.

3.3.5 The early Holocene interglacial climate anomalies (post-*Mangyshlak* regression)

Soon after the end of the *Mangyshlak* regression (that lasted between one and three millennia over the entire CS catchment area) (Bezrodnykh & Sorokin, 2017; Rychagov, 1997; Yanina, 2014) a high stand is proposed to occur in the first part of the Holocene; this highstand is called the post-*Mangyshlak* highstand in Leroy *et al.* (2019). Here, our new simulated results will be discussed to give contribution on the favorable climate conditions and the timing for onset of a larger CS surface area that occurred after the *Mangyshlak* regression. Our results for the early Holocene (EH) (defined with the orbital conditions for the 9 kyr BP in our simulation) are in comparison to the PI climatic conditions and include generally cooler conditions over the entire CS catchment area and drier over the Russian plain and Volga basin, while being wetter elsewhere (Fig. 3.7a-b). During the early Holocene, temperatures were higher over Europe by >0.5°C, but colder (<-0.5°C) over the CS catchment area (Fig. 3.7a), emerging in an east-west dipole pattern. The annual mean precipitation includes a north-south dipole pattern over the region with drier over Europe, northern CS catchment area (of ~-0.1 mm/day) and increased over the middle and southern areas by 0.2 mm/day (Fig. 3.7b). Interestingly, this north-south dipole over the northern and southern CS catchment areas favour a reversed salinity gradient as shown in Leroy *et al.* (2019). The corresponding P-E pattern resembles the precipitation pattern (Fig. 3.7c). The regional annual precipitation patterns seen are due to the summer mean precipitation (Fig. S3.1f) which can be linked to the total precipitable water (Fig. 3.7d) and a decrease summer SLP and north (increased)-south (decreased) dipole in the summer westerlies at the 850 hPa level (Fig. S3.5c & d) that control the wetter conditions around southern CS and drier over northern CS. Similar to the discussion for the LIG, we suggest the EH the enhanced precipitation over the southern CS area is primarily related to summer convective precipitation, triggered by the enhanced insolation that destabilizes the atmosphere. Additionally, given the impact of North Atlantic winter variability over this region, we note the enhanced pressure gradient over the entire catchment area (Fig. 3.7e) and the southern shifted weakened winter mean westerlies at the 850 hPa level; denoting a negative NAO-like pattern. These patterns are also somewhat similar to the LIG and we see a combined effect of a smaller thermal gradient, pressure gradient and thermodynamics on the CS catchment that results in a small increase in P-E anomaly, denoting a slightly large CS surface area.

The climatic conditions during the EH show a cooler condition with drier (wetter) P-E values over the northern (middle and southern) catchment area. Our simulated results suggest the onset

of a transgression, which can lead to the highstand confirmed by Leroy *et al.* (2019). This high stand likely relates to an enhanced paleo Indian summer Monsoon driving freshwater discharge through the paleo Amu Darya river and the paleo *Uzboy* channel to the east of the CS (Turkmenistan) (Leroy *et al.*, 2019; Leroy *et al.*, 2014; Leroy *et al.*, 2013).

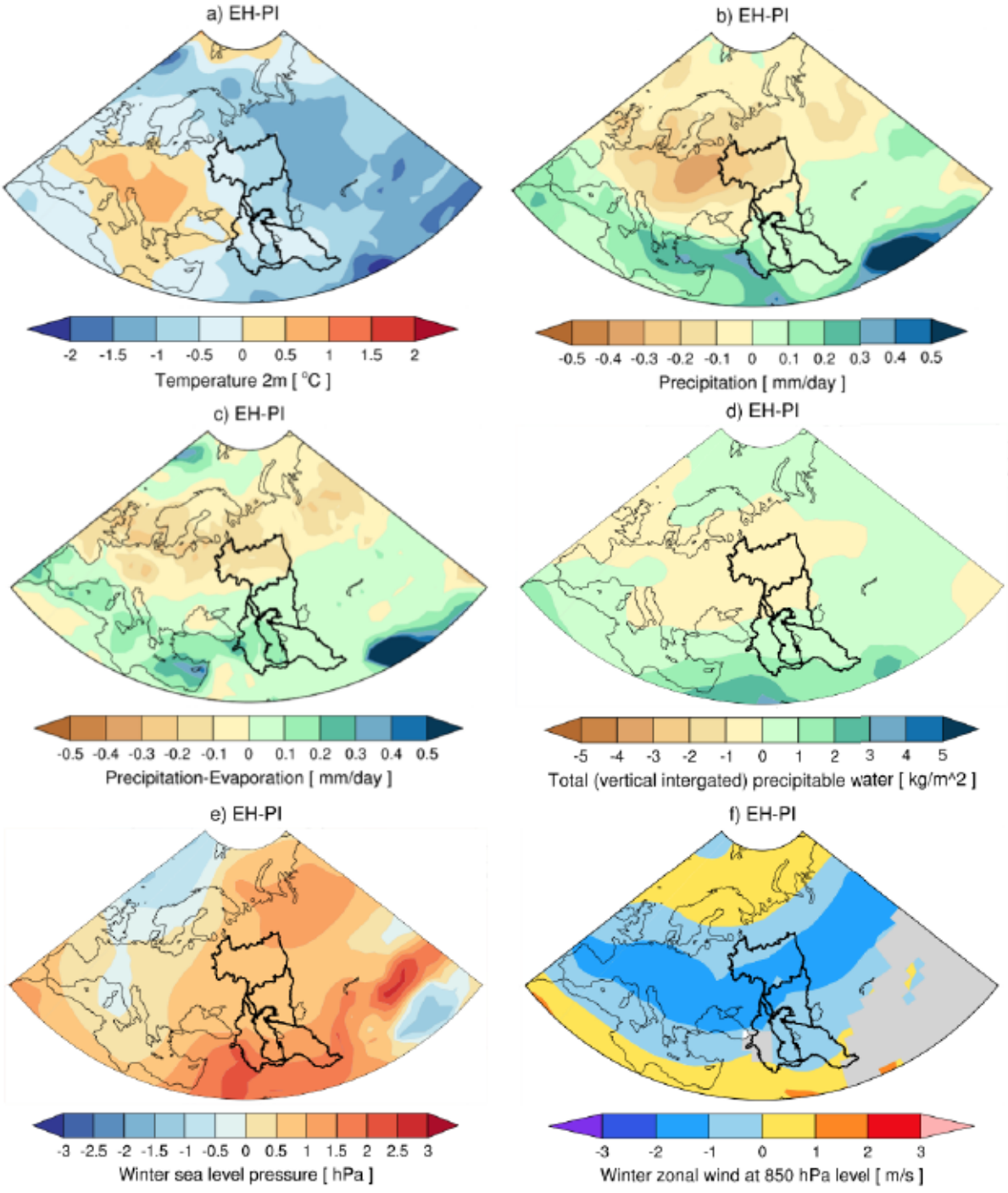

Figure 3.7: Climate conditions for the Early Holocene. Same as Fig. 3.3 but for the early Holocene (EH) relative to the PI values.

3.3.6 CESM Annual water budget (P-E) anomalies and comparisons with reconstructions

Here, we analyze the water budgets of the glacial experiments MIS3_ist, MIS3_st, eH1, and lH1 as anomalies relative to the LGM, and the water budgets of the interglacial experiments LIG and EH as anomalies relative to PI.

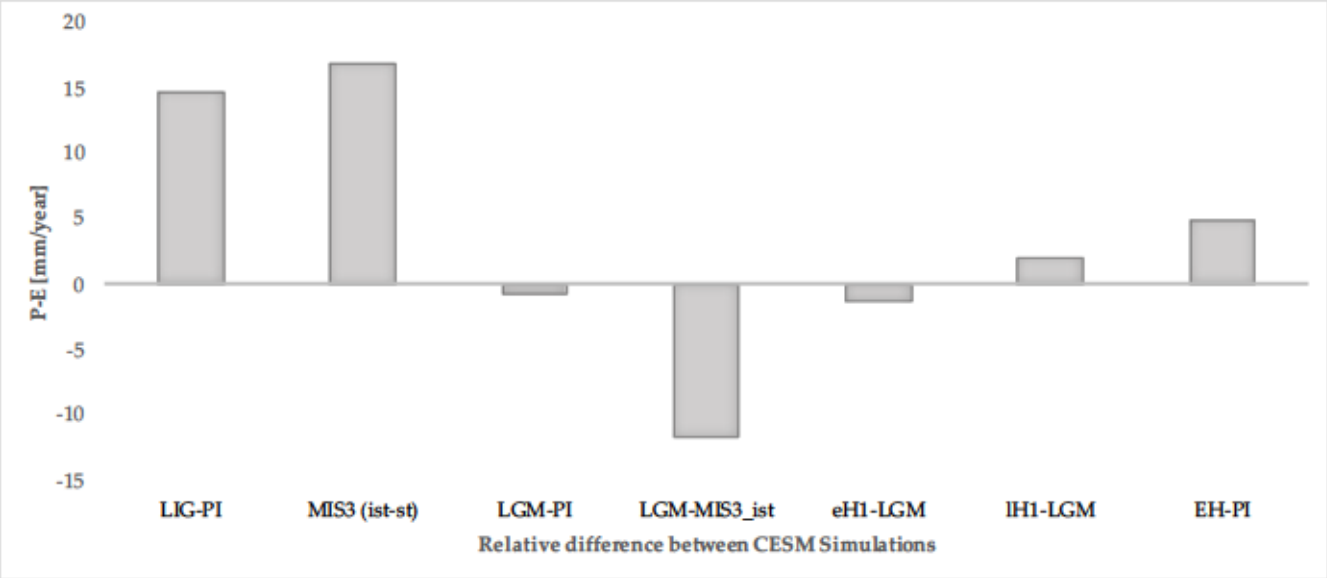

Figure 3.8: Annual mean changes in the CS water budget. Annual mean precipitation minus evaporation (P-E in mm/day) for the Last Interglacial (LIG) relative to pre-industrial (PI), the Early Holocene (EH) relative to PI, the Last Glacial Maximum (LGM) relative to PI, Marine Isotope Stage 3 interstadial (ist) relative to LGM, the MIS3 stadial (st) relative to LGM, Early Heinrich event1 (eH1) relative to LGM and the Late Heinrich event1 (lH1) relative to LGM climate conditions for the entire Caspian Sea and its catchment area.

Regarding the interglacial climate states, a positive anomaly in the water budget (defined as the mean annual P-E averaged over the CS catchment area) is simulated for the LIG (Fig. 3.8). The LIG has a positive water budget anomaly (P-E=14.6 mm/year) relative to pre-industrial conditions, denoting higher precipitation than evaporation over this region. Even such a modest P-E change can lead to a large increase in CSL of 14.6 meter/1000 years, not even taking ice-sheet dynamics into consideration. The EH experiment also shows a positive anomaly (P-E= 4.8 mm/year), albeit smaller than for the LIG (Fig. 3.8). Noteworthy is that the smallest (negative) water budget change relative to the pre-industrial occurs for the LGM (P-E= -0.73 mm/year), which proves interesting given the small CS area in our LGM simulation compared with the pre-industrial. As to the other glacial climate states, the largest positive water budget is found for MIS3_ist (P-E= ~16 mm/year), when compared with the stadial climate of MIS3st; that can potentially lead to a CSL increase (16 meter/1000 years). The largest negative water budget anomaly occurs for the LGM (P-E= -11.68mm/day) when compared with the previous

MIS3 interstadial climate that can lead to a CSL decline (-11.68 meter/1000 years); Our model further suggests different hydroclimatic conditions between the early (eH1) and late (lH1) phases of H1 over the CS catchment area. Compared to the preceding LGM climate, the early H1 shows a negative water budget (P-E= -1.34 mm/year) implying less net precipitation (P-E), whereas the late H1 phase shows a positive water budget anomaly (P-E= 1.9 mm/year) (Fig. 3.8).

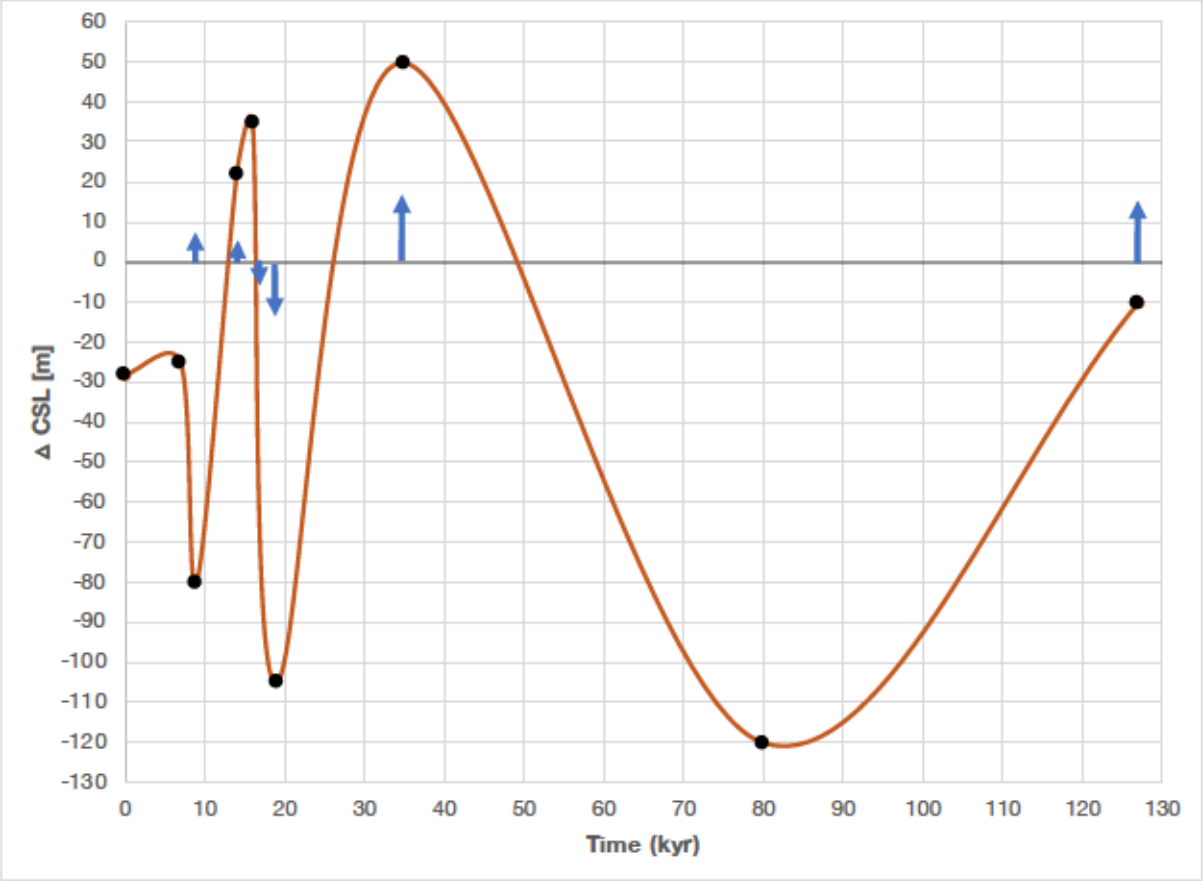

Figure 3.9: CESM modeled P-E versus the Reconstructions. Schematic interpretation of the change in CSL based from CESM model P-E results and the selected reconstructions after (Krijgsman *et al.*, 2019). Annual mean rate of change in the CSL in meter for CESM model (catchment-integrated P-E in m/1000yr) and reconstructions for MIS5e, MIS3, LGM, eH1, lH1 and EH. Note reconstructions with uncertainty range is detailed in Krijgsman *et al.* (2019).

Overall our new simulated results of catchment integrated P-E anomalies are discussed with the selected reconstructions for the CS transgressions and regressions; bearing in mind the model limitations (Fig. 3.9). To this end, we indicate the positive/negative P-E anomalies with up/down arrows as a representation for an increase/decrease in the CS surface area change and compare to the selected reconstructions after (Krijgsman *et al.*, 2019). Based on paleo timescales, we begin with the last interglacial at 127 kyr; here our simulated P-E show a

positive water budget and agree with the reconstructed transgressive nature of the MIS5e. Next, an increase in P-E anomaly confirm agreement with the reconstructed transgression during MIS3 at ~35kyr. Subsequently, both the model and reconstructions agree for the occurrence of a regression event during the LGM climate at ~19kyr. However, during the deglaciation period, our simulated P-E anomalies does not capture the reconstructed highstand at 16 kyr BP. Instead it only captures one highstand, during the end of the deglaciation (14 kyr BP) which marks as the late Heinrich event 1 in our simulations. Our simulated study did not account for meltwater routing into the CS that makes the comparisons with the selected reconstructions complicated. Our simulated water budget are not solely sufficient to explain the magnitude of the two reconstructed high stands at 16 and 14 kyr BP, as modelers still need to understand how meltwater is routed to the CS during the deglaciation. The last comparison between the model-reconstruction points to the early Holocene climate period, whereby the simulated positive P-E anomaly related to the onset of transgressive behaviour after the end of the regression at ~9kyr and agrees to Leroy et al. (2019).

Lastly, our modeling study includes some caveats which were also determined by internal variability, which strongly depends on specific physical boundary conditions, such as land-ocean and sea-ice distribution and topography. Even though the global sea levels were higher during MIS3 compared to LGM, all glacial simulations were setup with a 120m lowering of the sea levels (a standardized method used in many studies like Van Meerbeeck *et al.* (2009)) and included a smaller CS surface area. Our CESM interglacial simulations, including the pre-industrial simulation, include a prescribed CS area which is larger than the actual CS area. The climatic biases of involving a smaller or larger CS area have major impacts on the surrounding CS catchment climate as well as the large-scale climate in the northern hemisphere revealed in Arpe et al. (2018); and Nandini et al. (revised). The absence of the ice sheet meltwater routing in to the CS and leaving aside potential changes in river hydrography, as well as the changes in the AMOC strength which are needed to provide constraints on the timing and magnitude of CS hydroclimate changes, can be stronger in reality when compared to our simulated results; since only simulated precipitation and evaporation results can not reveal the sole climatic conditions favorable for the onset of major CS transgressions and regressions. Nevertheless, our modeling study shares key insights on identifying the impacts from different climate processes that can trigger a CS transgression or regression.

3.4 Conclusions

We present new modeling results that identify climate processes responsible for hydroclimate (precipitation and evaporation) changes in the Caspian Sea which is associated with the major transgression and regressions, leaving aside potential changes in river hydrography, based on selected glacial and interglacial climate states spanning the Late Quaternary and compared them with selected geological reconstructions. Our new modeling results contribute in constraining the timing for the Caspian Sea transgressions and regressions as well as the climate conditions favourable for the occurrence of these events.

The interglacial climate states from our study suggest favourable climate conditions (higher temperature and precipitation) for the CS that result in a positive water budget (precipitation minus evaporation; P-E). In comparison with the pre-industrial climate conditions, the last Interglacial period results in P-E anomalies of 14.6 meter/1000 years and the early Holocene marks P-E anomalies ~5 meter/1000yr; suggesting a larger Caspian Sea area and agrees with the reconstructions that confirm a mild transgression event. Our early Holocene simulation relates to the post- *Mangyshlak* regression and includes conditions for a larger CS that agree with the highstand suggested by Leroy et al. (2019). Our results suggest that the above two interglacial periods are impacted by large-scale and convective summer precipitation triggered by enhanced summer insolation and the associated wind anomalies, such as the southern shift in the strength and the position of the mid latitude winter westerly winds and storm tracks. This controls the annual mean precipitation that is responsible for drier conditions over the northern CS catchment area and wetter conditions over the southern area.

The glacial climate states include the combination of abrupt orbital induced insolation changes in the winter large-scale atmospheric circulation for the pressure gradient and enhanced westerlies contributing to the precipitation patterns; however, the summer ice sheet melt discharge into the Caspian Sea and the Atlantic and changes in the Atlantic Meridional Overturning Circulation strength plays a primary role. The warmer and wetter Marine Isotope 3 (MIS3) interstadial climate results in the largest positive water budget of P-E anomalies of 16 meter/1000yr; driven by enhanced thermal driven winter precipitation over the North Atlantic and the larger CS region. We identify the MIS3 interstadial climate responsible for a larger CS surface area; similar but smaller in magnitude to the reconstructions for the early *Khvalynian* transgression. When compared to the previous MIS3 interstadial climate, a colder

and drier Last Glacial maximum (LGM) climate includes a negative water budget of catchment integrated P-E of ~-12 meter/ 1000yr that leads to a CS regression, which is analogous to reconstructions. Based on GLAC-1D ice sheet data, during the deglaciation (our simulated early and late stages in the Heinrich event 1), it is clear that insolation-controlled changes in the ice sheet meltwater is responsible for the two reconstructed high stands seen at 16 and 14 kyr. Here, our P-E anomalies only capture the conditions for one highstand, since the model does not include a sophisticated meltwater routing into the CS, making comparisons with the selected reconstructions complicated. Our simulated results do however show that in comparison with the LGM conditions, the early H1 shows much colder and drier conditions which switches to slightly less cold and dry during the late H1.

Our time-slice simulated results suggest that the accumulation of P-E anomalies over a longer timescale can result in changes in the Caspian Sea surface area that can correspond to similar magnitudes in the reconstructed transgressive-regressive behaviour for Caspian Sea under the late Quaternary. However, this is not true for the transient climate periods that are solely driven by orbital induced ice sheet growth/ melting or including large changes in paleo river hydrography around the larger Caspian Sea region. Hence including only, the simulated P-E anomalies or the atmospheric-ocean circulation processes are not sufficient to explain the full nature of the major transgressions and regressions. Importantly, our model results can also be utilized for both, other modeling and paleoclimate reconstruction studies, which attempt to better interpret the nature of the Late Quaternary Caspian Sea transgressions and regressions with respect to changes in precipitation and evaporation.

Acknowledgements

This project has received funding from the European Union's Horizon 2020 research and innovation programme under the Marie Sklodowska-Curie grant agreement No 642973 (PRIDE) as well as from the BMBF project PalMod. All CESM simulations were performed on the supercomputer of the Norddeutscher Verbund für Hoch- und Höchstleistungrechnen (HLRN-III). The processing charges for this open access publication were covered by the University of Bremen. The authors declare no conflict of interests.

4 Past and future impact of North Atlantic winter teleconnections on the Caspian catchment area in CESM1.2.2

Sri D. Nandini-weiß [1,*], Matthias Prange[1], Klaus Arpe[2], Ute Merkel[1], Michael Schulz[1]

[1] MARUM – Center for Marine Environmental Sciences and Faculty of Geosciences, University of Bremen, Germany.
[2] Max-Planck-Institute for Meteorology, Hamburg, Germany.
Revised in *International Journal of Climatology*

Abstract

The Caspian Sea Level (CSL) has undergone variations of more than 3 m during the past century with important implications for the life of coastal people, economy and the ecosystem. The origin of these variations as well as future changes in the Caspian water budget are still a matter of debate. Here, the major modes of North Atlantic winter climate variability and atmospheric teleconnections that have a potential effect on the hydroclimate of the Caspian catchment region are examined, i.e. the North Atlantic Oscillation (NAO), the East Atlantic Pattern, and the Scandinavian Pattern. The skill of the Community Earth System Model (CESM1.2.2) regarding the simulation of the modern climatology in the Caspian region and the major North Atlantic modes are analysed using different atmospheric grid resolutions and setups of the atmospheric component, the Community Atmosphere Model (CAM4 and CAM5). CESM1.2.2 with CAM5 atmosphere physics and 1° atmospheric grid resolution shows reasonable skill in simulating the North Atlantic winter teleconnections. Using this model version, a weakly positive ($r=0.2$) statistically significant ($p<0.05$) correlation between the catchment winter water budget (precipitation minus evaporation, P-E, integrated over the catchment area) and the NAO is found for the historical period 1850-2000. Climate projections of the 21st century under the Representative Concentration Pathways RCP4.5 and RCP8.5 show that the NAO remains the leading mode of winter variability with a dominant influence on the climate in the Caspian catchment region. Under the RCP4.5 scenario the correlation between the winter NAO and winter P-E over the Caspian catchment region increases ($r=0.5$, $p<0.05$). For RCP8.5, however, this correlation disappears due to a north-south dipole pattern with a positive P-E anomaly over the northern and a negative anomaly over the southern parts of the Caspian catchment region, cancelling out an effect on the total Caspian water budget. Nevertheless, due to increasing annual evaporation over the Caspian Sea in the warming climate, the model predicts an additional CSL decrease of about 9 m and 18 m between 2020 and 2100 for the RCP4.5 and RCP8.5 scenarios, respectively. Even though the model tends to overestimate the total evaporation due to a too large Caspian Sea surface area, these values are larger than previous projections of CSL decline.

4.1 Introduction

The Caspian Sea (CS) is the world's largest inland sea and located within a closed (endorheic) drainage basin (Fig. 4.1). The CS is nestled between eastern Europe and Central Asian semi-arid regions, northern flat terrains and Caucasus high mountain ranges. The CS catchment basin (covering ca. 3.7 x 10^6 km^2) is ca. 10 times larger than the CS itself, and includes more than 130 rivers feeding into the lake (Arpe *et al.*, 2018; Rodionov, 1994). The Volga river is the main inlet (~80-90% of total river discharge into the CS) and covers the northern CS catchment basin (Leroy *et al.*, accepted). The other major river basins include Ural, Terek and Kura. The CS basin is rich in ecosystems, large river systems, and major wetlands and features high level species endemism and diversity (Kosarev, 2005). Therefore, climatic changes in this region may have a strong environmental impact.

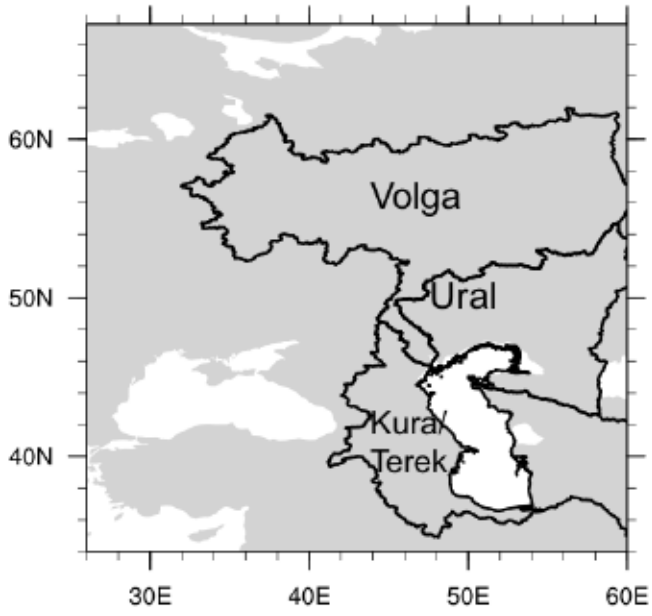

Figure 4.1: Study Area. Caspian catchment area and major river basins outlined in black.

The CS has experienced drastic lake level changes due to climate and hydrological processes in the last 150 years (Arpe *et al.*, 1999; Arpe & Leroy, 2007; Chen *et al.*, 2017; Kroonenberg *et al.*, 2008). Currently, the Caspian Sea Level (CSL) is ~28 m below zero (i.e. the global sea level). However, during the past 150 years, large and rapid fluctuations of ~4 m in CSL (-25 to -29 m) had strong consequences for coastal communities. The drivers for these changes are not fully understood and heavily debated (Arpe *et al.*, 2000; Arpe & Leroy, 2007; Elguindi & Giorgi, 2006b; Golitsyn *et al.*, 1990; Panin & Dianskii, 2014; Panin *et al.*, 2014; Rodionov, 1994). However, numerous observational and modeling studies suggest that variations in the

CSL are mainly driven by climate-induced changes in the Volga river runoff and surface fluxes (precipitation minus evaporation, P-E) over the CS (Chen *et al.*, 2017; Elguindi & Giorgi, 2007; Kroonenberg *et al.*, 2008; Panin *et al.*, 2014; Panin *et al.*, 2015; Yanina, 2014). Due to the CSL's sensitivity to hydroclimatic changes, future risk assessment and the development of adaptive strategies are of particular importance in the CS region.

Atmospheric circulation features influencing the CS catchment area include the mid-latitude westerly winds and, at upper tropospheric levels, the polar and subtropical jet streams (Molavi-Arabshahi *et al.*, 2015; Rodionov, 1994). Several air masses affect the regional climate, i.e. cold air from the Arctic, moist temperate air masses from the Atlantic Ocean, warm subtropical air masses arising from the Black Sea, and dry continental air masses from the east. Hence, the northern CS resides in a continental climate zone, whereas the central and southern CS is located in a warm and dry climate belt. Given this complex climatological setting, the seasonal cycle of precipitation varies strongly over the different regions of the catchment area, with maximum precipitation in summer over the northern part (Volga basin), in spring over the western part (Kura/Terek area), and in autumn-winter over the southern CS (the eastern CS coastal area is a desert). Evaporation over the CS is highest in autumn (September) (Rodionov, 1994).

Major winter North Atlantic teleconnection patterns are known to impact European climate and include the North Atlantic Oscillation (NAO), the East Atlantic (EA) pattern and the Scandinavia (SCA) pattern (Barnston & Livezey, 1987; Hurrell, 1995; Panin & Dianskii, 2014). Although the NAO, EA, and SCA patterns undoubtedly have a strong impact on European winter climate, their influence on the hydrology of the Caspian catchment region and hence the CSL is controversial. While Rodionov (1994) discusses possible effects of the NAO on the CSL and Panin & Dianskii (2014) as well as Panin *et al.* (2015) argue in favor of NAO-driven CSL changes based on correlations between NAO and precipitation, other studies could not find a stable connection between NAO and CSL, but instead suggest a role of the El Niño-Southern Oscillation (ENSO) in driving CSL variations (Arpe *et al.*, 2000). Recent studies have evaluated the ability of climate models to reproduce teleconnection patterns and revealed biases in representing physical processes and shifts in the position and magnitude of the centres of action that impact regional surface temperature and precipitation (Davini & Cagnazzo, 2014; Lee & Black, 2013; Ning & Bradley, 2016; Stoner *et al.*, 2009). These studies emphasize the

need to consider teleconnection biases in projections of future climate change and their relationships with regional winter climate variability.

Moreover, projections for the 21st century CSL change remain contradictory since much depends on the model physics and resolutions and the key underlying assumptions that lead to different results (Arpe & Leroy, 2007; Elguindi & Giorgi, 2006a; Elguindi & Giorgi, 2006b; Renssen *et al.*, 2007). CSL predictions were performed based on global (Arpe *et al.*, 1999; Kislov *et al.*, 2014; Kislov & Toropov, 2007; Renssen *et al.*, 2007) and regional models (Elguindi & Giorgi, 2006b, 2007). Using a global model and projections based on the IPCC A1B scenario, Renssen *et al.* (2007) show a CSL decline of 4.5 m by 2100. Projections based on the IPCC A2 scenario suggested a CSL decline of at least five meters by 2100 (Elguindi & Giorgi, 2007). Interestingly, by using an ensemble of different atmosphere-ocean general circulation models (AOGCMs) forced by the same A2 scenario, a CSL drop of about nine meters by the end of 2100 was found (Elguindi & Giorgi, 2006a). Other models suggested a stable or even increasing CSL (Arpe & Leroy, 2007). Hence, it is essential to consider biases from model setups and resolutions to improve our understanding regarding the physical mechanisms behind future CSL variations.

In the present study, we investigate the potential role of North Atlantic winter teleconnections in driving regional Caspian climate variability and CSL variations with the coupled general circulation model CESM1.2.2. Given the potential sensitivity of simulated teleconnections and hydroclimatic variations to model physics and grid resolution as mentioned above, we carry out a model evaluation to select the best model version with respect to atmosphere physics and horizontal resolution to represent the CS catchment climate. We also investigate the changing influence of these winter teleconnections on the Caspian region hydroclimate under global warming for the period 1850-2100. Moreover, we provide first-order estimates of the projected CSL change under two emission scenarios by the end of the 21st century.

4.2 Methodology and Data

4.2.1 CESM1.2.2 Model and Experimental Design

The Community Earth System Model CESM1.2.2 is a fully coupled global climate model (Hurrell *et al.*, 2013). Its development is coordinated by the National Centre for

Atmospheric Research (NCAR), Boulder, Colorado. The coupled components include a physics based atmospheric model (Community Atmosphere Model, CAM4 or CAM5), a land-surface model (Community Land Model, CLM4.0) (Lawrence *et al.*, 2011), an ocean general circulation model (Parallel Ocean Program, POP2) (Smith *et al.*, 2010), a dynamic-thermodynamic sea ice model (Community Ice CodE, CICE4) (Hunke & Lipscomb, 2010) and a River Transport Model (RTM at 0.5° resolution) (Gent *et al.*, 2011). The models are coupled through the CESM1.2.2 flux coupler (CPL7). The CESM1.2.2 ocean and ice models share the same horizontal grid. The horizontal resolution of this grid varies and is higher around Greenland, with the North Pole displaced, as well as around the equator. In all our experiments, we use a nominal 1° resolution of the ocean/sea-ice grid. The ocean model grid has 60 levels in the vertical.

CESM1.2.2 can be run with different atmospheric grid resolutions and physics packages (CAM4 and CAM5). CAM5 differs from CAM4 by simulating full aerosol-cloud interactions and hence indirect radiative effects. It includes improved moist turbulence, shallow convection, cloud micro- and macrophysics, and aerosol schemes (see Neale *et al.* (2012) for details). CAM4 runs with 26 levels in the vertical, while four levels were added for a better representation of the boundary layer in CAM5. To evaluate which model version performs best with regard to CS basin climatology and North Atlantic modes of variability, we carried out three control transient experiments (Table 4.1) using different atmospheric grid resolutions (2° versus 1°) and model physics (CAM4 versus CAM5) for the historical (1850-2005 AD) period with identical forcings (a combination of anthropogenic and natural forcings; see Gent *et al.* (2011); Meehl *et al.* (2012)) and on the same machine (Cray XC30/40 of HLRN-III). Note that the atmosphere model has a finite volume dynamical core with a uniform horizontal resolution which is shared with the land model grid.

In order to examine potential future changes in the climate of the CS region, two transient experiments were run until the year 2100 under the IPCC scenarios RCP4.5 and RCP8.5 (Meinshausen *et al.*, 2011; Moss *et al.*, 2010; van Vuuren *et al.*, 2011). The RCP8.5 is a high-range scenario with rising greenhouse gas emissions and a radiative forcing of 8.5 W/m^2 by the year 2100 while RCP4.5 is a mid-range scenario that does not exceed 4.5 W/m^2 (Lamarque *et al.*, 2011). Both experiments use the 1° version of CAM5 and were initialized with the final state of the corresponding historical run. Experiments are summarized in Table 4.1.

Table 4.1: CESM1.2.2 coupled model experiments.

Experiment	Resolution: Horizontal grid	Period
Control CAM4	2° (2.5° x 1.9°)	1850-2005 CE
Control CAM4	1° (1.25° x 0.9°)	1850-2005 CE
Control CAM5	1° (1.25° x 0.9°)	1850-2005 CE
RCP4.5 CAM5	1° (1.25° x 0.9°)	2005-2100 CE
RCP8.5 CAM5	1° (1.25° x 0.9°)	2005-2100 CE

4.2.2 Observational/Reanalysis Climate Data

The following datasets were used to assess the model's skill in simulating the climate of the Caspian region and North Atlantic teleconnection patterns. Sea-level pressure (SLP) from 1950-2000 at 2.5° resolution was taken from the National Center for Environmental Prediction (NCEP/NCAR) reanalysis dataset (Kalnay *et al.*, 1996). Gridded (at 0.5° resolution) monthly station time series of land 2-meter temperature (T2m) is taken from the University of Delaware dataset version 4.0.1 (Willmott & Matsuura, 1995) for the period 1900-2000. Mean monthly precipitation, evaporation and P-E reanalysis data at 0.5° resolution was extracted from the reanalysis done at the European Center for Medium Range Weather Forecasts (ECMWF) (Dee *et al.*, 2011) for the period 1979-2000. For the analysis of the total hydrological budget of the Caspian catchment basin, we integrated P-E over the entire basin area up to 60° E where the Karakum Desert (Turkmenistan) is located and river water from further east evaporates and seeps away (Fig. 4.1).

4.2.3 Climate Indices

We apply Empirical Orthogonal Function (EOF) analysis to the observational, reanalysis and model data to extract independent modes of climate variability in the North Atlantic/European region. The NAO, EA and SCA indices in this study are defined as standardized first, second and third principal component time series calculated from seasonal-mean SLP anomalies in the region [70°W-60°E, 20°-80°N], which includes the CS basin. We focus on the winter season, Dec-Jan-Feb (DJF), as the NAO and other modes display their largest climate impact in the boreal winter months (Arpe *et al.*, 2000; Arpe *et al.*, 2014; Hurrell *et al.*, 2013; Hurrell *et al.*, 2003). All data was detrended before performing the EOF analysis. Corresponding EOF maps

(spatial patterns) were obtained by regressing the detrended SLP fields onto the standardized principle component time series (index). The time series of each mode was obtained by projecting the eigenvectors of the SLP covariance matrix onto the latitude-weighted anomalies (North *et al.*, 1982). The signs of the NAO, EA and SCA indices are defined such that a positive NAO phase corresponds to a negative SLP anomaly over Iceland (Hurrell, 1995), a positive EA phase corresponds to a positive SLP anomaly over the Northeast Atlantic (Barnston & Livezey, 1987) and a positive SCA phase is related to a positive SLP anomaly over Scandinavia (Aondover, 2013; Bueh & Nakamura, 2007). Analyses were performed with the NCL software.

4.3 Results

4.3.1 Simulation Skills of CESM1.2.2 for the Modern Climatology of the Caspian Sea region and North Atlantic Modes of Variability

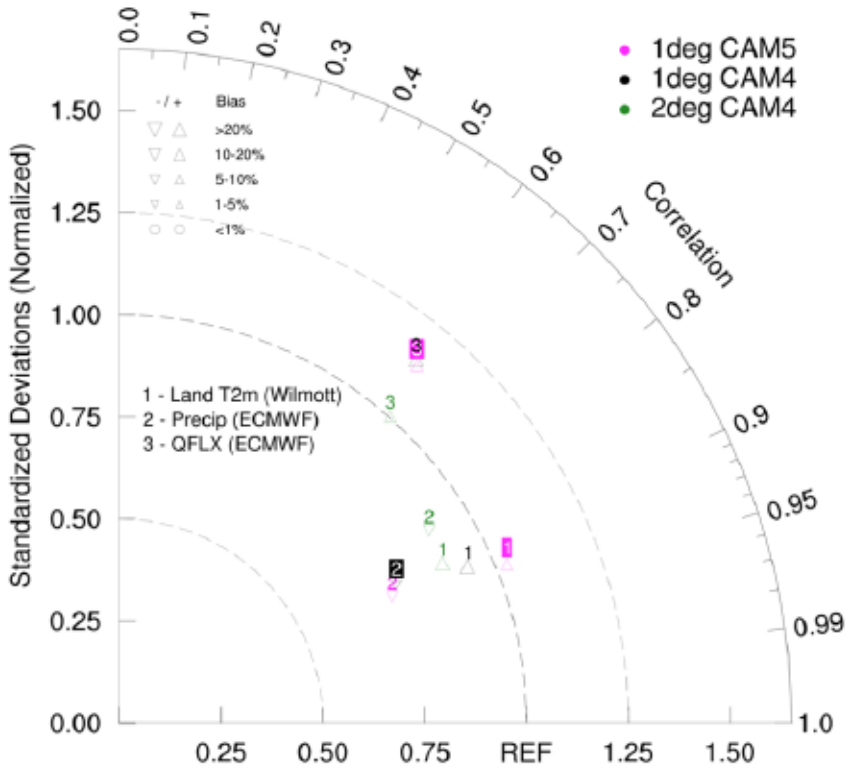

Figure 4.2: Model Skill Metrics. Normalized Taylor diagram for different CESM versions and the referenced data variables (annual means) over the Caspian basin [36-60°N and 45-55°E] (1979-1999). The QFLX here refers to evaporation. The diagram shows CESM-data correlation coefficients (angular axis), CESM standard deviations normalized to observational standard deviations (radius) and biases (Baker and Taylor, 2016; Taylor, 2001).

We evaluate the skills of the different model setups in simulating climatological 2-meter air temperature (T2m), precipitation and evaporation (defined here as the total surface moisture flux into the atmosphere) fields in the CS catchment [36-60°N; 45-55°E] by means of a Taylor diagram (Fig. 4.2), which is a common practice to evaluate multiple aspects of a climate model's performance in a single diagram (Taylor, 2001). To this end, the three historical runs with different model setups (Table 4.1) are evaluated against observational/reanalysis datasets for climatological (1979-1999) annual means. The Taylor diagram reveals that all model setups show lowest skill (low spatial correlation) for evaporation, whereas the models perform better with respect to T2m and precipitation. One reason for the relatively low skill in simulating the evaporation field is related to the land-sea mask of CESM1.2.2, where CSL is set to global sea level and therefore CS surface area is too large especially in the north (Fig. S4.1, S4.2). Since evaporation mainly takes place over the CS, this results in a positive bias in all the model simulations (Fig. 4.2). As a consequence, the water budget of the Caspian catchment basin becomes too negative (Fig. S4.3, S4.4). A negative bias in the simulation of precipitation (Fig. 4.2) further contributes to the negative water budget in all model setups and is partly related to a poor simulation of precipitation in the mountainous regions (Caucasus) west of the CS (Fig. S4.5, S4.6). This orography-related bias is smallest in the 1° model setups. With respect to T2m the 1° CAM5 setup shows the smallest bias over the entire region (Fig. 4.2). A closer inspection reveals that a temperature bias north of the CS of more than 4°C in the 2° CAM4 setup reduces to less than 2°C in the 1° CAM5 setup (Fig. S4.7, S4.8).

Figure 4.3 shows the leading modes of North Atlantic SLP winter variability as simulated by the three model setups and derived from reanalysis data for the period 1950-1999. The results reveal that the simulation with 1° CAM5 shows the best skill when compared to the NAO and EA derived from reanalysis data with respect to the spatial EOF patterns and explained variances, viz 46.4% (15.4%) in the model compared to 42.7% (16%) in the reanalysis data for the NAO (EA). All model setups have severe problems with simulating a SCA-like pattern in the 3rd mode, but the 2° CAM4 setup clearly shows the poorest performance compared to the reanalysis. NAO and EA-like patterns are also simulated by both CAM4 model setups, but the NAO southern centre of action is too weak in the 1° CAM4 while the northern centre of action is shifted eastward in all model setups. The EA pattern is also shifted too far east in all model setups.

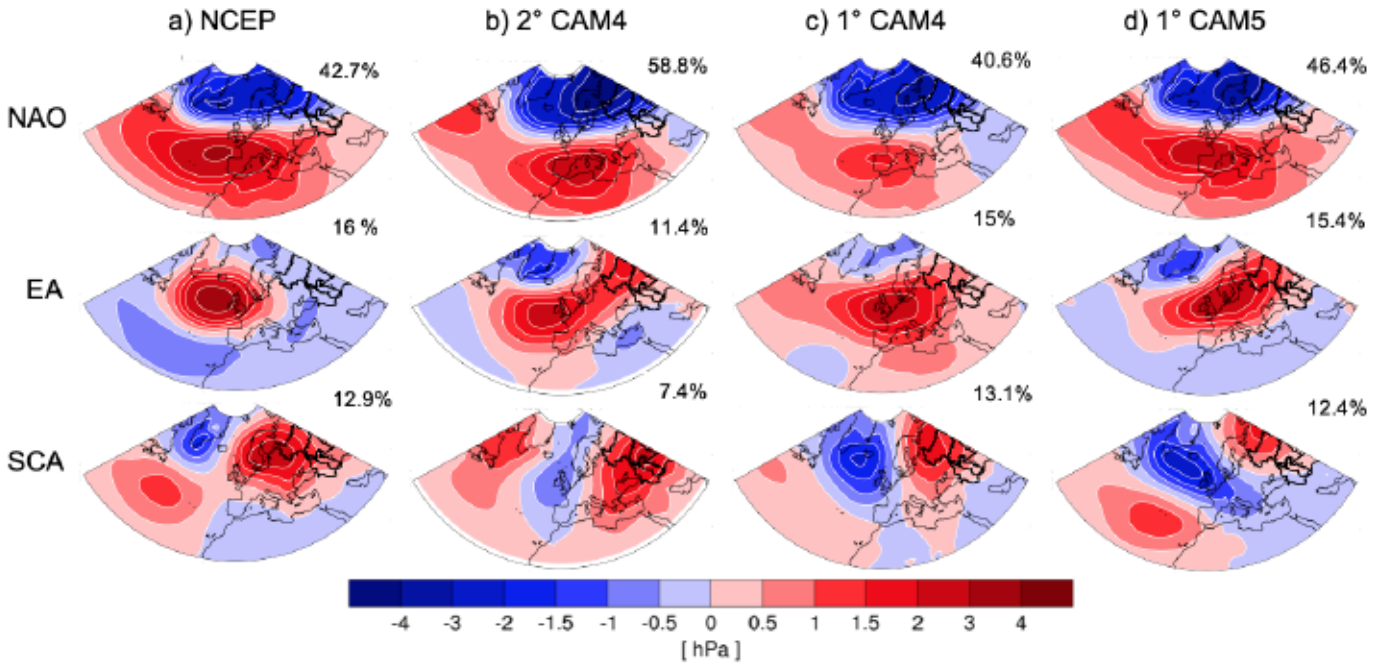

Figure 4.3: Leading three EOFs of winter (DJF) SLP (detrended) calculated for 1950-1999 [70°W-60°E, 20°-80°N] from **(a)** reanalysis data and **(b-d)** different model versions. EOF maps were obtained by regressing the detrended SLP fields onto the standardized principal components. The black outline denotes the Caspian catchment basin.

Taken together, the 1° CAM5 setup shows considerably improved skill in simulating the leading modes of variability compared to the 1° CAM4 and 2° CAM4 setups. It is important to identify the difference between the model setups for future climate change studies. Based on our evaluation, we carried out CESM simulations for future climate with the 1° CAM5 setup. Moreover, we restrict our analyses to the first two modes since the simulation of the SCA pattern is still insufficient with this model setup. Since the position and intensity of teleconnection centres of action are known to affect regional temperature and precipitation, the model biases need to be considered in the assessment of past and future changes in the Caspian region (Hurrell, 1995; Ning & Bradley, 2016; Stoner *et al.*, 2009).

4.3.2 Influence of NAO and EA on Winter Temperature, Precipitation and P-E in the Caspian Catchment Area

In order to analyze the influence of the NAO and EA patterns on the winter (DJF) climate in the Caspian catchment region, we calculate linear regression coefficients with the detrended T2m, precipitation and P-E fields. The regressions are tested for significance against the null hypothesis (i.e. slope =0). Figure 4.4 shows the results for observations and the 1° CAM5 version of CESM1.2.2 for temperature and the period 1950-1999.

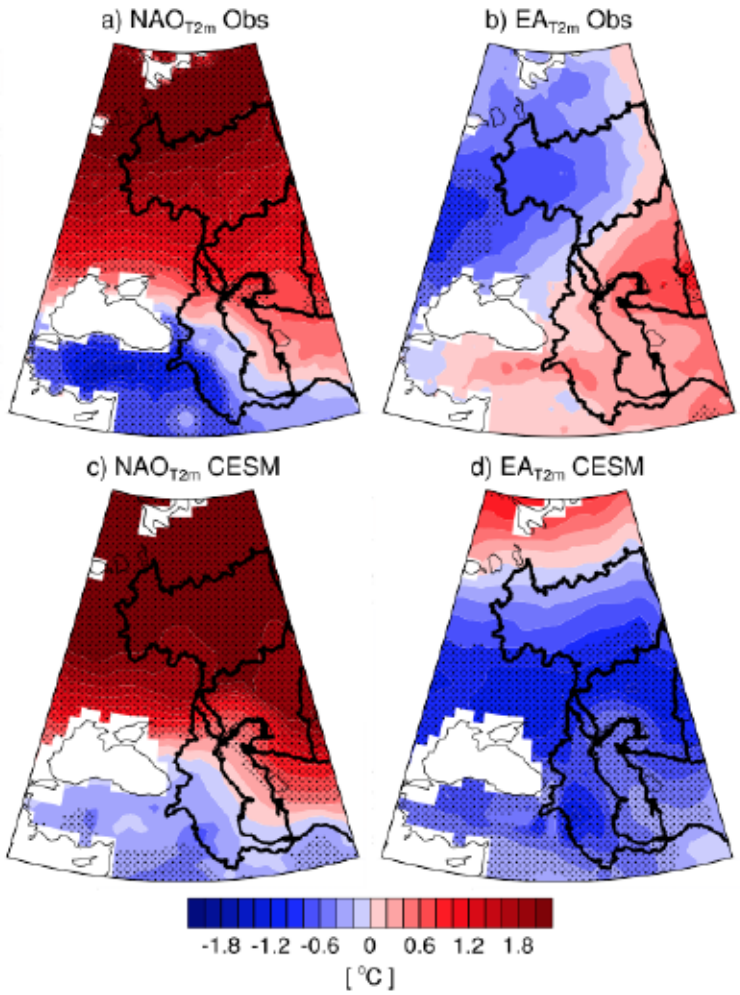

Figure 4.4: NAO and EA influence on T2m. Detrended winter (DJF) near-surface temperature (T2m) regressed onto the two leading standardized principal components of DJF SLP (NAO and EA indices, cf. Fig. 4.3) from **(a-b)** observations/reanalysis and **(c-d)** CESM (1° CAM5) for 1950-1999. Stippling indicates significance at 95% level (applying Student's t-test). The black outline denotes the Caspian basin.

The model captures the observed pattern related to the NAO rather well (Fig. 4.4a, c). In both model and observations, the nodal line crosses the CS and, further to the west, the Black Sea. During the positive NAO phase anomalous warming occurs over the northern part of the Caspian catchment region (including the Volga river basin), while anomalous cooling takes place in the southwestern part. The anomalous warming is mainly controlled by advection of heat by anomalous westerly flow as shown in previous studies (Hurrell & van Loon, 1997; Trigo *et al.*, 2002) and linked to the anomalous SLP pattern over the larger CS area (cf. Fig. 4.3a, d). By contrast, the model fails to reproduce the observed EA-related T2m anomaly pattern, which shows an east-west dipole in the observations (Fig. 4.4b), while strong cooling takes place over the entire CS catchment region during the positive EA phase in the model (Fig. 4d).

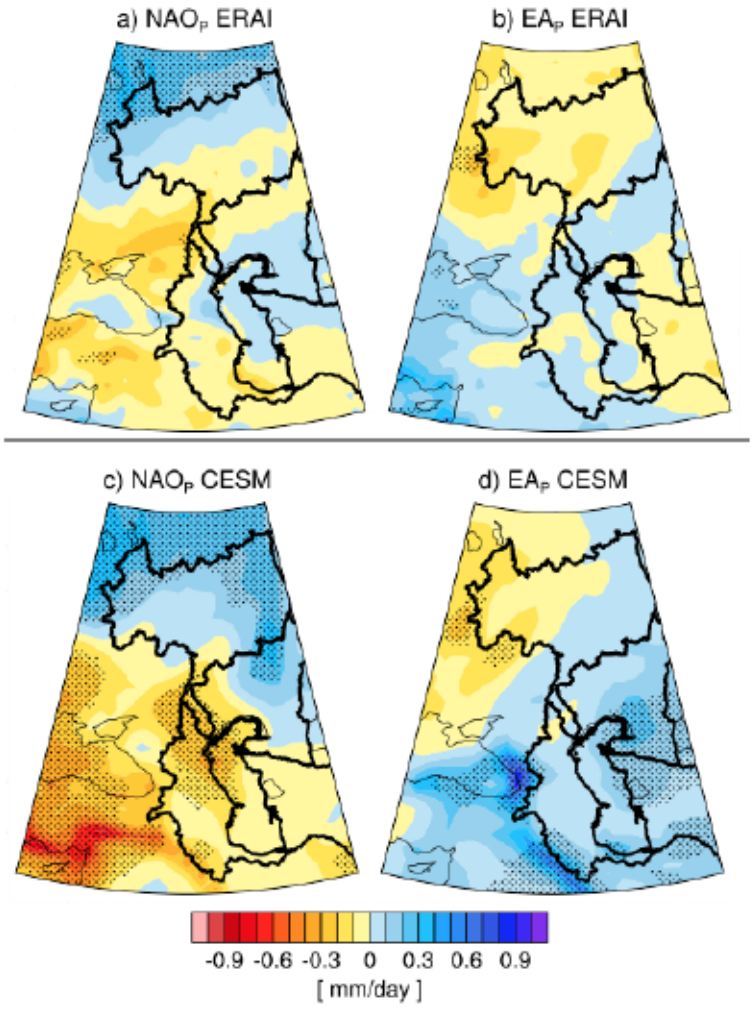

Figure 4.5: NAO and EA impact on precipitation. As Fig. 4.4 but for detrended DJF precipitation and the period 1979-1999.

As to precipitation, both data and model show a strong and large-scale negative anomaly west of the Caspian catchment region (Mediterranean/Black Sea region) and a positive anomaly over the northern Volga basin during the positive NAO phase (Fig. 4.5). It has been shown that NAO-related changes in the mean flow are accompanied by a meridional shift in the storm tracks and associated synoptic eddy activity (Hurrell & van Loon, 1997), which in turn controls precipitation rates (Trigo *et al.*, 2002), thus explaining wetter/drier conditions in the northern/southern regions during positive NAO (Fig. 4.5c). The EA pattern has hardly any significant effect on precipitation over the catchment region in the reanalysis, while the model shows a tendency towards wetter conditions during the positive phase (Fig. 4.5b, d). P-E shows a strong NAO signal over the CS in the reanalysis with a positive anomaly during the positive NAO phase (Fig. 4.6a). A positive anomaly is also simulated by the model, albeit weaker compared to reanalysis over the CS and stronger over the Volga basin (Fig. 4.6c). The EA

shows no clear effect on P-E over the Caspian catchment in the reanalysis data but some wettening in the model during the positive EA phase (Fig. 4.6b, d). In summary, CESM's bias in representing the EA pattern (eastward shift in the centre of action towards the northern CS catchment area; Fig. 4.3d) strongly affects the relationship between the EA and T2m, precipitation and P-E.

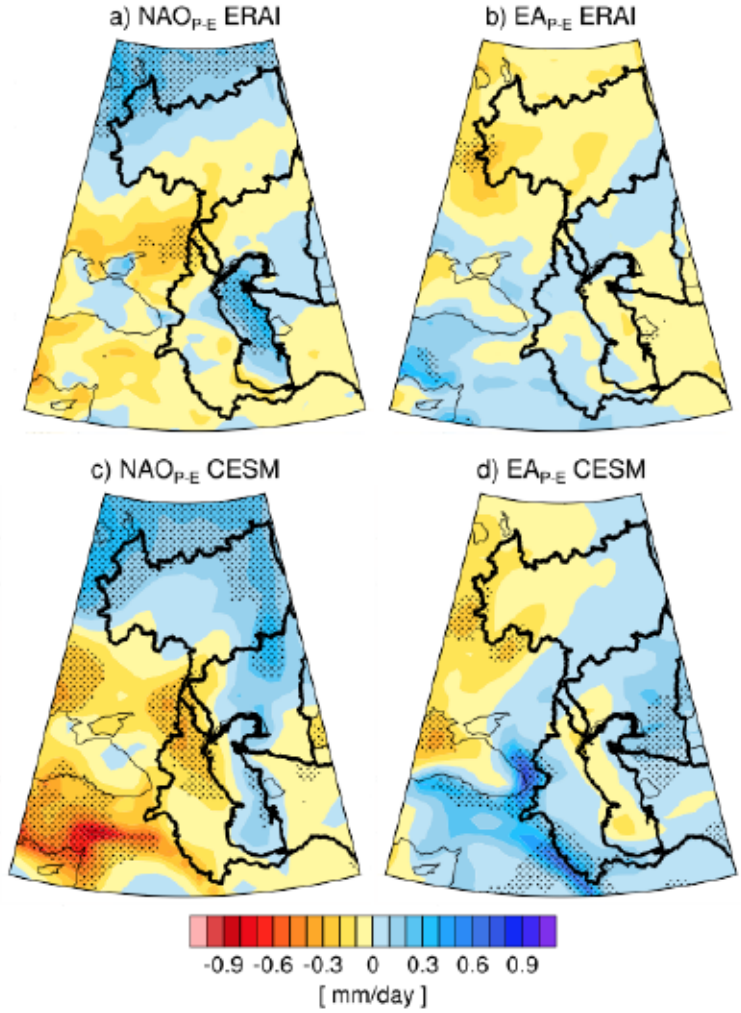

Figure 4.6: NAO and EA impact on P-E. Same as Fig. 4.5, but for P-E.

Due to the generally weak performance of the model in simulating the EA-related T2m and precipitation anomalies in the Caspian region, we will focus our analyses on the NAO for the remainder of this paper. The explained variance for the historical period (1850-2000) as simulated by the 1° CAM5 version is 44.9% for the NAO which exhibits a north-eastward shift of the northern centre of action with respect to reanalysis data (Fig. 4.7). Trend analysis of the corresponding principal component time series showed no significant trend over the historical period.

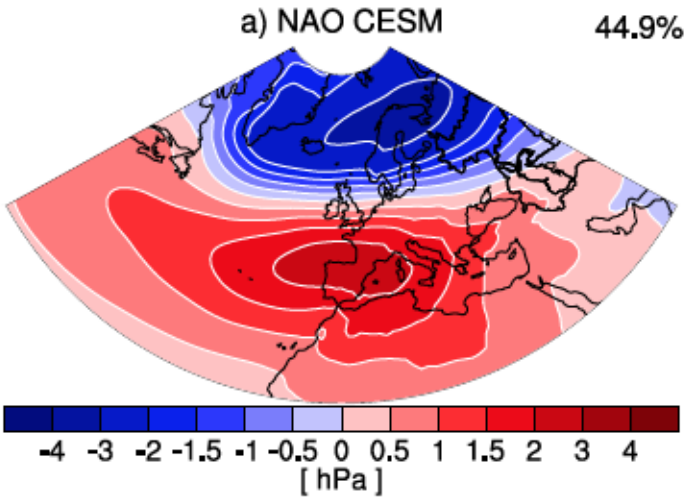

Figure 4.7: CESM CAM5 NAO. Leading mode as in Fig. 4.3 but for the historical period 1850-2000 using CESM with 1° CAM5.

Considering the impact of the NAO over the entire historical period (1850-2000) in order to obtain more reliable statistics, we find that the T2m pattern remains robust (Fig. 4.8a) when compared to the shorter period (Fig. 4.4c). The winter EOF-based NAO index for this period is significantly correlated with the winter T2m averaged over the catchment area ($r=0.7$, $p<0.05$). The winter precipitation shows a much more pronounced and significant large-scale north-south dipole over the longer period than over the shorter late 20th century interval, with more impact on the Caspian catchment area (Fig. 4.8b). This precipitation pattern reflects a northward shift in the storm track and increased moisture transport which is associated with a shift in winter precipitation from southern to northern Europe and the Volga catchment (Hurrell & van Loon, 1997; Hurrell, 1995). This results in a slightly positive correlation between the winter NAO index and winter precipitation averaged over the CS catchment area ($r=0.2$, $p<0.05$). The P-E pattern largely resembles the precipitation pattern (Fig. 4.8c). Anomalous Volga basin precipitation dominates the relationship between NAO and the catchment-integrated water balance, resulting in a weak but statistically significant positive correlation between the winter NAO index and winter P-E integrated over the Caspian catchment area ($r=0.2$, $p<0.05$).

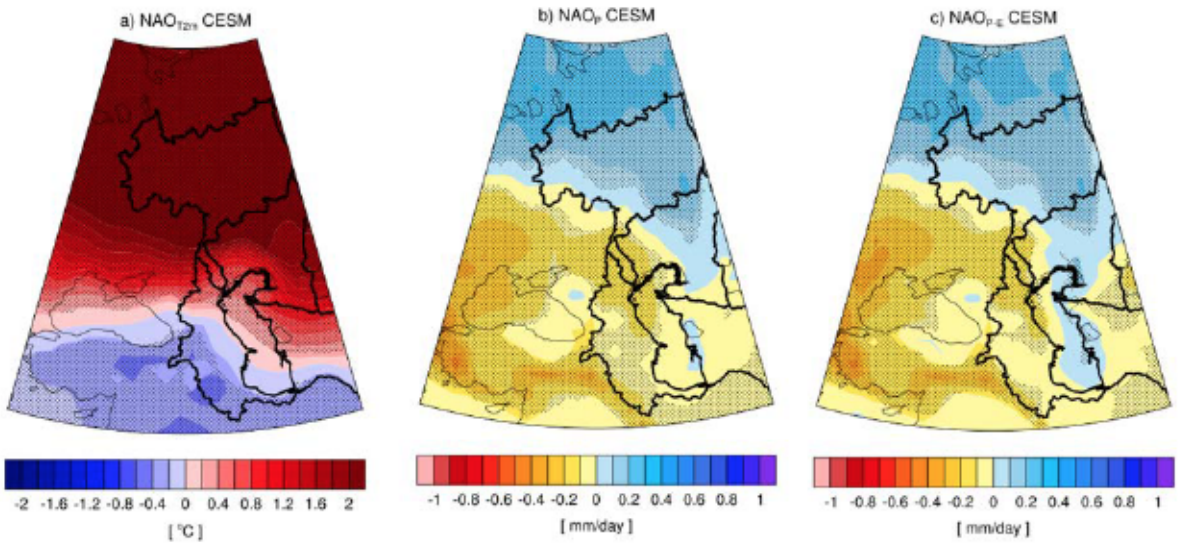

Figure 4.8: CESM NAO for historical period. As Figs. 4.4-4.6 but for the simulated historical period 1850-2000 with CESM with 1° CAM5.

4.3.3 Projected Climatic Changes in the Caspian Catchment Area

Here we examine the projected mean climatological changes first and then investigate the projected changes in the winter NAO signal and its influence on winter Caspian hydroclimate. Regarding projections of the future CS climate evolution, we only consider the 21st century long-term trends based on annual means (2020-2100), since on shorter (e.g. decadal) timescales the transient behaviour of future climate change is influenced by internal climate variability, e.g. the NAO (Deser *et al.*, 2017). Consideration of the long-term trend minimizes the effects of internal climate variability in our analysis. Figure 4.9 shows the linear trends (slopes) in annual mean T2m and hydroclimatic variables as simulated with the 1° CAM5 setup of CESM1.2.2 for the RCP4.5 and RCP8.5 scenarios. In the RCP4.5 scenario the warming is weaker but the pattern has a similar structure (Fig. 4.9a). As expected, the RCP8.5 simulation shows a strong annual warming over the entire region, which is slightly dampened over the water bodies (Caspian Sea, Black Sea) (Fig. 4.9b).

The RCP4.5 shows precipitation increases over the northern and western CS basin, whereas a north-south dipole structure emerges in the RCP8.5 scenario (Fig. 4.9c, d). Evaporation also increases in response to the warming. Strong increase of evaporation over the CS contributes to the damping of surface warming over the lake area.

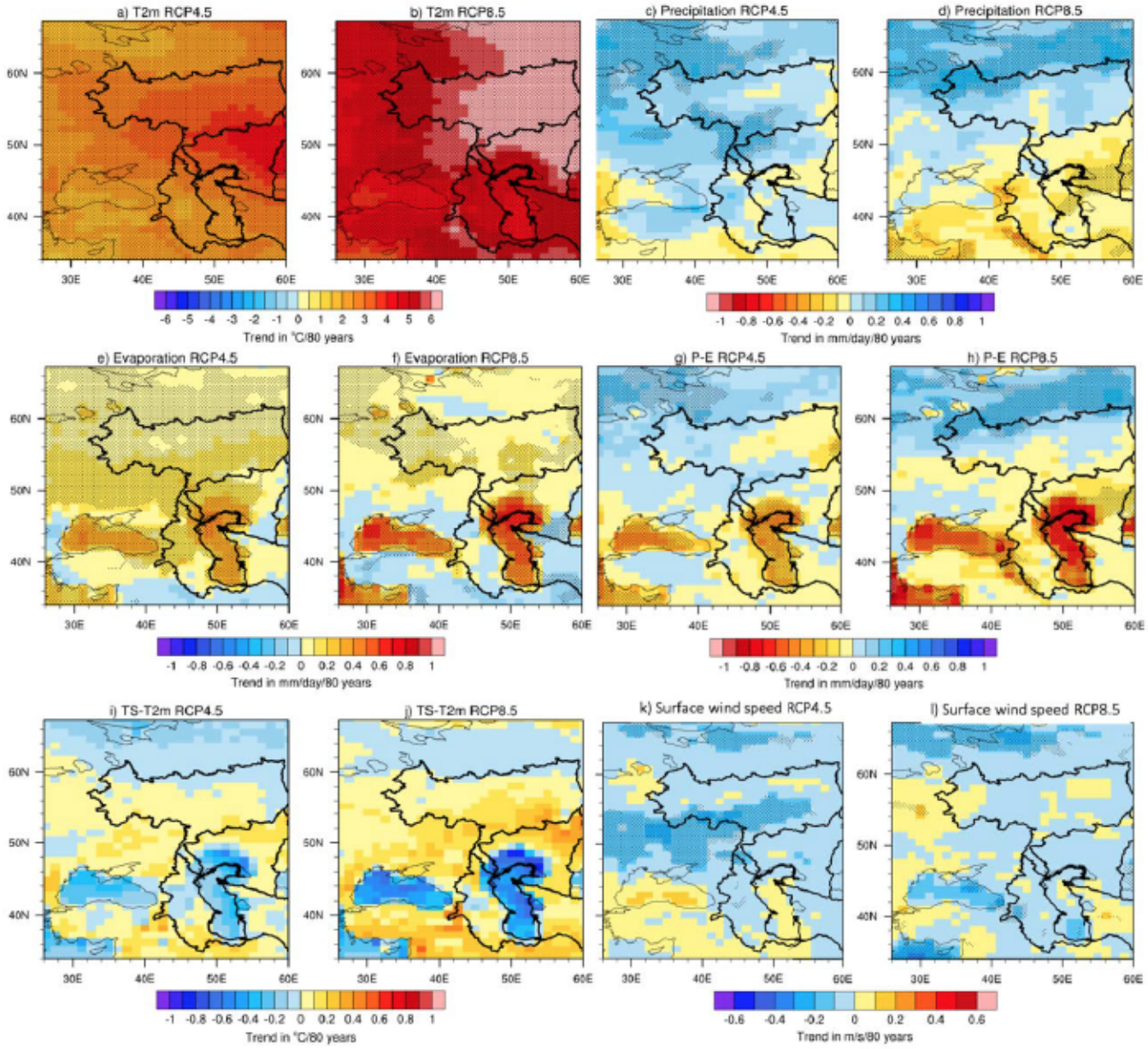

Figure 4.9: Linear trends of annual mean in the RCP4.5 and RCP8.5 scenarios with CESM 1° CAM5 for the period 2020-2100 for **(a-b)** T2m, **(c-d)** precipitation, **(e-f)** evaporation, **(g-h)** P-E, **(i-j)** surface temperature minus 2m air temperature (TS-T2m) and **(k-l)** surface windspeed. Stippling indicates significance at the 95% level (applying Student's t-test).

The increase in evaporation dominates over the precipitation increase such that P-E decreases over the Caspian catchment area in both scenarios (Fig. 4.9e-h). The increase in evaporation over the CS in the RCP8.5 scenario amounts to 15-20% by the end of the 21st century, which is in line with the 16% global lake evaporation increase recently found by Wang *et al.* (2018) under the same emission scenario. Due to evaporative cooling and thermal inertia of water the lake surface warms slower than the air above in both warming scenarios but especially more so for the RCP8.5 (Fig. 4.9i, j) which implies a higher stability of the atmospheric boundary

layer and therefore attenuates increased evaporation. No significant changes in surface wind speed are found over the CS that would contribute to enhanced lake evaporation in the global warming scenarios (Fig. 4.9k, l).

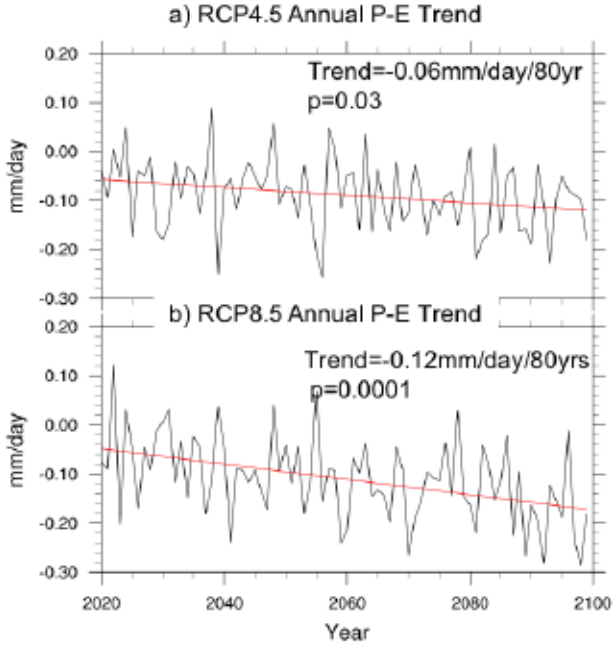

Figure 4.10: Trend analysis of P-E timeseries based on annual means integrated over the CS catchment area over the Caspian Sea catchment area over 80 years (2020-2100) for **(a)** RCP4.5 and **(b)** RCP8.5 as simulated by CESM (1° CAM5).

Table 4.2: Linear trend analysis (in mm/day/80years) with significance (p-values; bold for p<0.05) for P-E time series (2020-2100) integrated over the CS catchment for RCP4.5 and RCP8.5 and the individual seasons.

Seasons	RCP4.5 P-E	RCP8.5 P-E
DJF	Trend= 0.1 (p=0.1)	Trend=0.11 (p=0.08)
MAM	Trend=-0.02 (p=0.6)	**Trend=-0.16 (p=0.02)**
JJA	**Trend=-0.18 (p=0.003)**	**Trend=-0.11 (p=0.02)**
SON	Trend=-0.13 (p=0.07)	**Trend=-0.33 (p=0.0001)**

The timeseries of future annual mean P-E integrated over the CS catchment area shows significantly (p<0.05) decreasing trends (-0.06 mm/day/80years for RCP4.5 and -0.12 mm/day/80years for RCP8.5) (Fig. 4.10). Based on a simple "bathtub" model of the CS, which ignores the bathymetry of the CS as in Elguindi & Giorgi (2006a), and taking a value of 10 for the ratio between CS catchment area and CS surface area, the above negative P-E trends translate into an additional reduction of the CSL by ca. 9 m (RCP4.5) and 18 m (RCP8.5) from 2020 to 2100. Table 4.2 shows the projected P-E trends (2020-2100) based on seasonal means

integrated over the CS catchment for RCP4.5 and RCP8.5. The future P-E is negative for all seasons except the winter, highlighting the dominance of future enhanced evaporation, especially for the summer under the RCP4.5 and the autumn for the RCP8.5.

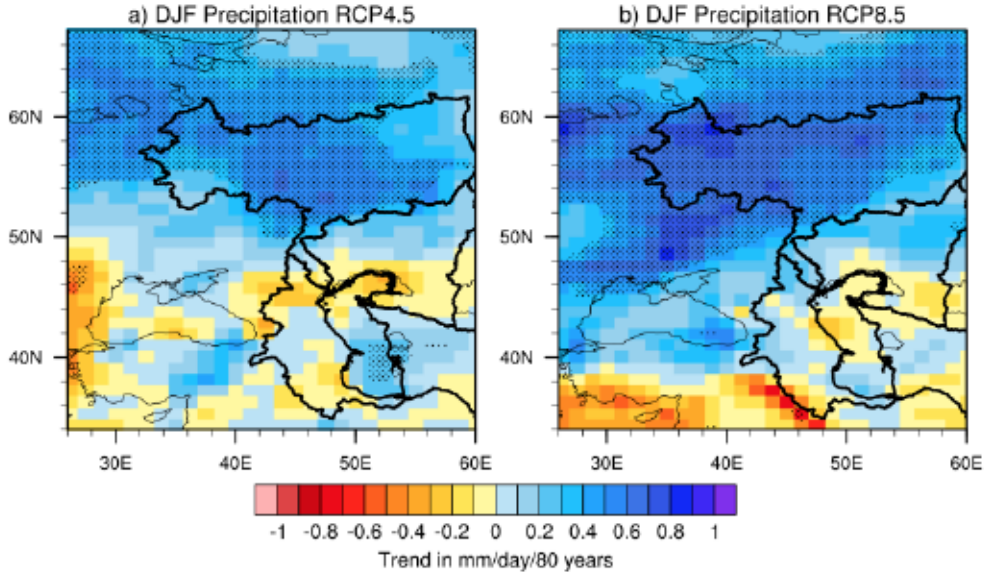

Figure 4.11: Winter precipitation. As Fig. 4.9 c, d but for winter (DJF) seasonal means.

In both scenarios, only in winter a positive trend is found, which can be attributed to an increase in precipitation over the Volga basin (Fig. 4.11) that was also noted in previous studies (Elguindi & Giorgi, 2007). We note that the annual catchment-integrated P-E had no significant long-term trend for the historical period. Increasing evaporation due to warming becomes dominant only in the 21st century, whereas no significant warming of the CS was simulated for the historical period (not shown). By analysing the historical period, Arpe & Leroy (2007) suggested that it is the summer precipitation over the Volga which is key to past CSL variations. However, our linear trend analysis for P-E anomalies suggest that it is the increase in summer (under RCP4.5) and spring and autumn (RCP8.5) evaporation over the CS catchment area that is key to understanding future CSL changes by 2100.

4.3.4 Projected Changes in the NAO Signal and Influence on Winter Caspian Hydroclimate

Of particular interest in this study is the projected winter NAO influence on the CS catchment area. Under RCP4.5 and RCP8.5 we find that NAO remains the leading mode of North Atlantic winter variability but the location and intensity in the centres of action slightly change (Fig. 4.12).

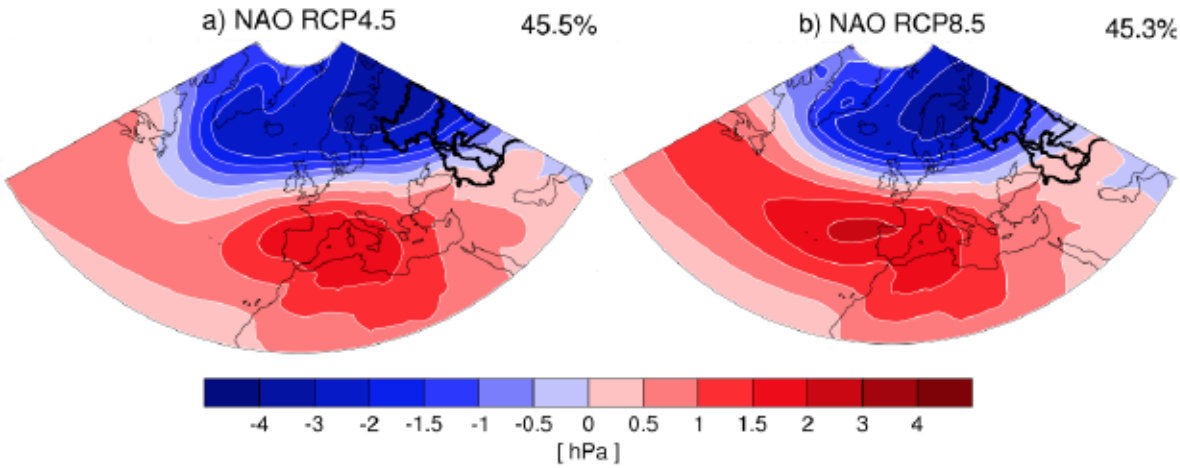

Figure 4.12: The NAO under RCPs. Same as in Fig. 4.7 but for 2020-2100 in **(a)** RCP4.5 and **(b)** RCP8.5

No significant trend is found in the projected NAO index in our simulations. The projected NAO pattern is hard to be distinguished from the present-day NAO pattern given the present-day model biases (Fig. 4.3, 4.7). Under RCP4.5, the only clear difference is that the NAO's northern centre of action is more intensified, extended to the east and has a stronger impact on the entire CS catchment area, while the southern centre of action is weaker, resulting in a southward shift of the nodal line (Fig. 4.7 versus Fig. 4.12a). Compared to the RCP4.5, in the RCP8.5 scenario the model predicts a more (less) intensified southern (northern) centre of action, with a smaller southward displacement of the nodal line over the CS region (Fig. 4.12b). These projected shifts in the nodal lines are likely related to future changes in the large-scale SLP pattern with SLP decrease over the Arctic and increase over the Atlantic and southern European regions (Collins *et al.*, 2013).

Regressing the detrended winter T2m onto the winter NAO index for the period 2020-2100 we find a clear north-south dipole pattern for both RCP4.5 (more southward displaced) and RCP8.5 (less southward displaced over the CS compared to RCP4.5) (Fig. 4.13). Hence, compared to the present/historical situation (Fig. 4.8), the region of positive temperature anomalies during the positive NAO phase extends further south in both scenarios such that almost the entire Caspian basin and Black Sea experience a surface air temperature increase during the positive NAO phase.

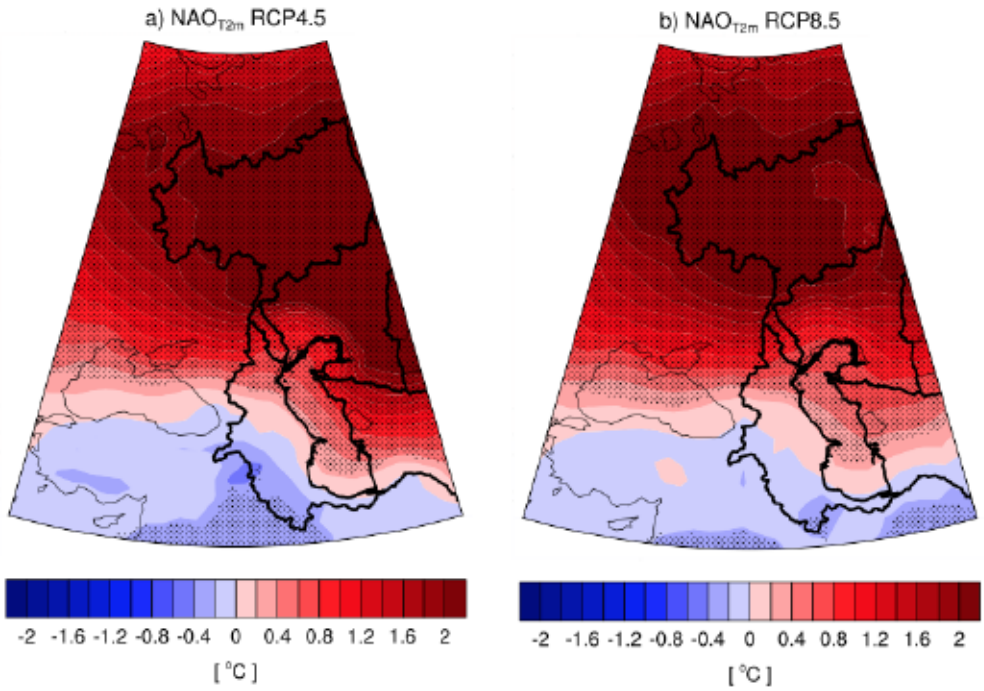

Figure 4.13: NAO influence on T2m under RCPs. As Fig. 4.8a, but for 2020-2100 in **(a)** RCP4.5 and **(b)** RCP8.5.

In both scenarios, T2m for almost the entire Caspian catchment is in phase with NAO since the nodal line shifts southward compared to present. The particularly strong correlation between NAO and CS catchment-averaged T2m under RCP4.5 ($r=0.73$, $p<0.05$) compared to RCP8.5 ($r=0.63$, $p<0.05$) is likely driven by the shift and intensification of the northern center of action.

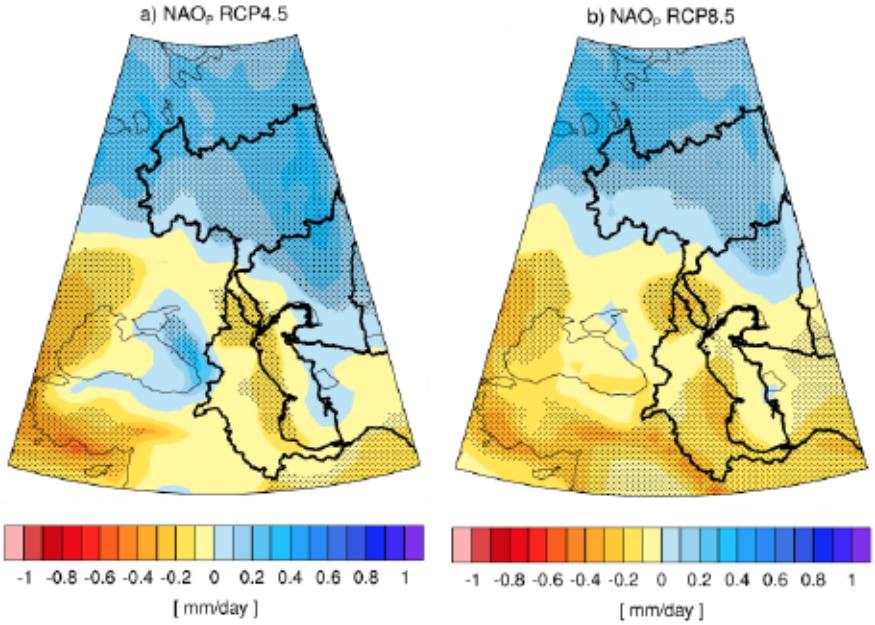

Figure 4.14: NAO influence on precipitation under RCPs. Same as Fig. 4.13, but for precipitation.

Compared to the present situation, the influence of NAO on winter precipitation is projected to increase in the northern part of the Caspian catchment area in RCP4.5 (with a correlation of r=0.5 for the catchment average, p<0.05) (Fig. 4.14a). However, in RCP8.5 NAO's influence on winter precipitation increases over the southern part of the catchment region (Fig. 4.14b) which can partly be attributed to a northward shift of the EOF's nodal line and an intensified southern center of action (Fig. 4.12b) that can be linked to a poleward shift in the storm tracks which is accompanied by a poleward shift in midlatitude precipitation (Chang *et al.*, 2012; Meehl *et al.*, 2007; Yin, 2005). Moreover, a change in the frequency and magnitude of winter blocking events during NAO may also affect precipitation over the southwestern CS (Molavi-Arabshahi *et al.*, 2015).

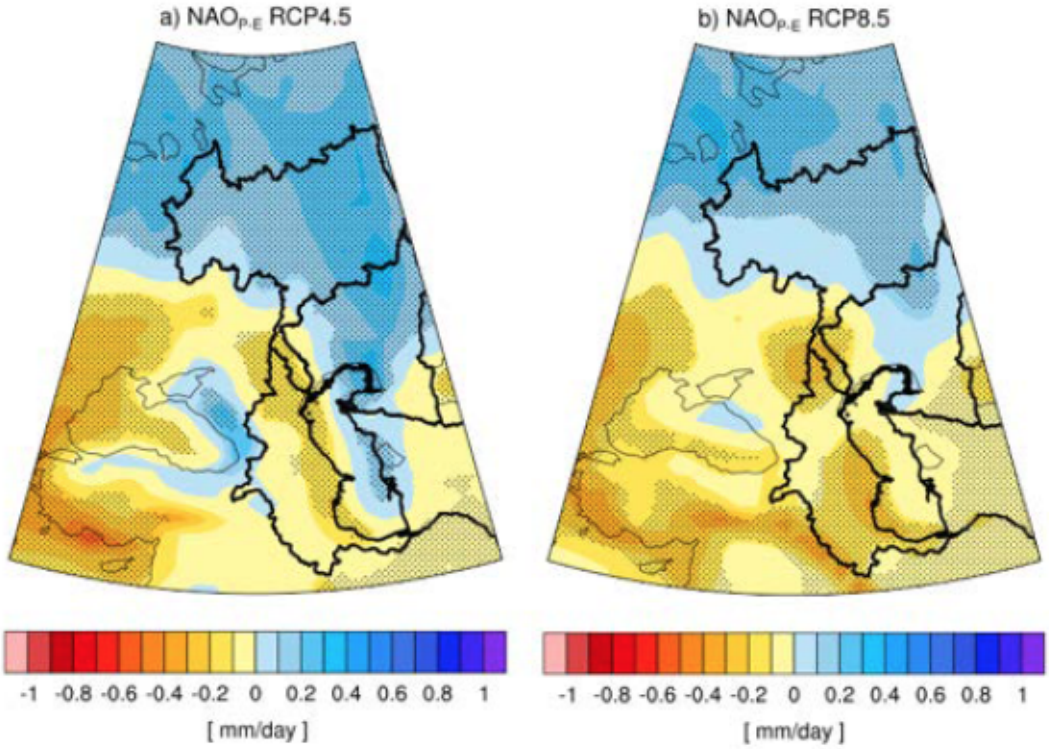

Figure 4.15: NAO influence on P-E under RCPs. Same as Fig. 4.13, but for P-E

As to P-E, a distinct north-south dipole pattern emerges in RCP8.5 (Fig. 4.15) which gives rise to a net cancellation of the effect of winter NAO on P-E variability integrated over the entire Caspian catchment area (i.e. the Caspian water budget) as a positive (negative) P-E anomaly over the Volga basin is nearly compensated by a negative (positive) P-E anomaly over the southern basins. Under the RCP4.5 scenario the correlation between the winter NAO index and winter P-E integrated over the Caspian catchment area (detrended) increases significantly (r=0.5, p<0.05). For RCP8.5, however, this correlation disappears (r=0.05, p=0.6) and the prominent P-E dipole pattern removes the net NAO effect on the Caspian water budget due to

a sub-basin cancellation which is linked to the mechanisms of the NAO-precipitation relationship discussed above. However, in both scenarios the future long-term evolution of catchment-integrated P-E and hence CSL will not be determined by changes in the NAO, but rather by gradually increasing evaporation that will lead to a substantial CSL decline over the 21st century.

4.4 Discussion

The 1° CAM5 setup of CESM1.2.2 simulates the two leading modes of North Atlantic winter variability (NAO, EA) with reasonable skill. However, the CESM teleconnections for the Caspian region are reliable only for the NAO (first mode), and replicate typical see-saw spatial patterns in temperature and precipitation which just reach the CS catchment area. The DJF NAO has a clear influence on the DJF T2m as also seen in other studies (Comas-Bru & McDermott, 2014; Deser *et al.*, 2017; Hurrell & Deser, 2009). Due to the large meridional extension (ca. 30° latitude) and complex orography of the CS catchment area, the NAO affects different parts of the catchment in different ways. A positive NAO reflects enhanced and northward shifted westerly flow bringing warm (and moist) maritime air as far east as the CS region. Associated variations in the precipitation pattern are linked to anomalous atmospheric moisture transport and synoptic activity driven by the NAO as shown previously (Trigo *et al.*, 2002; Panin *et al.*, 2015). While previous studies hypothesized an effect of the NAO on the total Caspian water budget (integrated P-E) and hence CSL (Panin & Dianskii, 2014; Panin *et al.*, 2015), we were able to quantify this correlation for the historical period based on CESM1.2.2 ($r=0.2$, $p<0.05$).

Our results suggest that the relationship between the NAO and the catchment-integrated winter P-E changes depends on the respective background winter climate and the chosen timescale. Under RCP4.5, the projected changes in NAO-driven winter temperature and precipitation signals in the CS region are attributed to an intensified and northeasterly displaced northern center of action along with a weakened southern center of action when compared to the present-day situation, while in the RCP8.5 scenario NAO-related changes are attributed to a comparably more intense and westward shifted southern center of action. Even though there is no general consensus on shifts in the NAO centers of action under changing climate conditions, a similar northeastward shift in the NAO is also seen for some models in other

studies (e.g. Ulbrich & Christoph, 1999; Hu & Wu, 2004) and associated with a change in midlatitude baroclinity and the intensity and position of the Atlantic jet stream and storm track. Previous studies (e.g. Davini & Cagnazzo, 2014; Lee & Black, 2013; Stoner *et al.*, 2009; Ning & Bradley, 2016) also examine model biases in simulating and projecting the spatial NAO structure and associate it to uncertainties related to internal model component variability or dynamics and emission scenarios.

Our simulations suggest an additional CSL decline of ca. 9 m and 18 m by the end of the 21st century for the RCP4.5 and RCP8.5 scenarios, respectively, although this is only a first order estimate, neglecting any other water storage systems (e.g. groundwater) in the Caspian catchment basin, as well as discharge into the Kara-Bogaz bay, the CS bathymetry or tectonic movements (cf. Elguindi & Giorgi, 2006a; Elguindi & Giorgi, 2007). Moreover, these estimates must be taken with care since (i) no dynamic lake model is included in our simulations such that lake-climate feedbacks are not correctly captured, and (ii) the Caspian lake area is too large in the CESM such that evaporation and hence the future CSL decrease are overestimated. The latter effect is of particular importance. Given that the present CS area and associated evaporation is about 10% less than in the model, a corrected CSL calculation with evaporation reduced by 10% yields CSL declines of ca. 9 m and 18 m by the end of the 21st century for the RCP4.5 and RCP8.5 scenarios, respectively, still suggesting that evaporation plays a key role in future CSL evolution. Interestingly, a CSL rise in response to increasing greenhouse gas concentrations by the end of the 21st century was simulated with the coarse-resolution (2.5° horizontal grid resolution) ECHAM4 model (Arpe & Roeckner, 1999). However, this rise was estimated solely from the increase in the Volga river discharge due to increased winter circulation and precipitation. Other studies also find strongly increasing evaporation over the CS in response to increasing air temperatures and suggest CSL reductions by the end of the 21st century of at least 5 m in a regional model (Elguindi & Giorgi, 2007) and about 9 m in a multi-model (global) ensemble mean (Elguindi & Giorgi, 2006a). Taking all these estimates together, it appears highly likely that the CSL will substantially drop due to increased evaporation by the end of the century.

Indeed, Chen *et al.* (2017) recently suggested that increased evaporation over the Caspian Sea is not balanced by river discharge or precipitation, making it the leading driver for changes in CSL. This imbalance is likely to continue unless compensated by discharge or precipitation

increases in the Caspian basin. However, that study did not provide specific estimates of the CSL changes by the end of the 21st century. If the current rate of 7 cm/yr decrease in CSL (Chen *et al.*, 2017) continues, the northern portion of the CS, in which water depths are less than 5 m, may disappear in 75 years . However, due to the strong interdecadal variability of the CSL, such a linear extrapolation should not be based on a decadal trend. Nevertheless, it cannot be ruled out that the shallow northern CS, like the nearby Aral Sea, could face similar catastrophic ecosystem and agricultural impacts (Kosarev, 2005). The middle and south Caspian basins are less likely to face such strong impacts due to greater depths of >800 m (Rodionov, 1994).

As mentioned above, a key caveat in this and other studies is related to the lack of feedbacks associated with a changing lake surface area. For example, a negative feedback where reduced Volga river discharge causes CSL lowering, lake surface area shrinking and hence decreasing evaporation is not modelled by CESM or other climate models. Arpe *et al.* (2018) suggest a formula to estimate this effect for correction. The correct size of the CS in climate models is important for simulating the hydrological cycle. Our simulations also do not consider human-made contributions to the CSL such as dam building and irrigation which may impact the hydrological cycle and the CS size. Further caveats include shortcomings in the simulation of orographic precipitation due to limited model resolution in particular in the Caucasus and Elburz mountain regions as well as the fact of not considering the effects of ENSO, which have been previously investigated in Arpe *et al.* (2000). Our study also highlights the need for evaluating and improving the atmospheric circulation patterns at mid-latitudes in climate models.

4.5 Conclusions

Using the global climate model CESM1.2.2 we analysed the major modes of North Atlantic winter climate variability and atmospheric teleconnection patterns in the Caspian catchment region for the past and future time interval 1850-2100. Our study reveals that CESM1.2.2 with CAM5 atmosphere physics and 1° resolution shows best skill in simulating these modes and teleconnections when compared to the 1° CAM4 or 2° CAM4 setups. Under the RCP4.5 and RCP8.5 scenarios, the EOF-derived NAO remains the leading mode of winter North Atlantic climate variability, however the location and magnitudes of the centres of action change which

affects the regional hydroclimate variability. An increased impact of the NAO on the Caspian region winter climate during the 21st century is seen for the RCP4.5 scenario with enhanced precipitation over the Volga basin during the positive NAO phase due to an intensified and easterly displaced northern centre of action. For RCP8.5 the effect of the NAO on P-E over the southern part of the CS catchment area increases such that a distinct P-E dipole emerges which results in a net cancellation of the NAO effect on the total Caspian water budget. Our results therefore suggest that the correlation between the NAO and the winter conditions over the CS catchment area depends on the changing background climate and on shifts in the location and magnitude of the NAO centres of action.

The most important effect of future warming on the CSL is related to increasing evaporation over the lake surface. Despite increasing precipitation over the northern Volga basin, the increasing evaporation results in a negative water budget and an additional CSL drop of ca. 9 m (RCP4.5) to 18 m (RCP8.5) in our CESM1.2.2 simulations by the end of the 21st century. Although these values may be somewhat overestimated due to a CS area that is too large in the model, they are of the same order of magnitude as the values presented in previous model studies. Such a CSL decline may have a significant impact on the Caspian environment especially over the northern Caspian basin which presently has a depth of less than 5 m. A logical next step is to study the robustness of our results by using multiple global and regional climate models.

Acknowledgements

This project has received funding from the European Union's Horizon 2020 research and innovation programme under the Marie Sklodowska-Curie grant agreement No 642973. All CESM simulations were performed on the supercomputer of the Norddeutscher Verbund für Hoch- und Höchstleistungrechnen (HLRN-III). The processing charges for this open access publication were covered by the University of Bremen. The authors declare no conflict of interests.

5 The role of changing Caspian Sea surface areas on regional climate and large-scale circulation patterns

Sri D. Nandini-weiß [1]*, Sifan A. Koriche[2], Matthias Prange[1], Joy Singarayer[2], Klaus Arpe[3], Hannah Cloke[2], Pepijn Bakker[2,5], Suzanne A. G. Leroy[4], Michael Schulz[2] and Michael Coe[6]

[1] MARUM – Center for Marine Environmental Sciences and Faculty of Geosciences, University of Bremen, Germany.
[2] Department of Meteorology and Centre for Past Climate Change, University of Reading, UK.
[3] Max-Planck-Institute for Meteorology, Hamburg, Germany.
[4] Aix Marseille Univ, CNRS, Minist Culture, LAMPEA, UMR 7269, 5 rue du Château de l'Horloge, 13094 Aix-en-Provence, France.
[5] Faculty of Earth and Life Sciences, Vrije Universiteit Amsterdam, The Netherlands.
[6] Woods Hole Research Center, Falmouth, USA.

Abstract

The Caspian Sea is the largest inland lake in the world, and currently has the highest interannual-decadal variation in surface area of all the large lakes. Despite the clear potential for these variations to impact regional climate, this remains an overlooked element of current global climate model simulations. In this study, the impact of different Caspian Sea (CS) areas on its catchment area and the northern hemisphere are investigated. The CESM1.2.2 coupled climate model is used to simulate the climate of the region with pre-industrial CO_2 and four scenarios of Caspian Sea area: (1) larger-than-present area, (2) current area, (3) small, and (4) no CS scenario. Results reveal strong changes in the regional atmospheric water budget (precipitation and evaporation), whereby evaporation over the sea increases with increasing area, while precipitation increases over SW CS with area increases and vice versa. The presence of CS areas has a large impact on reducing (in summer) and enhancing (in winter) surface air temperatures. We also note enhanced precipitation over central Asia and increased warming over north-western Pacific during winter. Our results further suggest the widening of the 500 hPa troughs with smaller CS area over the northern Pacific and vice versa. Lastly, we show that decreased summer temperatures can trigger the reduction in geopotential height anomalies which results in enhanced north-south dipole pattern and a southward shift in the subtropical jet stream at the 200 hPa and 500 hPa levels during summer. Our findings establish that changing CS areas result in climate impacts of such scope that CS area variation should be considered for incorporation into global climate model simulations, including paleo and future scenarios.

5.1 Introduction

The Caspian Sea (CS) is the world's largest inland sea sited within a vast endorheic catchment area (3.6 Mkm^2) that is fed by 130 rivers (Rodionov, 1994). The present-day Volga river (spans the northern CS basin) contributes ~80% of inflow to the sea level which is ~27 m below sea level (Arpe & Leroy, 2007; Kroonenberg *et al.*, 2008). The CS lies amid semi-arid Central Asian regions, flat arid northern terrains, and humid high mountain ranges in Eurasia (Fig. 5.1). A large region of strong desertification vulnerability lies north of the CS (Republic of Kalmykia) and a region of high precipitation (1000 mm /yr), i.e. the Hyrcanian region, is found south of the CS (Molavi-Arabshahi *et al.*, 2015). Given this complex orography, the entire CS catchment area occupies six Köppen climatic zones (Chen & Chen, 2013) and is known to affect regional and large-scale climate (Arpe *et al.*, 2012).

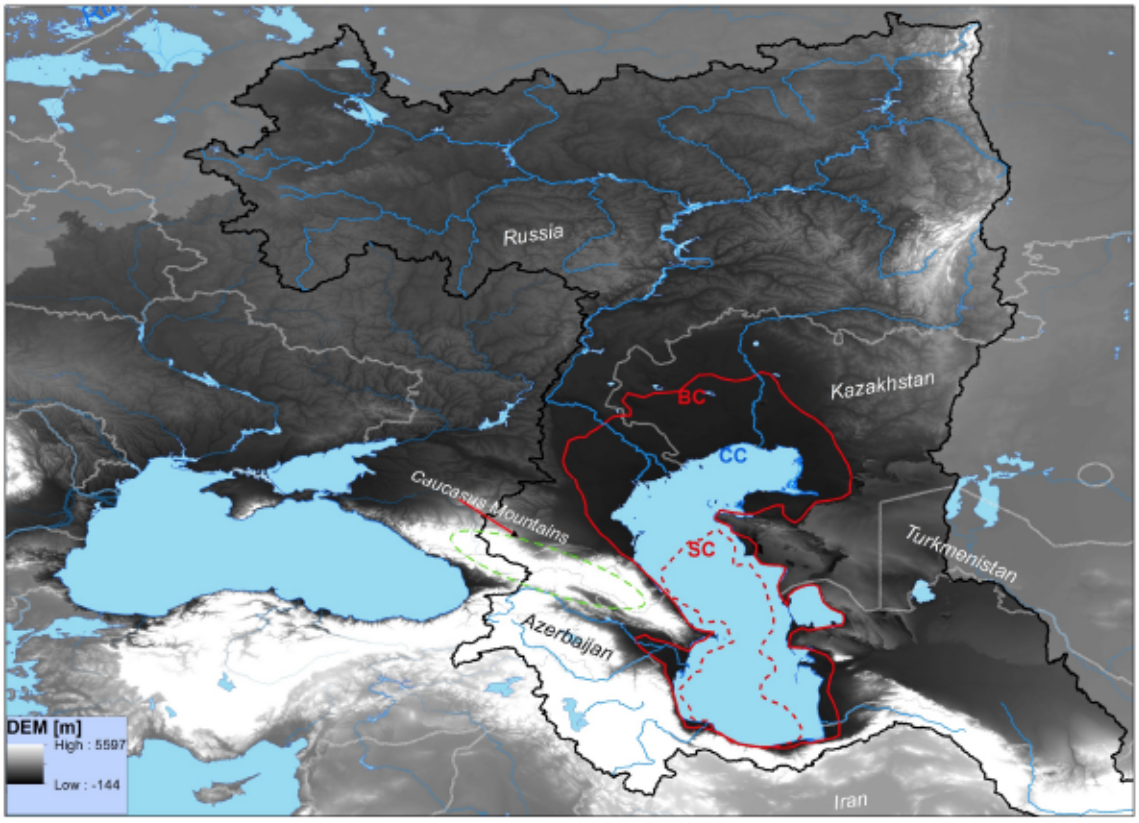

Figure 5.1: Study Area. High resolution DEM contours of Caspian Sea surface areas (shown by red solid line (big Caspian-BC), red broken line (small Caspian-SC) and light blue area (current Caspian-CC)). The catchment area is depicted by black solid line. Blue and grey solid lines represent rivers and country borders respectively. Elevation change is shown by colour shades of white-grey-black.

Over the late Quaternary period, the Caspian Sea Level (CSL) has seesawed drastically by 190 m; ranging from ~50 m higher to ~>90 m lower between glacial and interglacial periods (Fig.

5.1) and >3 m in the last century (Arpe & Leroy, 2007; Arslanov *et al.*, 2016; Forte & Cowgill, 2013; Kakroodi *et al.*, 2014; Naderi *et al.*, 2013). This has led to CS surface area changes ~equivalent to the combined area of the Netherlands and Belgium, which potentially affect regional and large-scale climate. However, it is still not well known on how the CS changing areas (increase/ decrease) affected the regional and northern hemispheric climate in the geological past. Therefore, understanding the feedbacks of changing CS surface areas on the atmosphere is essential at both the regional and global scale, since any large waterbody like CS plays a significant role in affecting the energy and water budget by altering the albedo, evaporative fluxes and near-(surface) temperature.

The potential influence of the presence of a CS on regional and large scale climate, as compared to a 'no-CS' scenario, can be inferred from previous climate modeling studies that examined the impacts on the CS itself (Arpe *et al.*, 2018; Farley-Nichols & Toumi, 2013; Lodh, 2015) and other large lakes, e.g., mega lake Chad (Broström *et al.*, 1998; Coe & Bonan, 1997; Contoux *et al.*, 2013) or the Great Lakes (Lofgren, 1997; Notaro *et al.*, 2013; Sousounis & Fritsch, 1994). The presence of lakes in climate model simulations (compared to simulations in which lakes are absent) is linked, in general, with strong seasonal changes in evaporation, temperature, and precipitation such as the lake effects of increased precipitation and temperature on the CS shown by Farley-Nichols & Toumi (2013). Idealized modeling studies of the Great Lakes have noted that their presence impacts large-scale circulation patterns (geopotential height) and the jet stream (Lofgren, 1997), with increased strength of zonal winds and resulting in enhanced cyclogenesis. This idea is reinforced by Sousounis & Fritsch (1994) who show the Great lakes contribution to the East Coast cyclogenesis via heat and moisture transport. Another study of the effects of the Great lakes on large-scale circulation found that the lakes caused decreased (increased) surface pressure in winter (summer), which led to irregular cyclonicity (anticyclonicity) (Notaro *et al.*, 2013). However, they found no shift in the subtropical jet stream unlike other studies (Lofgren, 1997), due to constraints in regional modeling domain. Moreover, using a regional model, Lodh (2015) established that area changes of the CS impact precipitation over northern India, assumingly from a shift of the subtropical jet stream.

Most climate models still poorly prescribe the actual CS area (related to e.g. low spatial resolution), which results in over /underestimation of its climatic impacts and the introduction of errors in the CS water budget (Arpe *et al.*, 2018; Nandini *et al.*, revised). There are two

notable studies involving investigation of different CS surface areas (Arpe *et al.,* 2018; Farley-Nichols & Toumi, 2013). Using a regional climate model, Farley-Nichols & Toumi, (2013) examined the impacts of the presence of the present-day CS area (when compared to no CS) on seasonal precipitation and large-scale circulation patterns. Their findings suggest that the presence of the CS lead to significant changes in surface temperatures, which increase in winter and decrease in summer. This in turn leads to associated changes in cyclonicity. In particular, decreases in summer temperature are suggested to influence the atmosphere via changes to geopotential height by extending to the top of the troposphere and linked with zonal winds, leading to a stronger summer jet stream over western Asia. However, this study did not investigate other CS areas (larger or smaller areas compared to current area) which are known to occur during late Quaternary period.

Using a global climate model, combined with a full ocean model, Arpe *et al.* (2018) examined the impacts of different CS areas and found that changes in evaporation over the sea are linearly related to CS area. Interestingly, they found that different CS areas have an impact on the large-scale atmospheric circulation as far as the northern Pacific. However, their results can be affected by low resolution (T63), which can limit the actual representation of CS area. Hence, an accurate inclusion of the CS area/shape in climate models of higher spatial resolution is thus important for reliable simulations of the regional climate and surface-atmosphere feedbacks.

The above suggest there is evidence of CS changing surface area on near and far climate systems. Here, we apply a new modeling approach to constrain the impacts from major surface area changes in the CS which are known to occur during the late Quaternary period. Since it is still not fully known what kind of regional and large-scale climate conditions were influenced by the major changes CS surface area, we use our modeling approach to assess whether changes in regional hydroclimate (precipitation minus evaporation) in the catchment area are solely driven by Caspian Sea surface areas. In particular, we aim to identify the impacts from different Caspian Sea surface areas on upper atmospheric circulation patterns (e.g., subtropical jet stream).

5.2 Methodology and Data

We design four scenarios of different CS size (large, small, current and no Caspian) with the

earth system model CESM1.2.2 (Hurrell *et al.,* 2013) to simulate the climate. Next, we examine the anomalies in atmospheric water budget (Precipitation-Evaporation; P-E), surface air temperature and vertically integrated lower level (> 850 hPa) water vapor flux of large, current and small Caspian scenarios with respect to no CS for the regional impact. Vertically integrated water vapor transport (IVT) is calculated by integrating the zonal and meridional moisture fluxes via each atmospheric layer between 1000 hPa and 850 hPa. We repeat this for large-scale changes (subtropical jet stream, geopotential height and sea level pressure. We also perform stand-alone numerical simulation of CSL using climate forcing from the four scenarios using the Hydrological Routing Algorithm model (THMB; (Coe, 1998, 2000)). All statistical analysis on all four simulations include annual mean temporal and spatial as well as polar stereographical seasonal plots of Winter (December, January, February-DJF), Spring (March, April, May-MAM), Summer (June, July, August-JJA) and Autumn (September, October, November-SON). The statistical significance of seasonal and annual mean differences was estimated using a two–tailed Student t-test with 95% confidence level.

Table 5.1: CESM1.2.2 fully coupled model experiments.

Experiments	Resolution	Size (km^2)	Time
No Caspian (NC)	1° (1.25° x 0.9°)	0	1850
Small Caspian (SC)	1° (1.25° x 0.9°)	194019	1850
Current Caspian (CC)	1° (1.25° x 0.9°)	433 926	1850
Big Caspian (BC)	1° (1.25° x 0.9°)	628620	1850

5.2.1 CESM1.2.2 Model Experimental Design

Four numerical sensitivity experiments were carried out at 1° resolution using the Community Earth System Model (CESM1.2.2 CAM5) on the North German Supercomputer HLRN3 for pre-industrial (1850) climate conditions with different CS prescribed areas (Fig. 5.1 and Table 5.1). CESM is a fully coupled global climate model that provides numerical simulations of the Earth's past, present and future (Hurrell *et al.*, 2013). Development of the community model is coordinated by the National Center for Atmospheric Research (NCAR). The coupled components include a physics based atmospheric model (Community Atmosphere Model, CAM5), a land-surface model (Community Land Model, CLM4.0 with carbon-nitrogen (CN) (Lawrence *et al.*, 2011)), an ocean model (Parallel Ocean Program, POP2; (Smith *et al.*, 2010), a sea ice model (Community Sea Ice Model, CISM) and a River Transport Model (RTM

at 0.5°) (Gent *et al.*, 2011). The models are coupled through the CESM1.2.2 flux coupler (CPL7). The atmosphere grid has 26 vertical levels. The CESM1.2.2 ocean and ice models share the same horizontal grid. The horizontal resolution of this grid varies and is higher around Greenland, with the North Pole displaced, as well as around the equator. In all our experiments, we use a nominal 1° resolution of the ocean/sea ice grid. The ocean model grid has 60 levels in the vertical. Evaluation of the model version used in this study (1° version of CESM1.2.2 with CAM5) as well as the role of present and future winter North Atlantic teleconnections on the CS catchment area have been investigated previously in Nandini *et al.* (revised) and found to be the best version of CESM representing the present day CS climate.

5.2.2 CESM Caspian Sea areas and Input Data Preparation

The three CS areas (large, current and small; Fig. 5.1) are determined using a 5 arc minute ETOPO1 digital elevation model (DEM) (Amante, 2009) and using spatial analysis tools in ArcGIS (ESRI, 2016). The DEM is visualized and rasterized with ArcGIS by changing the bathymetry depth of the DEM (0 m, -90 m, -27 m) to create each CS area. The resultant CS areas are overlaid onto the CESM default ocean model domain file to identify and modify the land and ocean grid points. If the water level of a grid point (ocean grid cells) is lower than the mean bathymetry of the grid, the grid is set to be a land grid. The large Caspian simulation is actually the default CESM pre-industrial simulation, that includes a CS area that is larger than the present-day area.

Based on the new CS areas, CESM ocean bathymetry (a 2D field called KMT representing the number of active depth levels at each grid point) are modified to reflect changes made to land/ocean areas. Next, new mapping files are generated with the NCAR Paleo toolkit software to prepare all input files which are interpolated onto the same domain. For all four scenarios, we extrapolate the surface properties of the nearest neighbour grid cell to the new land grid cells (e.g. plant functional types (e.g. grasslands) and soil properties). The land properties were recalculated for each scenario. The initial land surface conditions were interpolated (using Interpinic-a CESM tool) onto the new land surface definition. However, it does not extrapolate CLM initial conditions onto the newly created land grid cells, meaning those are potentially quite far from equilibrium. Lastly, the CESM simulations are spun up for 100 years and the last 50 years are taken for analysis in our sensitivity study. In this study, we examine differences between all simulations with respect to a no Caspian scenario.

5.2.3 The hydrological model: THMB

The CESM model outputs are used as inputs for the hydrological model THMB (formerly known as HYDRA, Hydrological Routing Algorithm) to perform offline simulations of four CSLs, which are spun up for a 1000-year simulation time each. THMB simulates hydrological processes as a linked dynamic system in which locally derived runoff is transported across the land surface in rivers, lakes and wetlands, and is finally transported to the ocean or an inland lake (Coe, 1998, 2000). The model is forced with estimates of runoff over land, and precipitation and evaporation over sea in a hydrologic network linked to a linear reservoir model (Eq. 1). The linear reservoir model (river water reservoir (Wr), surface runoff pool (Ws), and subsurface drainage pool (Wd)) simulates water transport based on prescribed local drainage directions derived from the local topography, residence times of water within a grid cell, and effective flow velocities.

$$\partial[W_r]/\partial t = [W_s/T_s + W_d/T_d] * [1 - A_w] + [P_w - E_w] * A_w - [W_r/T_r] + \sum F_{in}$$

eqn. 01

where A_w is the predicted fractional water area in the grid cell; T_s, T_d, and T_r are the residence times (s) of the water in each of the reservoirs; P_w and E_w are the precipitation and evaporation rates (m^3s^{-1}) over the surface water, respectively; and F_{in} is the water fluxes (m^3s^{-1}) from the upstream cells. For the case of small and no-CS scenarios, where considerable areas were changed to land, we used a simplified Penman-Monteith equation (Allen *et al.*, 1998) to estimate potential evaporation over areas that THMB simulates as water, rather than using the climate modelled actual evaporation (over land points).

5.3 Results

5.3.1 The impact of CS areas on regional climate

Here we present the impacts on surface water budget (evaporation and precipitation), CSL and IVT based on monthly means, and 2 m temperature (T2m). All results presented below are based on monthly climatological model output. Our results show that changes in the CS area exert strong impacts on the water budget (Fig. 5.2). Evaporation increases as CS surface area increases in all seasons, with spring being the lowest and autumn the highest except for the NC where evaporation is highest in spring (Fig. 5.2a) because highest precipitation occurs in winter (Fig. 5.2c), when there would be enough water in the ground, which can be evaporated. The

mean annual precipitation increases with a larger CS area with up to a 73% over CS and 21% over CS basin with respect to no-CS scenario (Fig. 5.2c). The mean annual evaporation increases with a larger CS area with up to a 398% over CS and 51% over CS basin with respect to no-CS scenario (Fig. 5.2b). This is directly linked to the increase in surface area of the CS. The annual mean evaporation anomaly over the CS is predominantly higher (more than 3 mm day^{-1}) (Fig. 5.3a, e, i).

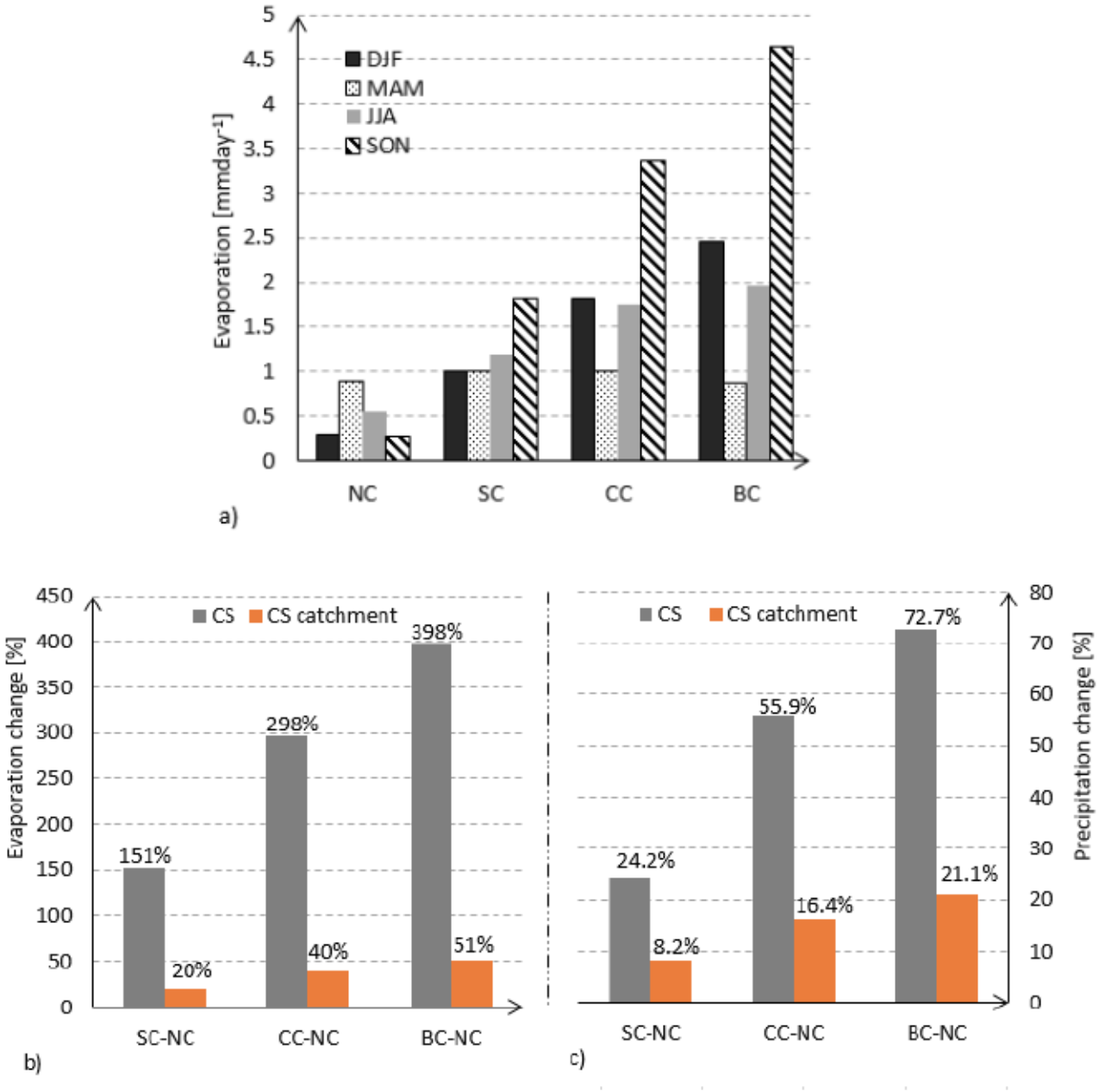

Figure 5.2: Seasonal changes for evaporation and precipitation a) Mean seasonal evaporation, b) percentage change of evaporation relative to no-CS scenario over larger CS (in grey) and CS catchment (in orange), and c) same as b) but for precipitation.

The changes in CS area likely controls the precipitation distribution and amount (Fig. 5.3b, f,

j), since larger surface area means more water available for evaporation and this leads to more moisture in the atmosphere available for precipitation. The largest precipitation anomalies (greater than 1 mm day^{-1}) occur over the south-western (SW) part of CS.

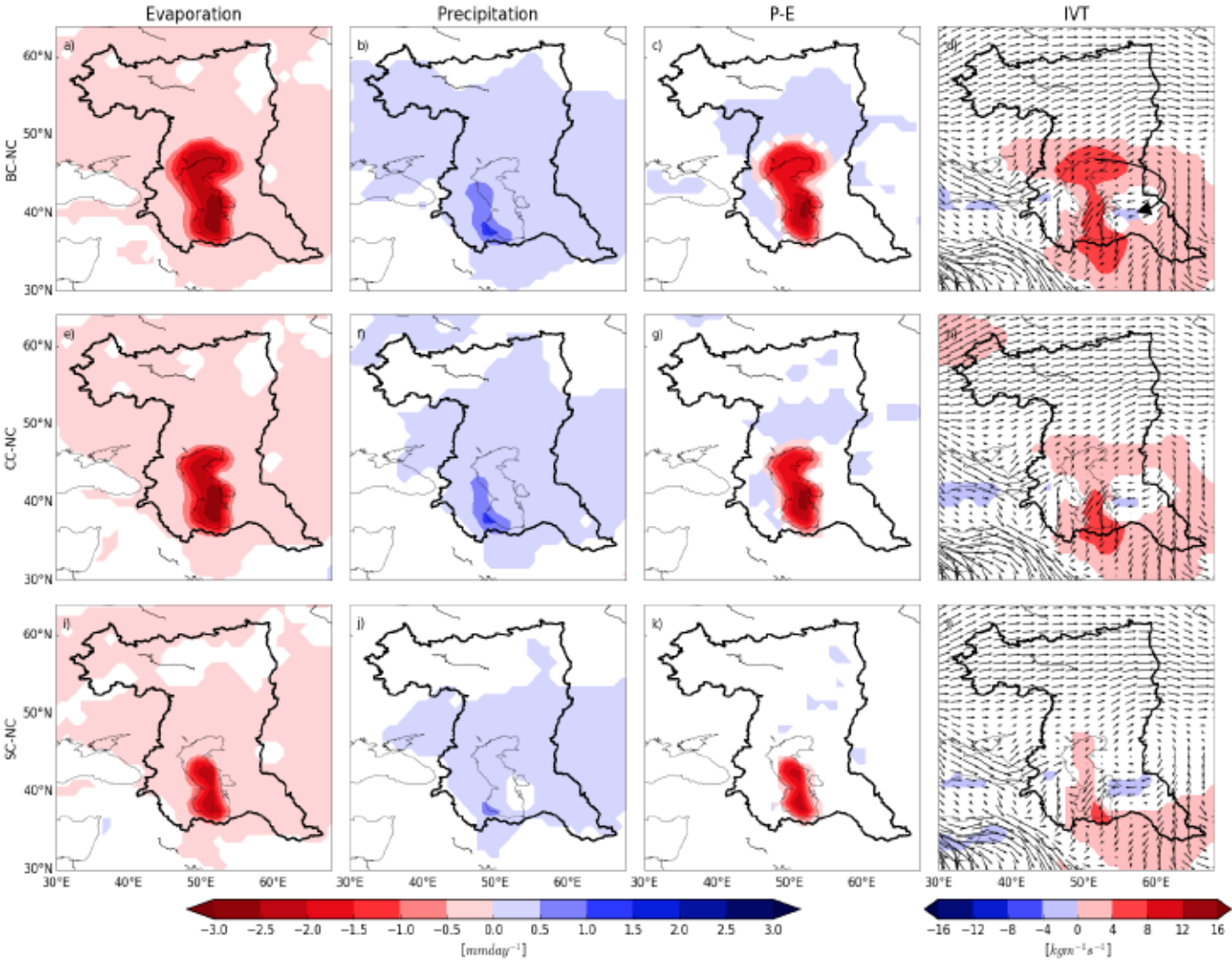

Figure 5.3: Annual mean changes for evaporation (a, e and i), precipitation (b, f and j), P-E (c, g and k) and lower level (1000 – 850 hPa) vertically integrated water vapor transport (IVT) (d, h and l) for large, current and small CS with respect to No-CS scenario. Shading indicates significance at 95% level (applying Student's t-test). The IVT is calculated by integrating the zonal and meridional moisture fluxes. The vector field are not anomaly values, but actual values of IVT for BC (d), CC (h) and SC (l).

The two possible primary reasons for higher precipitation in the SW are the amount of evaporation available over the sea (which depends on the size of the sea) and lower level easterly winds driving vapor flux toward a SW direction (Fig. 5.3d, h, l) enhanced by the Caucasus and Elburz mountains (Arpe et al. 2018). Significant, though smaller, changes in the annual mean precipitation (<0.5 mm day^{-1}) are observed over most parts of CS catchment area,

which can be linked to the combined effect of lower level easterly wind driving the moisture flux and the large-scale circulation processes influenced by upper level westerly winds. To understand the drivers of moisture transport that contribute to changes in water balance, we investigate lower level IVT (>850 hPa level). The amount of available moisture flux increases with larger CS area (Fig. 5.3d, h, l). Lower level wind patterns over CS and the eastern part of CS basin form a circular pattern and this plays vital role for transporting moisture flux generated over CS and also from the eastern part of the sea (Fig. 5.3d). In particular, this easterly surface winds (from Kazakhstan) shift direction to the south-west around the western CS catchment area and this contributes significantly to the moisture flux directed towards the south-western parts of CS.

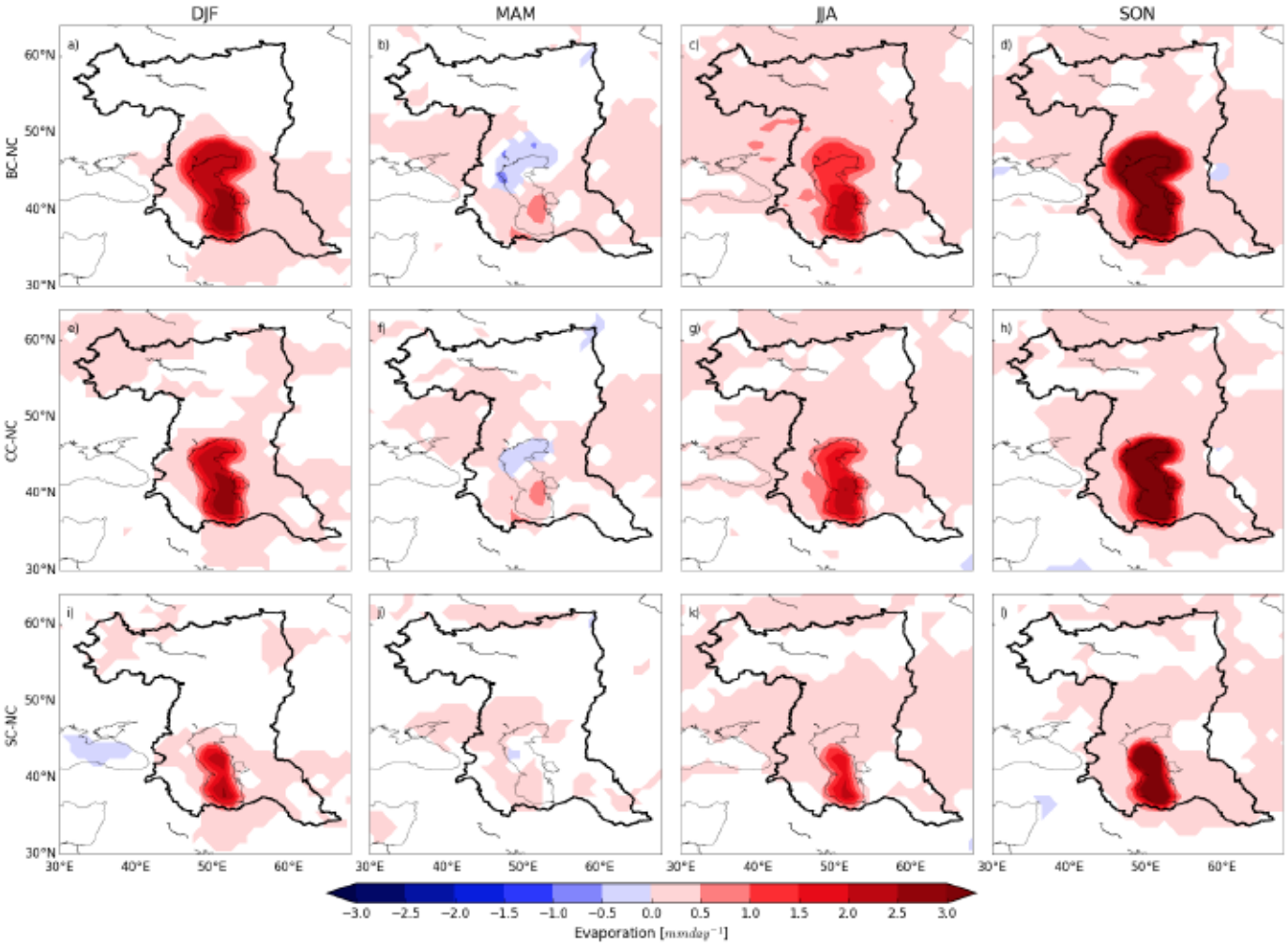

Figure 5.4: Seasonal mean evaporation changes of large, current and small CS with respect to No-CS scenario. The shaded colours show statistically significant changes with 95% confidence interval.

Higher evaporation over the CS mainly happens during the autumn (followed by winter) season (Fig. 5.4). This is because of greater thermal inertia (higher heat capacity plus lower albedo

compared to bare surface), and more heat is stored during spring and summer leading to lower evaporation and released later during autumn and winter leading to higher evaporation. Due to an accumulated cooling effect during winter and spring periods (resulting in sea ice cover during spring time) the northern shallow CS part experiences lower evaporation (Fig. 5.4b, f).

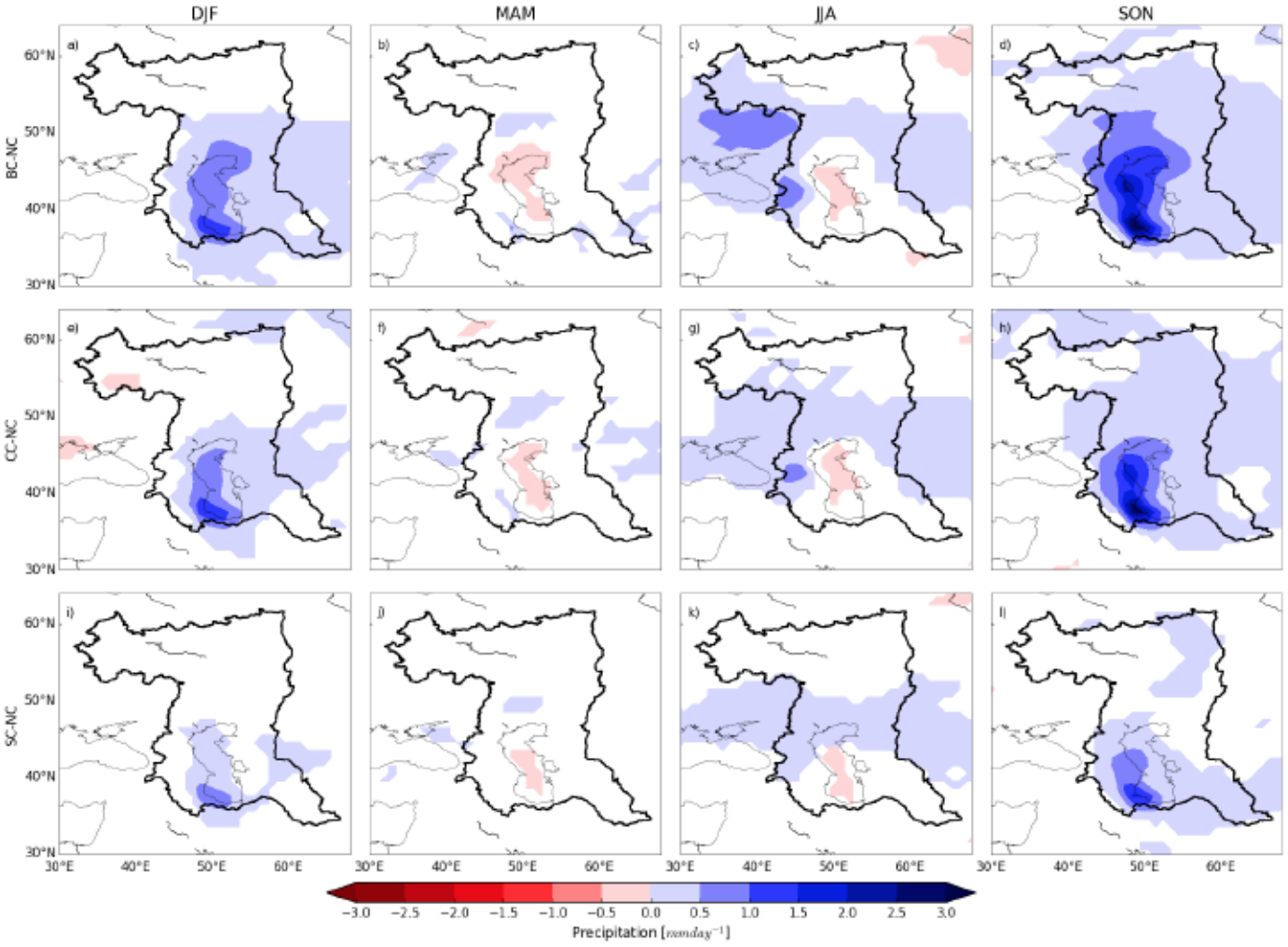

Figure 5.5: Same as Fig. 5.4 but for precipitation changes.

Seasonal changes of precipitation have a similar spatial pattern to changes in evaporation during autumn and winter (Fig. 5.5). The presence of CS produces more precipitation over the sea in autumn and winter (more than 2 mm day^{-1}), but less precipitation over sea in spring and summer (Fig. 5.5). This suggests that winter and autumn precipitation changes dominate the annual mean anomalies which can be related to changes in air temperature. Although changes in precipitation tend to follow evaporation occurrence during autumn and winter, the changes are not linearly related throughout the year.

The surface temperature changes are linear (Fig. 5.6), with the larger CS area produced higher

(lower) in T2m during autumn and winter (spring and summer) (Fig. 5.6) which agree with the results of Farley-Nichols & Toumi (2013), and further suggest the link between changes in CS area and air temperature changes over the CS and surrounding area.

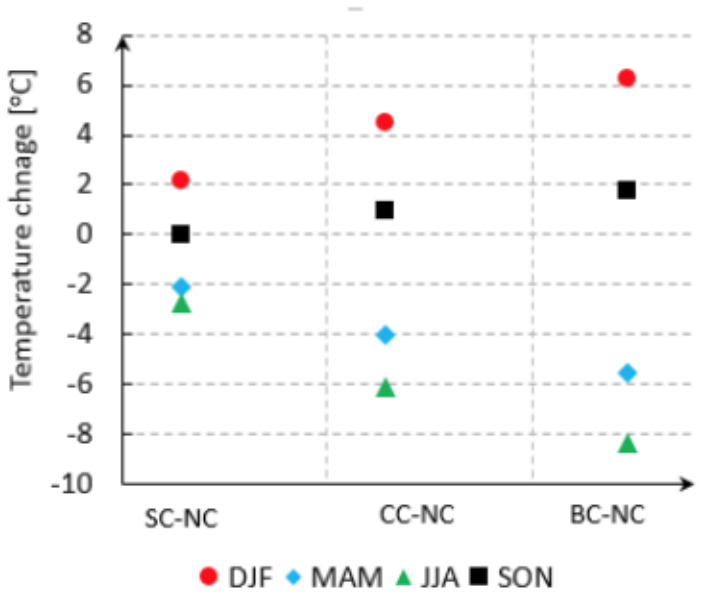

Figure 5.6: Mean seasonal temperature (T2m) changes with respect to no Caspian scenario over CS surface areas.

Seasonal variation of T2m for larger CS clearly show significant decrease over and around the CS, predominately during spring and summer time (Fig. S5.2), although the amount of solar radiation received during this time is higher compared to other seasons. This can be explained by the albedo and heat capacity effect. A No-CS scenario results in a greater area of bare land surface with a higher surface albedo than over sea, and because of higher thermal inertial (higher heat capacity) of the sea, air temperature over the sea remains cooler during the summer season.

5.3.2 The presence of CS areas on large-scale climate

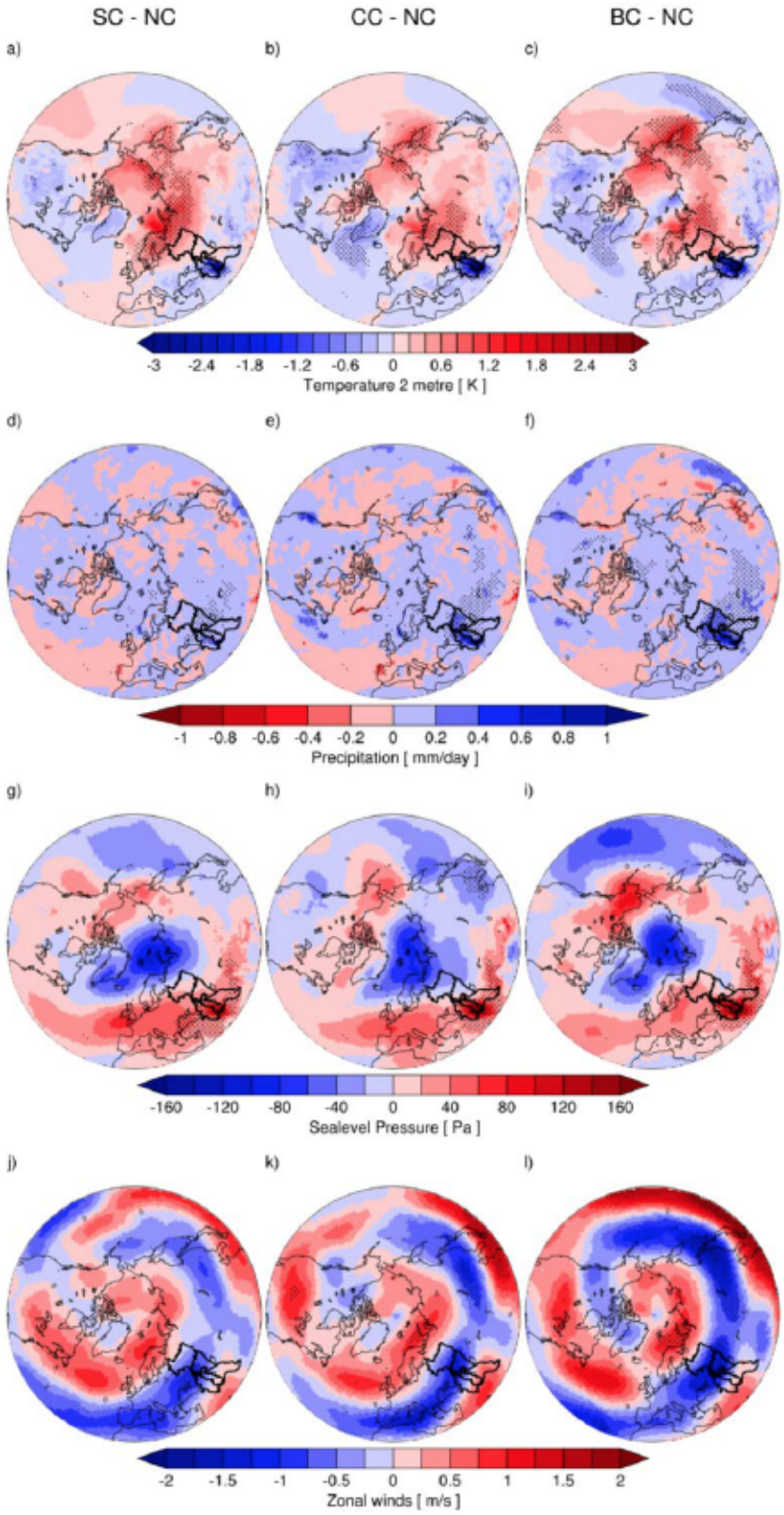

Figure 5.7: Annual mean changes for small Caspian, Current Caspian and Big Caspian compared with no-Caspian scenarios for (a-c) temperature 2-meter, (d-f) precipitation, (g-i) sea level pressure and (j-l) zonal wind at 200hPa showing the location of the jet stream. Stippling indicates significance at 95% level (applying Student's t-test).

Annual changes show significant warming (>1 K) in surface air temperatures extending in a north-easterly band over the northern catchment area and as far as east Siberia and northwest Pacific. The warming over the northwest Pacific decreases in the small CS scenario when compared with the no Caspian scenario (Fig. 5.7a-c). Also, it appears that temperatures are restricted in the southern CS by the Elburz mountains, which was previously noted by Farley-Nichols & Toumi (2013) and Arpe *et al*. (2018). These temperature changes are stronger when compared with precipitation, where annual mean changes appear more restricted to regional NW surroundings of CS catchment area at ~0.8 mm/day (Fig. 5.7d-f). Upon examining the large-scale changes in sea-level pressure due to the presence of each CS area, high pressures are seen extending from the Mediterranean region towards the southern CS (at ~ 125 Pa), which increases with small CS when compared with larger CS area (Fig. 5.7g-i). We also note high pressure over the northwest Pacific that decreases due to the presence of large to small CS area (Fig. 5.7g). The zonal winds at the 200 hPa level show the location of the subtropical jet stream that plays a key role in distributing moisture, temperature, and pressure across this region (Fig. 5.7j-l). We denote north-south dipole changes in the jet stream pattern driven by the westerlies with a decrease in speed over the northern CS catchment area, which extends in a north-easterly band across Asia and northwest Pacific concerning small to large CS area. The increase in the jet stream speed slows down over the southern CS catchment area, in the small CS area (Fig. 5.7j).

In order to understand the influence from different CS areas on the upper atmospheric flow, we also investigated annual changes for geopotential height and temperature at the 500 hPa level (Fig. 5.8). Results show that annual mean temperatures trigger corresponding changes in geopotential height, possibly via atmospheric Rossby waves (Hoskins, 1981). This can result in the widening of the 500 hPa troughs over the northern Pacific under the presence of large CS area (Fig. 5.8f). Hence, a significant upper atmospheric link occurs between decreases in temperature and the reduction in geopotential height over the southern CS catchment area and vice versa.

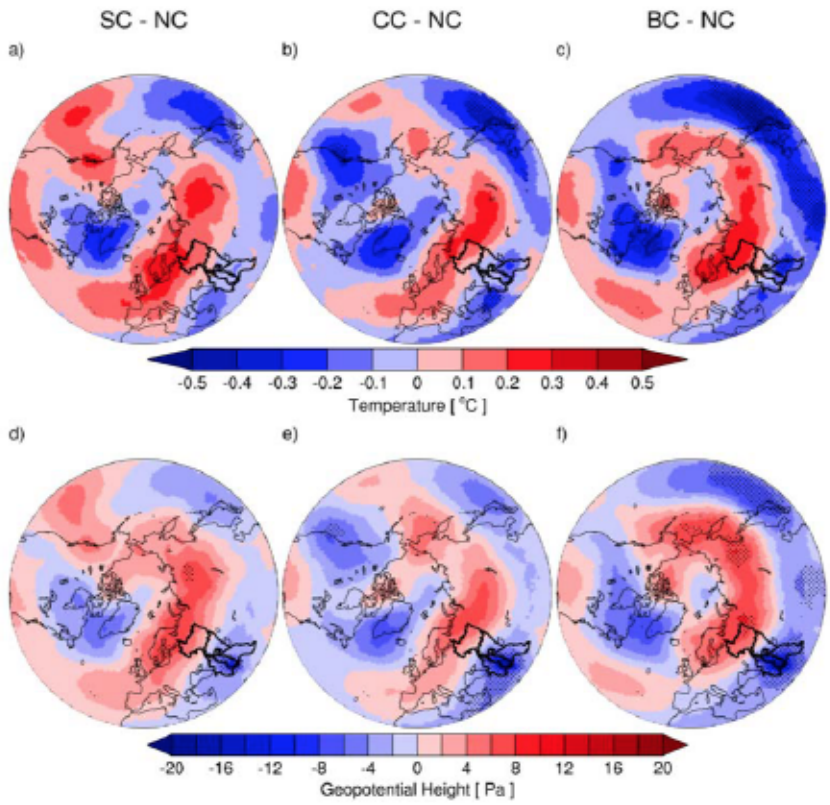

Figure 5.8: Same as Figure 5.7 but for (a-c) temperature and (d-f) geopotential height at the 500 hPa level.

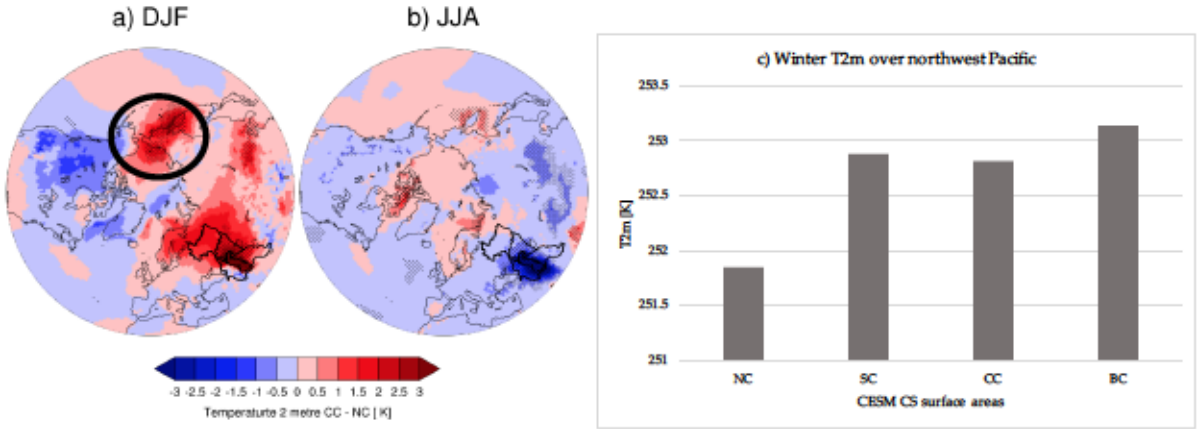

Figure 5.9: a) Winter and b) summer changes for temperature for current CS- no CS scenario and c) CESM CS surface area changes for winter temperature, averaged over Northwest Pacific region [45:80N and 140:185E] (circled in black).

The seasonal results also suggest that different CS areas influence large-scale climate over the entire northern hemisphere. Here, we only consider winter and summer changes and take the current CS scenario (compared to no CS) as an example. The most striking and significant seasonal feature is the intense warming during winter for air temperatures over the CS and the northern catchment area, which extends as far afield as the northwest Pacific (Fig. 5.9a). In

comparison, the summer reduction in temperatures are restricted over the CS catchment area (Fig. 5.9b). The enhanced winter temperature seen in Fig. 5.9a over the northwest Pacific region [45:80N and 140:185E] are averaged for all CS scenarios (Fig. 5.9c).

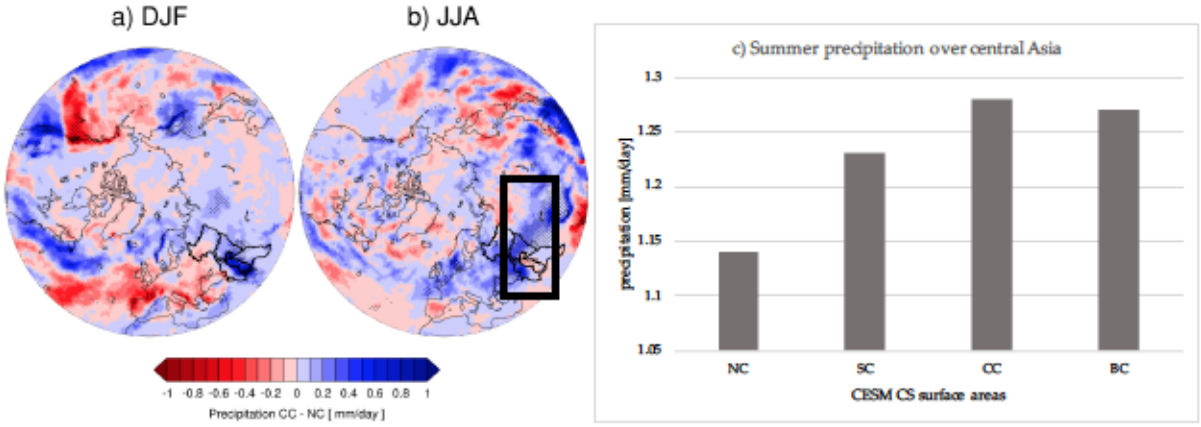

Figure 5.10: a) Winter and b) summer changes for precipitation for current CS- no CS scenario and c) CESM CS surface area changes for summer precipitation averaged over central Asia region [35:55N and 55:100E] (rectangle in black).

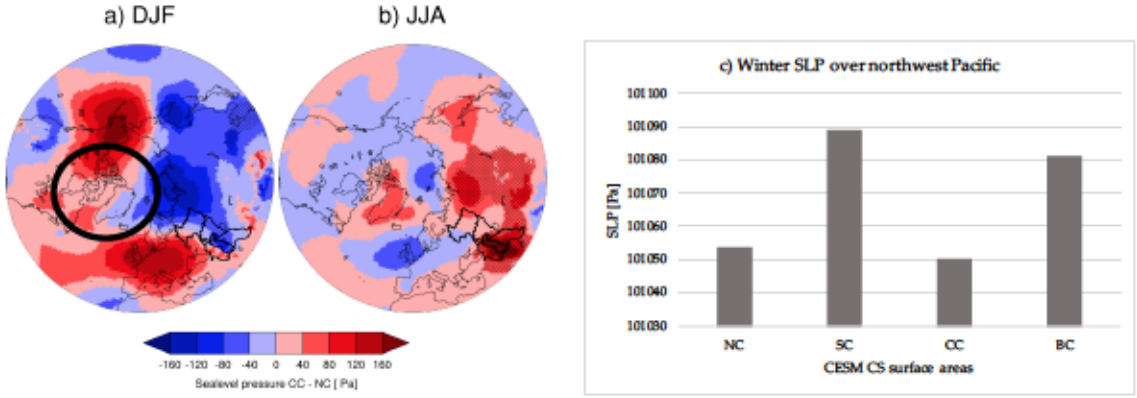

Figure 5.11: a) Winter and b) summer changes for sea level pressure for current CS- no CS scenario and c) CESM CS surface area changes for winter sea level pressure averaged over Northwest Pacific region [45:80N and 140:185E] (circled in black).

Generally, the warming increases from a no CS to large CS area. On the other hand, the winter increase in precipitation are mostly restricted over the CS (Fig. 5.10a). However, the summer increases over central Asia are of valid interest (>0.6 mm day^{-1}) (Fig. 5.10b). When examined over the central Asia region [35:55N and 55:100E], precipitation seems to broadly increase for all simulations (Fig. 5.10c). This increase in summer precipitation over central Asia can be driven by the associated changes seen previously in surface winds, moisture flux and the lake effects of the CS which transports moisture afield. However, this merits further investigation. The winter sea-level pressure changes show an east-west pressure dipole over the CS catchment area, and high pressure over the northwest Pacific and Europe (Fig. 5.11a).

However, during summer, high pressures are seen over the sea, southern catchment area and central Asia region (~160 Pa) (Fig. 5.11b). To investigate the high pressure over the northwest Pacific during winter, we averaged this region [45:80N and 140:185E] and suggest the presence of the small CS area to influence the enhanced pressure gradient; when compared to a larger or current CS area (Fig. 5.11c).

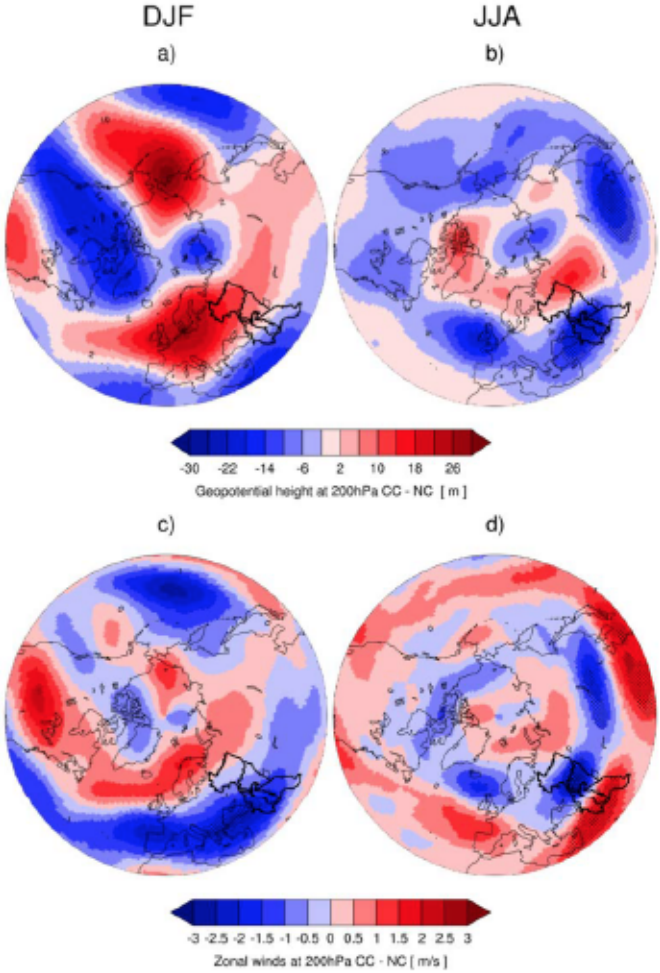

Figure 5.12: Winter and summer changes for current CS- no CS scenario for (a-b) geopotential height and (c-d) zonal winds at 200 hPa showing the location of the jet stream. Stippling indicates significance at 95% (t-test).

The presence of different CS areas affects the atmospheric circulation patterns much higher in the atmosphere (at the 500 hPa and the 200 hPa levels) via changes in geopotential height and zonal winds. We firstly examined winter and summer changes for the geopotential height and the location of the jet stream by investigating the zonal winds at the 200 hPa level (Fig. 5.12). The seasonal responses of both to the presence of different CS areas during winter and summer show high variability, especially in the structure of subtropical jet stream (Fig. 5.12c, d). It appears that reduced summer surface temperatures (Fig. 5.9b) can trigger a reduction in the

summer geopotential height (~28 m) (Fig. 5.12b) with a resultant enhanced summer north-south dipole pattern in westerly winds over southern CS, from the Mediterranean Sea to east Asia and a reduced northward tilt over the northern CS (Fig. 5.12d).

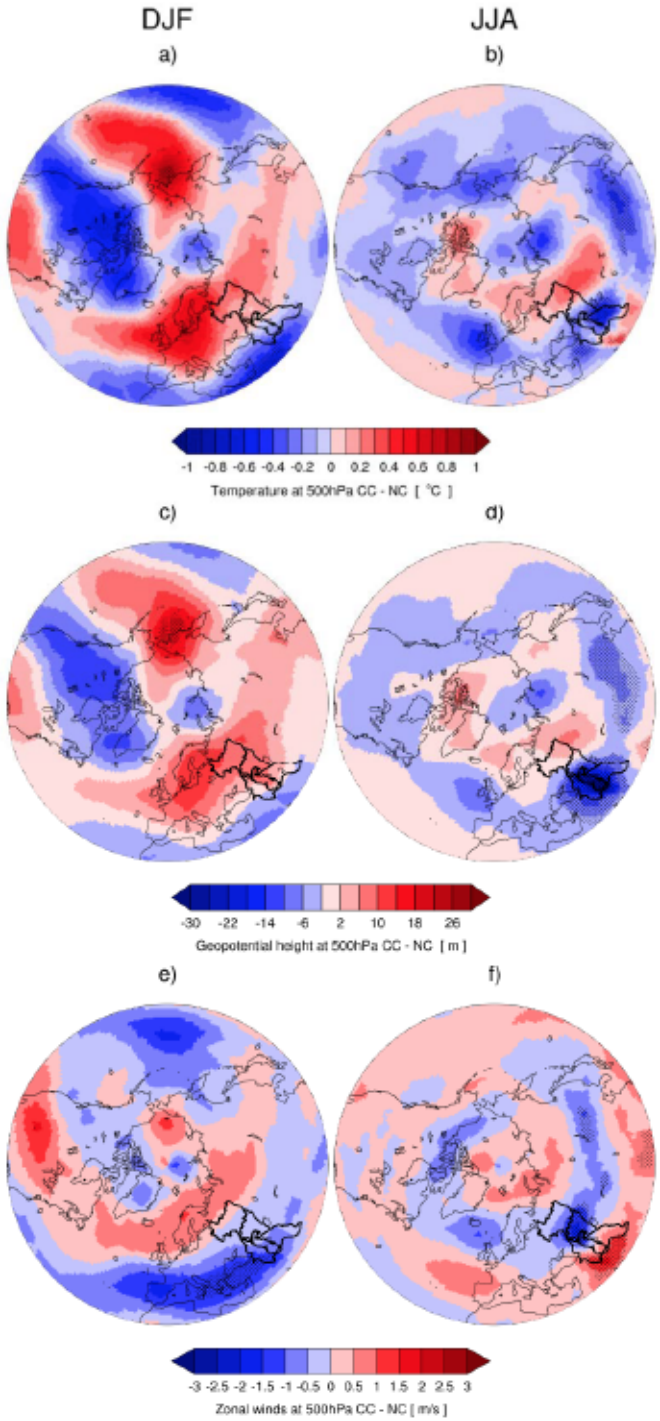

Figure 5.13: Winter and summer changes for current CS- no CS scenario for (a-b) temperature, (c-d) geopotential height and (e-f) zonal winds at the 500 hPa level.

A possible explanation for the strong southwards shift in the jet stream arises from horizontal temperature gradients between warm and cold regions which influence the westerlies as also

seen in Farley-Nichols & Toumi (2013). It is plausible be that surface temperature signals propagate up to higher atmospheric levels, which changes the geopotential height. The above summer relationship is consistent at the 500 hPa level as well (Fig. 5.13) and our results show that, the summer temperatures indeed influence the reduction in geopotential height anomalies (-30 m) which results in the same (but weaker) dipole pattern of the jet stream (Fig. 5.13b, d, f). The results of this study suggest that the presence of different CS areas affect large-scale climate over the entire northern hemisphere.

5.4 Discussion

Our simulated results suggest that the presence of different CS areas (when compared with a no CS scenario) affect the climate in the regional catchment area and large-scale circulation patterns in the northern hemisphere. We note that both precipitation and evaporation increase (decrease) with a larger (smaller) CS area; as a larger CS can produce and contribute to more moisture to this region compared to a smaller or no CS, particularly during late autumn–early winter, when cold, dry air masses pass over the relatively warm CS given the high heat capacity of the sea. Our results highlight that evaporation plays a significant role on the CSL variability similar to seen in the investigations by (Chen *et al.*, 2017). A clearly enhanced precipitation in the SW of the CS is seen in our study, which was not found by Arpe *et al*. (2018) but shown by Farley-Nichols & Toumi (2013). During the winter, precipitation changes tend to follow evaporation, however, these changes are not linearly related throughout the year (similar to Farley-Nicholls & Toumi, 2013). The impacts on evaporation and precipitation are smaller during spring. A partial explanation for this lies in the contrasting seasonal thermodynamics (and thermal inertia of the sea) and atmospheric moisture recycling changing in each CS area simulations. Also, the summer atmospheric moisture recycling and distribution is known to play a key role in changing the regional climate (and convective stability). In particular, the amount of atmospheric moisture available is driven by the temperature difference between surface atmosphere and sea surface and surface winds and this relationship changes upon a given CS area.

Of key interest in our study are the impacts of the changing CS areas on specific regions in the northern hemisphere. In particular, we examine and discuss three main large-scale relationships seen in the simulations: 1) The impact of surface air temperatures extending towards east

Siberia and northwest Pacific during the winter. 2) The impact of enhanced precipitation in the central Asia region during summer. 3) The impact of surface temperature on upper atmospheric geopotential height and zonal winds.

The first association focuses on the impact of enhanced winter surface air temperatures which extends as far as east Siberia and northwest Pacific. These temperatures increase based on larger area changes and vice versa and are relative to a no CS scenario. This enhanced warming over north-western Pacific can be driven by changes in CS area dependent air masses (strong westerlies and convective instabilities during winter). During winter, the presence of the CS (when compared with no CS) leads to reduction in atmospheric stability due to CS being warmer than the surrounding air temperatures. Hence, the seasonal temperature leads to atmospheric instability (implications on cyclogenesis), during winter and greater stability (anti-cyclogenesis) during summer (Arpe *et al.*, 2018; Farley-Nichols & Toumi, 2013). However, the warming over the northwest Pacific can be attributed to the Pacific decadal oscillation, but this is not investigated in our study. Moreover, it is quite plausible that the above changes are affected by a no CS scenario, comparable to a similar situation such as that seen for the nearby Aral Sea (McDermid & Winter, 2017; Small *et al.*, 2001). Interestingly, the temperature changes are linked to the sea level pressure changes which show similar pattern for the same region, highlighting surface temperatures as drivers of low-level atmospheric circulation. Typically, enhanced (warmer) surface temperatures initiate updrafts, with resultant effects on low sea level pressure. Moreover, the winter season around the CS catchment area (relative to no CS scenario) is dominated by lower pressure, stronger low-level winds and increased moisture (enhanced temperature and evaporation changes).

The second connection focuses on the impact of enhanced summer precipitation in the central Asia region which can be associated with surface winds and westerly winds which transports moisture afield. However, the westerlies are stronger in winter. Yet, it is likely that these winds pick up moisture over the sea and transport towards the eastern dry plains near central Asia (Arpe *et al.*, 2019). Also, the generally westerly flow in winds is disturbed by the Caucasus mountains and restricted by the southern Elburz mountains. During the summer, associated reduced surface temperatures, high pressure gradients and weaker westerlies are seen relative to no CS scenario. Given this, it is interesting that the summer precipitation increases with larger area changes (high moisture capacity) and vice versa and are relative to a

no CS scenario. A second potential explanation is that the summer Indian monsoon is driving the high precipitation variability over central Asia from the Far East (Schiemann *et al.*, 2007).

The third link focuses on the impact of temperature on upper atmospheric geopotential height and zonal winds resulting in a shift in the location of the jet stream that influence changes in circulation patterns. Here we discuss two aspects; first our results suggest the widening of the 500 hPa troughs with smaller CS area on the northern Pacific and vice versa. In the Northern Hemisphere, two frontal zones are best developed at the 500 hPa level, initiating a strong thermal gradient at the 500 hPa level that can be projected via the Rossby waves or stationary waves (Hoskins, 1981). These wave trains in the upper atmosphere intensify due to stronger winds from the north; induced from a difference in temperature gradients. Hence a thermal response (for changes in the temperatures at the 500 hPa level) can be responsible for triggering the wave pattern seen in the geopotential height at the 500 hPa level.

The second aspect of the third link relates to the southward shift in the location of the summer jet stream. The presence of different CS areas is seen to influence the atmospheric circulation patterns much higher in the atmosphere (at the 500 hPa and the 200 hPa levels). During the summer, surface temperatures influence a reduction in geopotential height at the 200 hPa level (-28 m) and an associated southward shift in the jet stream at 200 hPa. Typically, strong surface temperatures can influence changes in the upper atmospheric geopotential height field, and impact the zonal wind field due to the geostrophic height-wind relationship. Here, we note the presence of different CS areas affect the thermal gradient, which drives the jet stream speed and location. In particular, this summer relationship for a surface thermal response triggering the reduction in geopotential height anomalies which result in similar enhanced dipole pattern in the jet stream at the 200 hPa level is seen in the regional modeling study by Farley-Nichols & Toumi (2013). However, we have also tested this summer relationship at the 500 hPa level and can show that the summer temperatures at the 500 hPa level indeed influence the reduction in geopotential height anomalies (-30 m), that results in the same (but weaker) dipole pattern of the jet stream seen previously at the 200 hPa level. It is also comparable with the Great Lakes studies by Lofgren (1997) that lead to a poleward shift in the winter jet stream due to stronger meridional temperature gradient being intensified in the north and weakened in the south. Also, our study agrees with the regional limited study of Farley-Nichols & Toumi (2013) and further contributes to our new simulated results by including different realistic CS areas, using a state-of-the-art high-resolution coupled climate model and the improving the

interpretation between the CS changing surface areas and the large-scale physical processes over the Northern Hemisphere.

Our study involves some caveats that can limit the detailed understanding of the regional and large-scale climate over the northern hemisphere (e.g. moisture cycle is more pronounced on hourly, daily and weekly basis). The default version of the CESM includes a prescribed (larger) CS surface area. This affects realistic CS moisture transports that influence the atmospheric water budget and the feedback of CSL variability. By performing idealized simulations of four CS area changes, our findings aid in recognizing regional and large-scale climate impacts of the CS and strongly indicate that the inclusion of a realistic CS area representation is essential in future climate model developments.

5.5 Conclusions

Our new results propose that the presence of different CS areas affect the regional climate over the CS catchment area as well as large-scale climate over the northern hemisphere and contributes to the improved interpretation between the CS changing surface areas and the large-scale physical processes over the Northern Hemisphere. When compared to a no CS scenario, evaporation over the sea increases with increasing area, while precipitation increases over southwestern CS with increases in surface area. The presence of CS areas has a strong impact on surface air temperatures due to its thermal inertia, reducing temperatures in summer and increasing it in winter. This leads to enhanced precipitation over central Asia and increased warming over north-western Pacific during winter. The temperature and precipitation changes during different CS surface areas affect large-scale circulation and disturbance in wave trains resulting in a widening of the 500 hPa troughs on the northern Pacific region; as seen for the smaller CS area scenario. Furthermore, our results suggest a summer relationship of surface temperatures which trigger a reduction in geopotential height anomalies that can result in enhanced north-south dipole pattern and a southward shift in the jet stream at the 200 hPa and 500 hPa level.

Our results underline that an accurate representation of the CS is important to avoid bias when evaluating the climate processes over this region like changes in temperature, evaporation and the subtropical jet stream for climate models. This study allows for an accurate estimate of the

change of the CSL from the change in the CS surface areas when compared to a simulation carried out with an inaccurate CS area. Our study shares implications for exploring these realistic CS surface areas under past climate states as well as climate projections for the 21st century and can provide vital assessments for identifying climate impacts of changing CS surface areas.

Acknowledgements

This project has received funding from the European Union's Horizon 2020 research and innovation programme under the Marie Sklodowska-Curie grant agreement No 642973. All CESM simulations were performed on the supercomputer of the Norddeutscher Verbund für Hoch- und Höchstleistungrechnen (HLRN3). The processing charges for this open access publication were covered by the University of Bremen.

Chapter 6

6 Conclusions and Outlook

Both paleoclimate reconstructions regarding the extreme changes in Caspian Sea level (CSL) during the late Quaternary, and climate modelling regarding the CSL by the end of the 21st century, have been of keen interest, heavily debated and uncertain. Understanding the global mechanisms for regional CSL changes is complex, but essential for predicting the CSL under future climate change. In this study, a climate modeling approach was used to identify the physical mechanisms for the long-term variations in the water budget (precipitation and evaporation; P-E) of the Caspian Sea (CS) that lead to changes in the CSL; as well as to assess the CESM1.2.2 model skill in representing different climate states for the CS. To this end, a large set of paleo climate, present-day and future simulations were designed for the above, and the new results offer fresh perspectives on the relationship between the northern hemispheric climate events and the CS catchment area during the late Quaternary to the end of the 21st century. Here, we summarise the key insights gained from research questions examined in the three chapters.

The results of the first chapter clearly suggest that regional changes in the CS water budget are influenced by global glacial and interglacial climate conditions. The CESM1.2.2 constrains the timings for the major CS transgressions and regressions as well as identifies the climate conditions favourable for the occurrence of these events during the Late Quaternary; leaving aside potential changes in river hydrography, and compared with the selected paleoclimate reconstructions. However, the model cannot capture all selected reconstructions for the above, based solely on water budget changes; in particular during the Heinrich Stadial1. Insolation-controlled summer meltwater and a weakened in the Atlantic Meridional Overturning Circulation strength potentially play a primary role during the early and late phases of Heinrich Stadial1 that are quite different and affect the catchment area in different ways. Based on CESM ice sheet data, and the selected reconstructions, it is clear that meltwater is responsible for the two reconstructed high stands seen during the deglaciation (at 16 and 14 kyr BP). Here, the CESM positive water budget and climate conditions only capture one highstand (~14 kyr BP), since the model does not include a sophisticated meltwater routing into the CS, making

comparisons with the selected reconstructions complicated. Compared with the pre-industrial climate, the warmer and wetter interglacial climates result in a positive CS water budget and agree with the selected reconstructed transgressions; based on a combination of weakened winter westerlies (denoting a negative NAO-like pattern) and insolation enhanced summer precipitation. The glacial Marine Isotope 3 interstadial climate is clearly driven by enhanced thermal influenced winter precipitation over the North Atlantic and the larger CS region, resulting in a positive water budget that identify to a transgression; analogous to reconstructions. The North Atlantic winter climate variability and ice sheet dynamics control the colder and drier conditions of the Last Glacial Maximum that lead to a negative water budget; leading to a regression, and concur with the reconstructions.

The second chapter suggests that the present and future changes (1850-2100 CE) in the winter North Atlantic Oscillation (NAO) clearly impact the Caspian Sea hydroclimate and CSL. The CESM1.2.2 with CAM5 atmosphere physics and 1° resolution shows the best skill in simulating the NAO, when compared to the 1° CAM4 or 2° CAM4 versions. The present-day winter NAO enhances winter precipitation over the Volga catchment area. Similarly, the future projection of RCP4.5 suggest higher precipitation over the Volga; but, the RCP8.5 proposes a more interesting cancelling effect of the NAO on P-E, with a north (increase)- south (decrease) dipole pattern in the NAO centres of action over the entire catchment area. This insinuates that the correlation between future winter NAO and the Caspian water budget is not stable and depends on the changing background climate and shifts in the location and magnitude of the NAO centres of action. In particular, the key result of future climate warming is related to increasing summer evaporation over the CS surface. Hence, despite increasing winter precipitation over the northern catchment area, the increasing summer evaporation over the sea is stronger and results in a negative water budget with an additional CSL drop of ca. 9 m (RCP4.5) to 18 m (RCP8.5) by the end of the 21st century; larger than future CSL from previous modeling studies. Such CSL decline can significantly impact the Caspian region, mainly the shallow (< 5 m water depth) northern Caspian catchment area. Because the CESM1.2.2 model includes an inaccurate CS surface area that is larger when compared to present-day, the calculated CSL drop can be overestimated.

In order to assess the impacts of different Caspian Sea surface areas on the regional water budget as well as large-scale atmospheric circulation patterns, the results from the third chapter focus on the relationship of a larger, current and smaller CS surface area; when compared to a

no CS. The model essentially confirmed that the presence of different Caspian Sea areas substantially affects the regional and upper atmospheric large-scale climate over the northern hemisphere. Regional changes in the CS catchment area appear to be driven by these changing CS surface areas. When compared to a no Caspian Sea scenario, a larger CS area suggests higher evaporation over the sea and higher precipitation over the south-west catchment area and vice versa for a smaller CS. Seasonally, the presence of a larger Caspian Sea area reduces (increases) surface temperatures in summer (winter) that triggers a resultant southward shift and increased speed in the subtropical jet stream at the 200 hPa and 500 hPa level. These changes in the upper atmospheric circulation lead to increased summer precipitation over central Asia and increased winter warming over the north-western Pacific; possibly via changes in the Rossby waves. Hence, including a correct Caspian Sea area is important to avoid model bias when evaluating for the above, as well as estimating changes in CSL when compared to simulations involving an inaccurate Caspian Sea area. In this context, exploring realistic Caspian Sea surface areas for past climate states and projections for the 21st century can provide improved and realistic assessments for identifying changes in CSL.

In this study, the CESM1.2.2 model has considerably contributed to improved understanding of the physical interactions between the large-scale climate over the Northern Hemisphere and the regional hydroclimate variations in the CS by constraining the selected reconstructions. However, the CESM model is limited in identifying and constraining all the CS transgressions and regressions during the late Quaternary, solely based on precipitation and evaporation changes. In particular, future modeling studies should consider integrating regional geological archives for estimates of ice sheet dynamics (growth and melting), paleo- hydrography changes and a proper implementation of a sophisticated meltwater routing into the CS that can provide a more realistic assessment of the meltwater impact during paleo climate, e.g., during the late stage in Heinrich Stadial1. For a realistic assessment of the potential biases, future CESM and other climate model developments should include the correct Caspian Sea surface area representations that are the best representative of past geologic and present periods; in order to predict most likely CSL changes under future scenarios.

Producing climate ensembles and transient climate simulations with precise CS surface areas can contribute to constraining the paleoclimate reconstructions for changes in the CS catchment area. At the regional scale, there is a need for a better integration of geologic archives and climate models in simulating a realistic Caspian Sea climate and to better validify the predictive

ability of high-resolution climate models for the physical mechanisms for changes in CSL throughout the 21st century. However, CESM1.2.2 is recognised to be robust at improving the interpreting of reconstructions and at representing present-day climate conditions. This installs a greater confidence in the model projections and interpretations regarding the climate and hydroclimate conditions for the Caspian Sea catchment area by the end of the 21st century.

Of particular concern is that the extreme CSL changes calculated from this study can occur before 2100, as the latest assessment by the IPCC special report highlighting impacts of global warming of 1.5°C above pre-industrial levels suggest dire changes as early as 2030 (Hoegh-Guldberg *et al.*, 2018). A rapid decline in the Caspian Sea poses well-known risks; similar to the nearby Aral Sea, which is a prime example of rapid lake shrinkage and the effects this has on the surrounding societies, agriculture, fisheries and the ecosystem. Similarly, the Caspian Sea's highly valuable resources are integral to the surrounding countries, and while further man-made developments can substantially change this region, the predicted future scorching summer climate certainly plays a key role. Conversely, the winter NAO can enhance winter precipitation / river runoff flow into the Volga and the Caspian Sea. However, the increased summer evaporation plays the key role in rapid Caspian Sea shrinkage and this trend is highly likely to continue with higher temperatures influencing stronger evaporation by the end of the 21st century. Given the large longitude of the CS catchment area, the influence of large-scale climate events on the precipitation and evaporation dominating the CSL and changes in this sensitive balance should be investigated constantly and in more detail in the next decades.

References

Akesson, H., Morlighem, M., Nisancioglu, K. H., Svendsen, J. I., & Mangerud, J. (2018). Atmosphere-driven ice sheet mass loss paced by topography: Insights from modelling the south-western Scandinavian Ice Sheet. *Quaternary Science Reviews, 195*, 32-47. doi:https://doi.org/10.1016/j.quascirev.2018.07.004

Allen, R., Pereira, L., Raes, D., & Smith, M. (1998). Crop Evapotranspiration. Guidelines for Computing Crop Water Requirements (Vol. 56).

Amante, C. a. B. W. E. (2009). ETOPO1 1 Arc-Minute Global Relief Model: Procedures, Data Sources and Analysis. In N. National Geophysical Data Center (Ed.), *NOAA Technical Memorandum NESDIS NGDC-24*.

Aondover, T. (2013). *Climate Variability- regional and thematic patterns*: IntechOpen.

Arpe, K., Bengtsson, L., Golitsyn, S., Mokhov, I. I., Semenov, V. A., & Sporyshev, P. V. (1999). Analysis and modeling of the hydrological regime variations in the Caspian Sea basin. *Dokl., Earth Sci., 366*(4), 552–556.

Arpe, K., Bengtsson, L., Golitsyn, S., Mokhov, I. I., Semenov, V. A., & Sporyshev, P. V. (2000). Connection between Caspian Sea level variability and ENSO. *Geophys. Res. Lett., 27*, 2693–2696.

Arpe, K., & Leroy, S. (2007). The Caspian Sea level forced by the atmospheric circulation, as observed and modelled. *Quat. Int., 173–174*, 144–152. doi:10.1016/j.quaint.2007.03.008

Arpe, K., Leroy, S., Lahijani, H., & Khan, V. (2012). Impact of the European Russia drought in 2010 on the Caspian Sea level. *Hydrol. Earth Syst.Sci., 16*, 19–27. doi:10.5194/hess-16-19-2012.

Arpe, K., Leroy, S., & U, M. (2011). *The last glacial maximum locations of summer-green tree refugia using simulations with ECHAM3 T42 uncoupled, ECHAM5 T31 coupled and ECHAM5 T106 uncoupled models* (Vol. 6).

Arpe, K., Molavi-Arabshahi, M., & Leroy, S. A. G. (2019). Wind variability at the South Caspian Sea during the last 60 years, their connections with the Caspian Sea level and ENSO.

Arpe, K., & Roeckner, E. (1999). Simulation of the hydrologic cycle over Europe: Model validation and impacts of increasing green-house gases. *Adv. Water Res, 23*, 105-119.

Arpe, K., Tsuang, B.-J., Tseng, Y.-H., Liu, X.-Y., & Leroy, S. A. G. (2018). Quantification of climatic feedbacks on the Caspian Sea level variability and impacts from the Caspian Sea on the large-scale atmospheric circulation. *Theoretical and Applied Climatology*. doi:https://doi.org/10.1007/s00704-018-2481-x

Arslanov, K. A., Yanina, T. A., Chepalyga, A. L., Svitoch, A. A., Makshaev, R. R., Maksimov, F. E., et al. (2016). On the age of the Khvalynian deposits of the Caspian Sea coasts according to 14C and 230Th/234U methods. *Quaternary International, 409*, 81-87. doi:https://doi.org/10.1016/j.quaint.2015.05.067

Bakker, P., & Renssen, H. (2014). Last interglacial model–data mismatch of thermal maximum temperatures partially explained. *Clim. Past, 10*(4), 1633-1644. doi:10.5194/cp-10-1633-2014

Barnston, A. G., & Livezey, R. E. (1987). Classifications, Seasonality, and Persistence of Low-Frequency Atmospheric Circulation Patterns. *Monthly Weather Review, 115*, 1083-1126.

Bezrodnykh, Y. P., Deliya, S. V., Romanyuk, B. F., Fedorov, V. I., Sorokin, V. M., & Luksha, V. L. (2014). Holocene deposits in the Mangyshlak Peninsula, North Caspian Sea region. *Stratigraphy and Geological Correlation, 22*(4), 426-445. doi:10.1134/s0869593814040030

Bezrodnykh, Y. P., & Sorokin, V. M. (2017). On the age of the Mangyshlakian deposits of the northern Caspian Sea. *Quaternary Research, 85*(2), 245-254. doi:10.1016/j.yqres.2016.01.004

Braconnot, P., Harrison, S. P., Kageyama, M., Bartlein, P. J., Masson-Delmotte, V., Abe-Ouchi, A., et al. (2012). Evaluation of climate models using palaeoclimatic data. *Nature Climate Change, 2*, 417. doi:10.1038/nclimate1456

Briggs, R. D., Pollard, D., & Tarasov, L. (2014). A data-constrained large ensemble analysis of Antarctic evolution since the Eemian. *Quaternary Science Reviews, 103*, 91-115. doi:https://doi.org/10.1016/j.quascirev.2014.09.003

Broecker, W., Bond, G., Klas, M., Clark, E., & McManus, J. (1992). Origin of the northern Atlantic's Heinrich events. *Climate Dynamics, 6*(3), 265-273. doi:10.1007/BF00193540

Broecker, W. S., Peng, T. H., Jouzel, J., & Russell, G. (1990). The magnitude of global fresh-water transports of importance to ocean circulation. *Climate Dynamics, 4*(2), 73-79. doi:10.1007/BF00208902

Broström, A., Coe, M., Harrison, S. P., Gallimore, R., Kutzbach, J. E., Foley, J., et al. (1998). Land surface feedbacks and palaeomonsoons in northern Africa. *Geophysical Research Letters, 25*(19), 3615-3618. doi:10.1029/98gl02804

Bueh, C., & Nakamura, H. (2007). Scandinavian pattern and its climatic impact. *Q. J. R. Meteorol. Soc., 133*, 2117-2131.

Chang, E. K. M., Guo, Y., & Xia, X. (2012). CMIP5 multimodel ensemble projection of storm track change under global warming. *Journal of Geophysical Research: Atmospheres, 117*(D23). doi:10.1029/2012jd018578

Chen, D., & Chen, H. W. (2013). Using the Köppen classification to quantify climate variation and change: An example for 1901–2010. *Environmental Development, 6*, 69-79. doi:https://doi.org/10.1016/j.envdev.2013.03.007

Chen, J. L., Pekker, T., Wilson, C. R., Tapley, B. D., Kostianoy, A. G., Cretaux, J. F., et al. (2017). Long-term Caspian Sea level change. *Geophys. Res. Lett, 44*, 6993–7001. doi:10.1002/2017GL073958

Chepalyga, A. L. (2007). The late glacial great flood in the Ponto-Caspian basin. In V. Yanko-Hombach, A. S. Gilbert, N. Panin, & P. M. Dolukhanov (Eds.), *The Black Sea Flood Question: Changes in Coastline, Climate, and Human Settlement* (pp. 119-148). Dordrecht: Springer Netherlands.

Coe, M. T. (1998). A linked global model of terrestrial hydrologic processes: Simulation of modern rivers, lakes, and wetlands. *Journal of Geophysical Research: Atmospheres, 103*(D8), 8885-8899. doi:10.1029/98jd00347

Coe, M. T. (2000). Modeling Terrestrial Hydrological Systems at the Continental Scale: Testing the Accuracy of an Atmospheric GCM. *Journal of Climate, 13*(4), 686-704. doi:10.1175/1520-0442(2000)013<0686:Mthsat>2.0.Co;2

Coe, M. T., & Bonan, G. B. (1997). Feedbacks between climate and surface water in northern Africa during the middle Holocene. *Journal of Geophysical Research: Atmospheres, 102*(D10), 11087-11101. doi:10.1029/97jd00343

Collins, M., Knutti, R., Arblaster, J., Dufresne, J.-L., Fichefet, T., Friedlingstein, P., et al. (2013). Long-term Climate Change: Projections, Commitments and Irreversibility. In T. F. Stocker, D. Qin, G.-K. Plattner, M. Tignor, S. K. Allen, J. Boschung, A. Nauels, Y. Xia, V. Bex, & P. M. Midgley (Eds.), *Climate Change 2013: The Physical Science Basis. Contribution of Working Group I to the Fifth Assessment Report of the Intergovernmental Panel on Climate Change* (pp. 1029–1136). Cambridge, United Kingdom and New York, NY, USA: Cambridge University Press.

Comas-Bru, L., & McDermott, F. (2014). Impacts of the EA and SCA patterns on the European twentieth century NAO–winter-climate relationships. *Q. J. R. Meteorol. Soc., 140*, 354–363. doi:10.1002/qj.2158

Contoux, C., Jost, A., Ramstein, G., Sepulchre, P., Krinner, G., & Schuster, M. (2013). Megalake Chad impact on climate and vegetation during the late Pliocene and the mid-Holocene. *Climate of the Past, 9*, 1417-1430. doi:10.5194/cp-9-1417-2013

Davini, P., & Cagnazzo, C. (2014). On the misinterpretation of the North Atlantic Oscillation in CMIP5 models. *Climate Dynamics, 43*(5), 1497-1511. doi:10.1007/s00382-013-1970-y

Dee, D. P., Uppala, S. M., Simmons, A. J., Berrisford, P., Poli, P., Kobayashi, S., et al. (2011). The ERA-Interim reanalysis: configuration and performance of the data assimilation system. *Quarterly Journal of the Royal Meteorological Society, 137*(656), 553-597. doi:10.1002/qj.828

Deser, C., Hurrell, J. W., & Phillips, A. (2017). The role of the North Atlantic Oscillation in European climate projections. *Clim Dyn, 49*(9-10), 3141–3157.

Di Nezio, P. N., Timmermann, A., Tierney, J. E., Jin, F.-F., Otto-Bliesner, B., Rosenbloom, N., et al. (2016). The climate response of the Indo-Pacific warm pool to glacial sea level. *Paleoceanography, 31*(6), 866-894. doi:doi:10.1002/2015PA002890

Dolukhanov, M. P., L Chepalyga, A., K Shkatova, V., V Lavrentiev, N., & P Karpinsky, A. (2009). *Late Quaternary Caspian: Sea-Levels, Environments and Human Settlement* (Vol. 2).

Elguindi, N., & Giorgi, F. (2006a). Projected changes in the Caspian Sea level for the 21st century based on the latest AOGCM simulations. *Geophys. Res. Lett, 33*(8). doi:10.1029/2006GL025943

Elguindi, N., & Giorgi, F. (2006b). Simulating multi-decadal variability of Caspian sea level changes using regional climate model outputs. *Clim Dyn., 26*, 167–181.

Elguindi, N., & Giorgi, F. (2007). Simulating future Caspian sea level changes using regional climate model outputs. *Clim Dyn., 28*, 365–379.

Farley-Nichols, J., & Toumi, R. (2013). On the Lake Effects of the Caspian Sea. *Q. J. R. Meteorol. Soc.,, 140*, 1399-1408. doi:10.1002/qj.2222

Flato, G., Marotzke, J., Abiodun, B., Braconnot, P., Chou, S. C., Collins, W. J., et al. (2013). Evaluation of Climate Models. In: Climate Change 2013: The Physical Science Basis. Contribution of Working Group I to the Fifth Assessment Report of the Intergovernmental Panel on Climate Change *Climate Change 2013* (pp. 741-866): Cambridge University Press.

Forte, A. M., & Cowgill, E. (2013). Late Cenozoic base-level variations of the Caspian Sea: a review of its history and proposed driving mechanisms. . *Paleogeogr. Palaeoclimatol.Palaeoecol, 386*, 392-407.

Gent, P. R., Danabasoglu, G., Donner, J. L., Holland, M. M., Hunke, E. C., Jayne, S. R., et al. (2011). The Community Climate System Model Version 4. *J. Climate, 24*,(4973–4991).

Golitsyn, G. S., Dzyuba, A. V., Osipov, A. G., & Panin, G. N. (1990). Regional climate changes and their manifestations in the present-day rise in the Caspian Sea level. *Dokl. Akad. Nauk SSSR., 313*(5), 1224–1227.

Hoegh-Guldberg, O., Jacob, D., Taylor, M., Bindi, M., Brown, S., Camilloni, I., et al. (2018). Chapter 3: Impacts of 1.5°C global warming on natural and human systems. In: Global Warming of 1.5 °C. An IPCC special report on the impacts of global warming of 1.5 °C above preindustrial levels and related global greenhouse gas emission pathways [...] (pp. 175-311).

Huber, C., Leuenberger, M., Spahni, R., Flückiger, J., Schwander, J., Stocker, T., et al. (2006). *Isotope calibrated Greenland temperature record over Marine Isotope Stage 3 and its relation to CH4* (Vol. 243).

Hughes, A. L. C., Gyllencreutz, R., Lohne, Ø. S., Mangerud, J., & Svendsen, J. I. (2016). The last Eurasian ice sheets – a chronological database and time-slice reconstruction, DATED-1. *Boreas, 45*(1), 1-45. doi:doi:10.1111/bor.12142

Hunke, E. C., & Lipscomb, W. H. (2010). *CICE: The Los Alamos Sea Ice Model, Documentation and Software User's Manual, Version 4.1*. Retrieved from

Hurrell, J. W. (1995). Decadal trends in the North-Atlantic Oscillation: regional temperatures and precipitation. *Science, 269*:, 676-679.

Hurrell, J. W., & Deser, C. (2009). North Atlantic climate variability: The role of the North Atlantic Oscillation. *Journal of Marine Systems, 78*(1), 28-41. doi:https://doi.org/10.1016/j.jmarsys.2008.11.026

Hurrell, J. W., Holland, M. M., & Gent, P. R. (2013). The Community Earth System Model: A Framework for Collaborative Research. *B. Am. Meteorol. Soc., 94*(9), 1339–1360.

Hurrell, J. W., & van Loon, H. (1997). Decadal variations in climate associated with the North Atlantic Oscillation. *Climatic Change, 36*(3), 301-326. doi:10.1023/a:1005314315270

Ivanovic, R. F., Gregoire, L. J., Kageyama, M., Roche, D. M., Valdes, P. J., Burke, A., et al. (2016). Transient climate simulations of the deglaciation 21–9 thousand years before present (version 1) – PMIP4 Core experiment design and boundary conditions. *Geosci. Model Dev., 9*(7), 2563-2587. doi:10.5194/gmd-9-2563-2016

Justino, F., & Peltier, W. R. (2005). The glacial North Atlantic Oscillation. *Geophysical Research Letters, 32*(21). doi:10.1029/2005gl023822

Kageyama, M., Merkel, U., Otto-Bliesner, B., Prange, M., Abe-Ouchi, A., Lohmann, G., et al. (2013). Climatic impacts of fresh water hosing under Last Glacial Maximum conditions: a multi-model study. *Clim. Past, 9*(2), 935-953. doi:10.5194/cp-9-935-2013

Kageyama, M., Valdes, P. J., Ramstein, G., Hewitt, C., & Wyputta, U. (1999). Northern Hemisphere Storm Tracks in Present Day and Last Glacial Maximum Climate Simulations: A Comparison of the European PMIP Models. *Journal of Climate, 12*(3), 742-760. doi:10.1175/1520-0442(1999)012<0742:Nhstip>2.0.Co;2

Kakroodi, A. A., Kroonenberg, S. B., Goorabi, A., & Yamani, M. (2014). Shoreline Response to Rapid 20th Century Sea-Level Change along the Iranian Caspian Coast. *Journal of Coastal Research*, 1243-1250. doi:10.2112/jcoastres-d-12-00173.1

Kakroodi, A. A., Leroy, S. A. G., Kroonenberg, S. B., Lahijani, H. A. K., Alimohammadian, H., Boomer, I., et al. (2015). Late Pleistocene and Holocene sea-level change and coastal paleoenvironment evolution along the Iranian Caspian shore. *Marine Geology, 361*, 111-125. doi:https://doi.org/10.1016/j.margeo.2014.12.007

Kalnay, E., Kanamitsu, M., Kistler, R., Collins, W., Deaven, D., Gandin, L., et al. (1996). The NCEP/NCAR 40-Year Reanalysis Project. *Bull. Amer. Metero. Soc., 77*, 437-471.

Kindler, P., Guillevic, M., Baumgartner, M., Schwander, J., Landais, A., & Leuenberger, M. (2014). Temperature reconstruction from 10 to 120 kyr b2k from the NGRIP ice core. *Clim. Past, 10*(2), 887-902. doi:10.5194/cp-10-887-2014

Kislov, A., Panin, A., & Toropov, P. (2014). Current status and palaeostages of the Caspian Sea as a potential evaluation tool for climate model simulations. *Quaternary International, 345*. doi:10.1016/j.quaint.2014.05.014

Kislov, A. V., & Toropov, P. A. (2007). Climate modeling results for the circum-Pontic region from the late Pleistocene to the mid-Holocene. In V. Yanko-Hombach, Gilbert, AS., Panin, N., Dolukhanov, PM. (Ed.), *in: Book on "The Black Sea Flood Question: Changes in Coastline, Climate, and Human Settlement"* (pp. 47–62): Springer.

Kosarev, A. N. (2005). Physico-geographical conditions of the Caspian Sea. In A. G. Kostianoy & A. N. Kosarev (Eds.), *The Caspian Sea Environment*. Berlin and Heidelberg, Germany: Springer.

Kosarev, A. N., Yablonskaya, E. A., & Ablonskia, E. A. (1994). *The Caspian Sea* (Vol. 20). The Hague, The Netherlands.: SPB Academic Publishing.

Krijgsman, W., Tesakov, A., Yanina, T., Lazarev, S., Danukalova, G., Van Baak, C. G. C., et al. (2019). Quaternary time scales for the Pontocaspian domain: Interbasinal connectivity and faunal evolution. *Earth-Science Reviews, 188*, 1-40. doi:https://doi.org/10.1016/j.earscirev.2018.10.013

Kroonenberg, S. B., Kasimov, N. S., & Lychagin, M. Y. (2008). The Caspian Sea: A natural laboratory for sea-level change. *Geography, Environment, Sustainability, 1*, 22-37.

Kroonenberg, S. B., Rusakov, G. V., & Svitoch, A. A. (1997). The wandering of the Volga delta: a response to rapid Caspian sea-level change. *Sedimentary Geology, 107*(3), 189-209. doi:https://doi.org/10.1016/S0037-0738(96)00028-0

Lamarque, J.-F., Kyle, G. P., Meinshausen, M., Riahi, K., Smith, S. J., van Vuuren, D. P., et al. (2011). Global and regional evolution of short-lived radiatively-active gases and aerosols in the Representative Concentration Pathways. *Climatic Change, 109*(1), 191. doi:10.1007/s10584-011-0155-0

Lawrence, D. M., Oleson, K. W., Flanner, M. G., Thornton, P. E., Swenson, S. C., Lawrence, P. J., et al. (2011). Parameterization improvements and functional and structural advances in version 4 of the Community Land Model. *J. Adv. Model. Earth Syst, 3*.

Lee, Y.-Y., & Black, R. X. (2013). Boreal winter low-frequency variability in CMIP5 models. *Journal of Geophysical Research: Atmospheres, 118*(13), 6891-6904. doi:10.1002/jgrd.50493

Leroy, S. A. G., Lahijani, H., Crétaux, J.-F., Aladin, N., & Plotnikov, I. (accepted). Past and current changes in the largest lake of the world: The Caspian Sea. In M. S. (Ed.), *Large Asian lakes in a changing world*: Springer.

Leroy, S. A. G., López-Merino, L., & Kozina, N. (2019). *Dinocyst records from deep cores reveal a reversed salinity gradient in the Caspian Sea at 8.5—4.0 cal ka BP* (Vol. 209).

Leroy, S. A. G., López-Merino, L., Tudryn, A., Chalié, F., & Gasse, F. (2014). Late Pleistocene and Holocene palaeoenvironments in and around the middle Caspian basin as reconstructed from a deep-sea core. *Quaternary Science Reviews, 101*, 91-110. doi:https://doi.org/10.1016/j.quascirev.2014.07.011

Leroy, S. A. G., Tudryn, A., Chalié, F., López-Merino, L., & Gasse, F. (2013). From the Allerød to the mid-Holocene: palynological evidence from the south basin of the Caspian Sea. *Quaternary Science Reviews, 78*, 77-97. doi:https://doi.org/10.1016/j.quascirev.2013.07.032

Liu, Z., Zhu, J., Rosenthal, Y., Zhang, X., Otto-Bliesner, B. L., Timmermann, A., et al. (2014). The Holocene temperature conundrum. *Proceedings of the National Academy of Sciences, 111*(34), E3501-E3505. doi:10.1073/pnas.1407229111

Lodh, A. (2015). *Impact of Caspian Sea Drying on Indian Monsoon Precipitation and Temperature as Simulated by Regcm4 Model* (Vol. 06).

Lofgren, B. M. (1997). Simulated Effects of Idealized Laurentian Great Lakes onRegional and Large-Scale Climate. *Journal of Climate, 10*(11), 2847-2858. doi:10.1175/1520-0442(1997)010<2847:seoilg>2.0.co;2

Masson-Delmotte, V., Schulz, M., Abe-Ouchi, A., Beer, J. r., Ganopolski, A., Gonz·lez Rouco, J. F., et al. (2013). Information from Paleoclimate Archives: PANGAEA.

McDermid, S. S., & Winter, J. (2017). Anthropogenic forcings on the climate of the Aral Sea: A regional modeling perspective. *Anthropocene, 20*, 48-60. doi:https://doi.org/10.1016/j.ancene.2017.03.003

McKay, N. P., Overpeck, J. T., & Otto-Bliesner, B. L. (2011). The role of ocean thermal expansion in Last Interglacial sea level rise. *Geophysical Research Letters, 38*(14). doi:doi:10.1029/2011GL048280

Meehl, G., Stocker, T., Collins, W. D., Friedlingstein, P., Gaye, A. T., Gregory, J. M., et al. (2007). *Global climate projections climate change 2007: The physical science basis.*

Meehl, G. A., Washington, W. M., Arblaster, J. M., Hu, A., Teng, H., Tebaldi, C., et al. (2012). Climate System Response to External Forcings and Climate Change Projections in CCSM4. *Journal of Climate, 25*(11), 3661-3683. doi:10.1175/jcli-d-11-00240.1

Meinshausen, M., Smith, S. J., Calvin, K. V., Daniel, J. S., Kainuma, M. L. T., Lamarque, J. F., et al. (2011). The RCP Greenhouse Gas Concentrations and their Extension from 1765 to 2300. *Climatic Change (Special Issue).* doi:10.1007/s10584-011-0156-z

Molavi-Arabshahi, M., Arpe, K., & Leroy, S. (2015). Precipitation and temperature of the southwest Caspian Sea region during the last 55 years: their trends and teleconnections with large-scale atmospheric phenomena. *International Journal of Climatology, 36*, 2156—2172.

Moss, R. H., A, E. J., Hibbard, K A., Manning, M R., Rose, S K., van Vuuren, D P., et al. (2010). The next generation of scenarios for climate change research and assessment. *Nature Climate Change, 463*, 747-756.

Naderi, B., Lahijani, H., Mousavi, H., Arpe, K., Leroy, S., Marriner, N., et al. (2013). Caspian Sea-level changes during the last millennium: historical and geological evidence from the south Caspian Sea. *Clim. Past, 9*, 1645—1665. doi:10.5194/cp-9-1645-2013

Nandini, S. D., Prange, M., Schulz, M., & Arpe, K. (revised). Past and future impact of North Atlantic winter teleconnections on the Caspian catchment area in CESM1.2.2. *International Journal of Climatology.*

Neale, R., Gettelman, A., Park, S., Conley, A., Kinnison, D., Marsh, D., et al. (2010). *Description of the NCAR community atmosphere model (CAM 5.0).* Retrieved from Natl. Cent. For Atmos. Res., Boulder, Colorado, USA:

Neale, R. B., Gettelman, A., Park, S., Chen, C. C., Lauritzen, P. H., Williamson, D. L., et al. (2012). *Description of the NCAR Community Atmosphere Model (CAM 5.0)*. Retrieved from Natl. Cent. For Atmos. Res., Boulder, Colorado, USA:

Ning, L., & Bradley, R. S. (2016). NAO and PNA influences on winter temperature and precipitation over the eastern United States in CMIP5 GCMs. *Climate Dynamics, 46*(3), 1257-1276. doi:10.1007/s00382-015-2643-9

North, G. R., Bell, T. L., Cahalan, R. F., & Moeng, F. J. (1982). Sampling Errors in the Estimation of Empirical Orthogonal Functions. *Monthly Weather Review, 110*(7), 699-706. doi:10.1175/1520-0493

Notaro, M., Holman, K., Azar, Z., Elody, F., Steve, V., & Val, B. (2013). Influence of the Laurentian Great Lakes on Regional Climate. *Journal of Climate, 26*(3), 789-804. doi:10.1175/jcli-d-12-00140.1

Otto-Bliesner Bette, L., Rosenbloom, N., Stone Emma, J., McKay Nicholas, P., Lunt Daniel, J., Brady Esther, C., et al. (2013). How warm was the last interglacial? New model–data comparisons. *Philosophical Transactions of the Royal Society A: Mathematical, Physical and Engineering Sciences, 371*(2001), 20130097. doi:10.1098/rsta.2013.0097

Otto-Bliesner, B. L., Braconnot, P., Harrison, S. P., Lunt, D. J., Abe-Ouchi, A., Albani, S., et al. (2017). The PMIP4 contribution to CMIP6 – Part 2: Two interglacials, scientific objective and experimental design for Holocene and Last Interglacial simulations. *Geosci. Model Dev., 10*(11), 3979-4003. doi:10.5194/gmd-10-3979-2017

Otto-Bliesner, B. L., Brady, E. C., Clauzet, G., Tomas, R., Levis, S., & Kothavala, Z. (2006). Last Glacial Maximum and Holocene Climate in CCSM3. *Journal of Climate, 19*(11), 2526-2544. doi:10.1175/jcli3748.1

Panin, G. N., & Dianskii, N. A. (2014). On the correlations between oscillations of the Caspian sea level and north Atlantic climate. *Izvestiya, Atmospheric & Oceanic Physics., 50*(3), 266-277. doi:10.1134/S000143381402008X

Panin, G. N., Solomonova, I. V., & Vyruchalkina, T. Y. (2014). Regime of Water Balance Components of the Caspian Sea. *Water Resour., 41*(5), 505-511.

Panin, G. N., Vyruchalkina, T. Y., & Solomonova, I. V. (2015). Effect of the North Atlantic on the Hydrological Regime of the Caspian Sea Basin. *Water Resour., 42*(4), 525-534.

Pausata, F. S. R., Li, C., J. Wettstein, J., Kageyama, M., & Nisancioglu, K. (2011). *The key role of topography in altering North Atlantic atmospheric circulation during the last glacial period* (Vol. 7).

Renssen, H., Longhead, B. C., Aerts, J. C., de Moel, H., Ward, P. J., & Kwadijk, J. C. J. (2007). Simulating long-term Caspian Sea level changes; The impact of Holocene and future climate conditions. *Earth and Planetary Science Letters, 261*, 685–693.

Rodionov, S. (1994). *Global and Regional Climate Interaction: The Caspian Sea Experience.*: Kluwer Academic Publications.

Rychagov, G. I. (1997). Holocene oscillations of the Caspian Sea, and forecasts based on palaeogeographical reconstructions. *Quaternary International, 41-42*, 167-172. doi:https://doi.org/10.1016/S1040-6182(96)00049-3

Schiemann, R., Glazirina, M. G., & Schär, C. (2007). On the relationship between the Indian summer monsoon and river flow in the Aral Sea basin. *Geophysical Research Letters, 34*(5). doi:10.1029/2006gl028926

Small, E. E., Sloan, L. C., & Nychka, D. (2001). Changes in Surface Air Temperature Caused by Desiccation of the Aral Sea. *Journal of Climate, 14*(3), 284-299. doi:10.1175/1520-0442(2001)014<0284:cisatc>2.0.co;2

Smith, R., Jones, P., Briegleb, B., Bryan, F., Danabasoglu, G., Dennis, J., et al. (2010). The parallel ocean program (POP) reference manual: Ocean component of the community climate system model (CCSM). *Tech. Note LAUR-10-01853, Los Alamos Natl. Lab., Los Alamos, N. M.*

Sorokin, V. M. (2011). Correlation of upper quaternary deposits and paleogeography of the Black and Caspian seas. *Stratigraphy and Geological Correlation, 19*(5), 563. doi:10.1134/S086959381104006X

Sorokin, V. M., Yanina, T. A., Bezrodnykh, Y., & Romanyuk, B. F. (2018). Identification and age of submarine Girkanian sediment beds (Upper Pleistocene) in the Caspian Sea. *Quaternary International, 465*, 152-157. doi:https://doi.org/10.1016/j.quaint.2016.08.044

Sousounis, P., & Fritsch, M. (1994). Lake-Aggregate Mesoscale Disturbances. Part II: A Case Study of the Effects on Regional and Synoptic-Scale Weather Systems. *Bulletin of the American Meteorological Society, 75*(10), 1793-1812. doi:10.1175/1520-0477(1994)075<1793:lamdpi>2.0.co;2

Srokosz, M., Baringer, M., Bryden, H., Cunningham, S., Delworth, T., Lozier, S., et al. (2012). Past, Present, and Future Changes in the Atlantic Meridional Overturning Circulation. *Bulletin of the American Meteorological Society, 93*(11), 1663-1676. doi:10.1175/bams-d-11-00151.1

Stoner, A. M. K., Hayhoe, K., & Wuebbles, D. J. (2009). Assessing General Circulation Model Simulations of Atmospheric Teleconnection Patterns. *Journal of Climate, 22*(16), 4348-4372. doi:10.1175/2009jcli2577.1

Stroeven, A. P., Hättestrand, C., Kleman, J., Heyman, J., Fabel, D., Fredin, O., et al. (2016). Deglaciation of Fennoscandia. *Quaternary Science Reviews, 147*, 91-121. doi:https://doi.org/10.1016/j.quascirev.2015.09.016

Svitoch, A. A. (2007). On the nature of the Khvalynian transgression of the Caspian Sea. *Oceanology, 47*(2), 282-289. doi:10.1134/S0001437007020142

Tarasov, L., Dyke, A. S., Neal, R. M., & Peltier, W. R. (2012). A data-calibrated distribution of deglacial chronologies for the North American ice complex from glaciological modeling. *Earth and Planetary Science Letters, 315-316*, 30-40. doi:https://doi.org/10.1016/j.epsl.2011.09.010

Taylor, K. E. (2001). Summarizing multiple aspects of model performance in a single diagram *JGR, 106*, 7183-7192.

Taylor, K. E., Stouffer, R. J., & Meehl, G. A. (2011). An Overview of CMIP5 and the Experiment Design. *Bulletin of the American Meteorological Society, 93*(4), 485-498. doi:10.1175/BAMS-D-11-00094.1

Trigo, R. M., Osborn, T. J., & Corte-Real, J. M. (2002). The North Atlantic Oscillation influence on Europe climate impacts and associated physical mechanisms. *Climate Research, 20*(1), 9-17.

Tudryn, A., Chalié, F., Lavrushin, Y. A., Antipov, M. P., Spiridonova, E. A., Lavrushin, V., et al. (2013). Late Quaternary Caspian Sea environment: Late Khazarian and Early Khvalynian transgressions from the lower reaches of the Volga river. *Quaternary International, 292*, 193-204.

Tudryn, A., Leroy, S. A. G., Toucanne, S., Gibert-Brunet, E., Tucholka, P., Lavrushin, Y. A., et al. (2016). The Ponto-Caspian basin as a final trap for southeastern Scandinavian Ice-Sheet meltwater. *Quaternary Science Reviews, 148*, 29-43. doi:https://doi.org/10.1016/j.quascirev.2016.06.019

Van Meerbeeck, C. J., Renssen, H., & Roche, D. M. (2009). How did Marine Isotope Stage 3 and Last Glacial Maximum climates differ? – Perspectives from equilibrium simulations. *Clim. Past, 5*(1), 33-51. doi:10.5194/cp-5-33-2009

Van Meerbeeck, C. J., Roche, D. M., & Renssen, H. (2011). Assessing the sensitivity of the North Atlantic Ocean circulation to freshwater perturbation in various glacial climate states. *Climate Dynamics, 37*(9), 1909-1927. doi:10.1007/s00382-011-1043-z

van Vuuren, D. P., Edmonds, J., Kainuma, M., Riahi, K., Thomson, A., Hibbard, K., et al. (2011). The representative concentration pathways: an overview. *Climatic Change, 109*(1), 5. doi:10.1007/s10584-011-0148-z

Wang, W., Lee, X., Xiao, W., Liu, S., Schultz, N., Wang, Y., et al. (2018). Global lake evaporation accelerated by changes in surface energy allocation in a warmer climate. *Nature Geoscience, 11*(6), 410-414. doi:10.1038/s41561-018-0114-8

Willmott, C. J., & Matsuura, K. (1995). Smart interpolation of annually averaged air temperature in the United States. *Journal of Applied Meteorology, 34*, 2577-2586.

Yanina, T., Sorokin, V., Bezrodnykh, Y., & Romanyuk, B. (2018). Late Pleistocene climatic events reflected in the Caspian Sea geological history (based on drilling data). *Quaternary International, 465*, 130-141. doi:https://doi.org/10.1016/j.quaint.2017.08.003

Yanina, T. A. (2012). Correlation of the Late Pleistocene paleogeographical events of the Caspian Sea and Russian Plain. *Quaternary International, 271*, 120-129. doi:https://doi.org/10.1016/j.quaint.2012.06.003

Yanina, T. A. (2014). The Ponto-Caspian region: Environmental consequences of climate change during the Late Pleistocene. *Quaternary International, 345*, 88-99. doi:https://doi.org/10.1016/j.quaint.2014.01.045

Yin, J. H. (2005). A consistent poleward shift of the storm tracks in simulations of 21st century climate. *Geophysical Research Letters, 32*(18). doi:10.1029/2005gl023684

Zhang, X., Prange, M., Merkel, U., & Schulz, M. (2014). Instability of the Atlantic overturning circulation during Marine Isotope Stage 3. *Geophysical Research Letters, 41*(12), 4285-4293. doi:doi:10.1002/2014GL060321

Supplements

S1 Supporting Information for Chapter 3

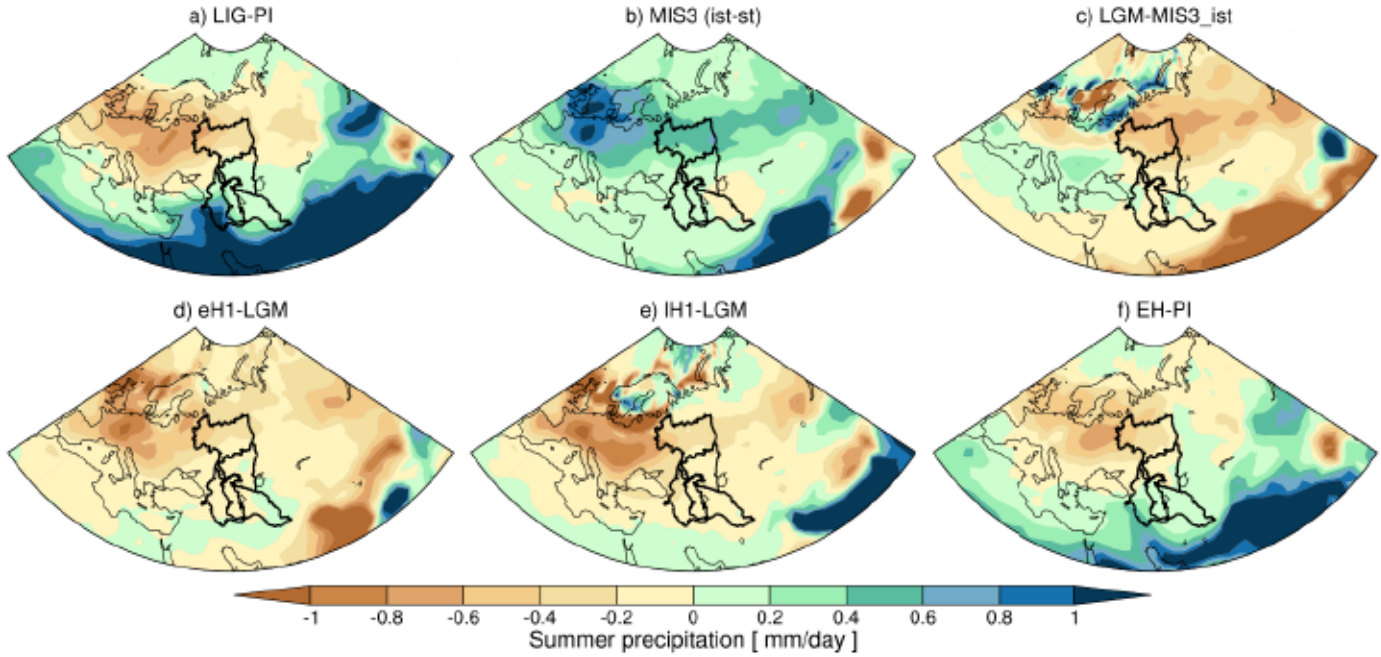

Figure S3.1: Summer mean precipitation in mm/day.

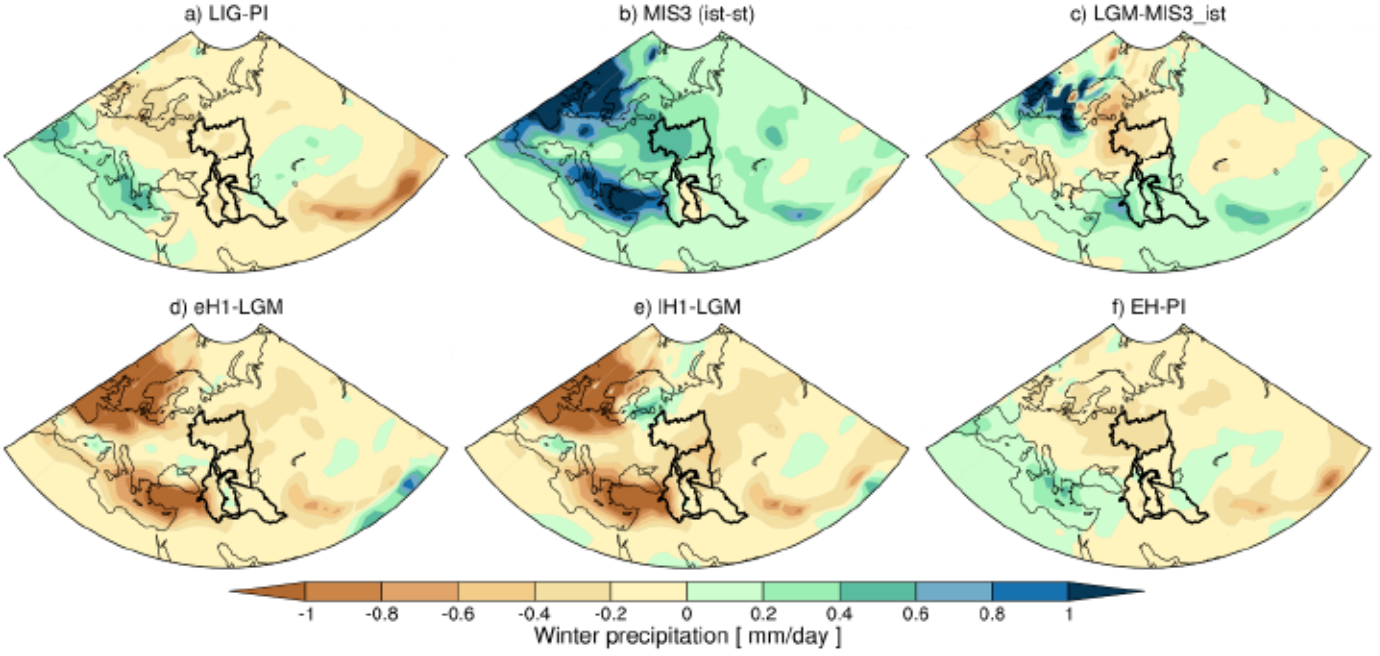

Figure S3.2: Winter mean precipitation in mm/day.

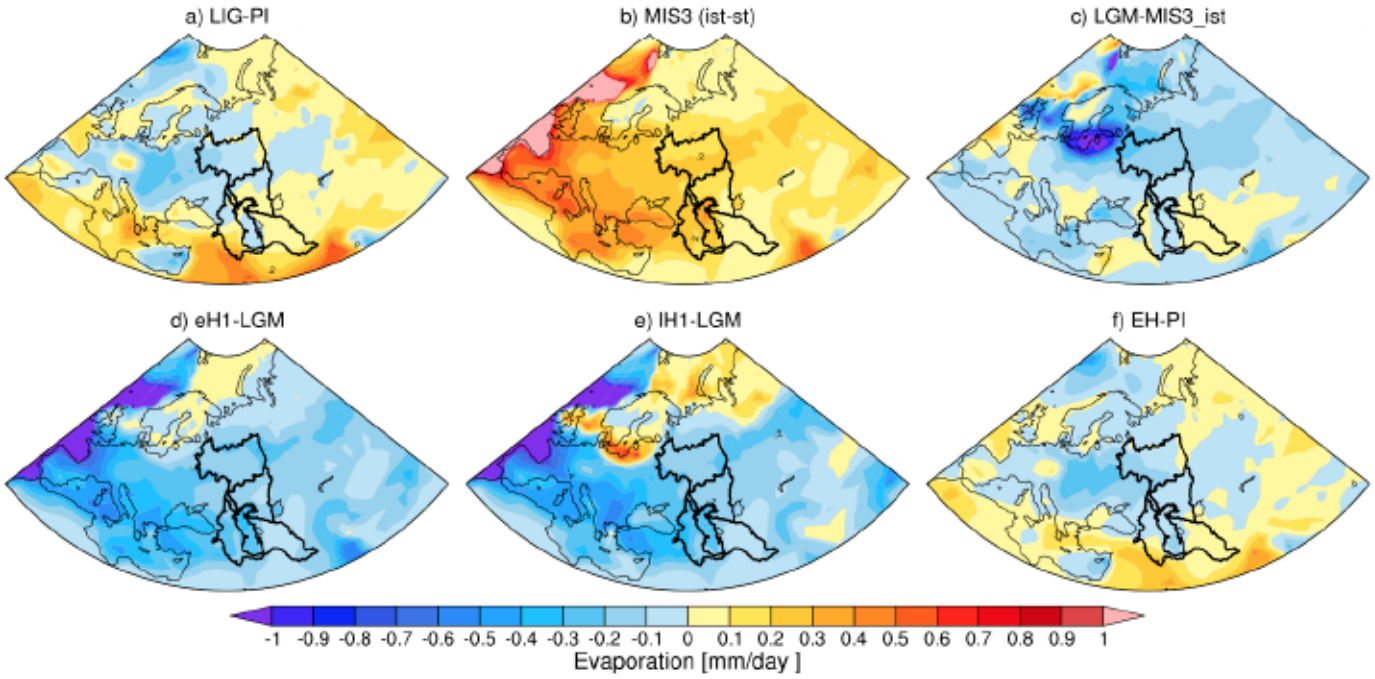

Figure S3.3: Annual mean differences in evaporation between simulations (mm/day).

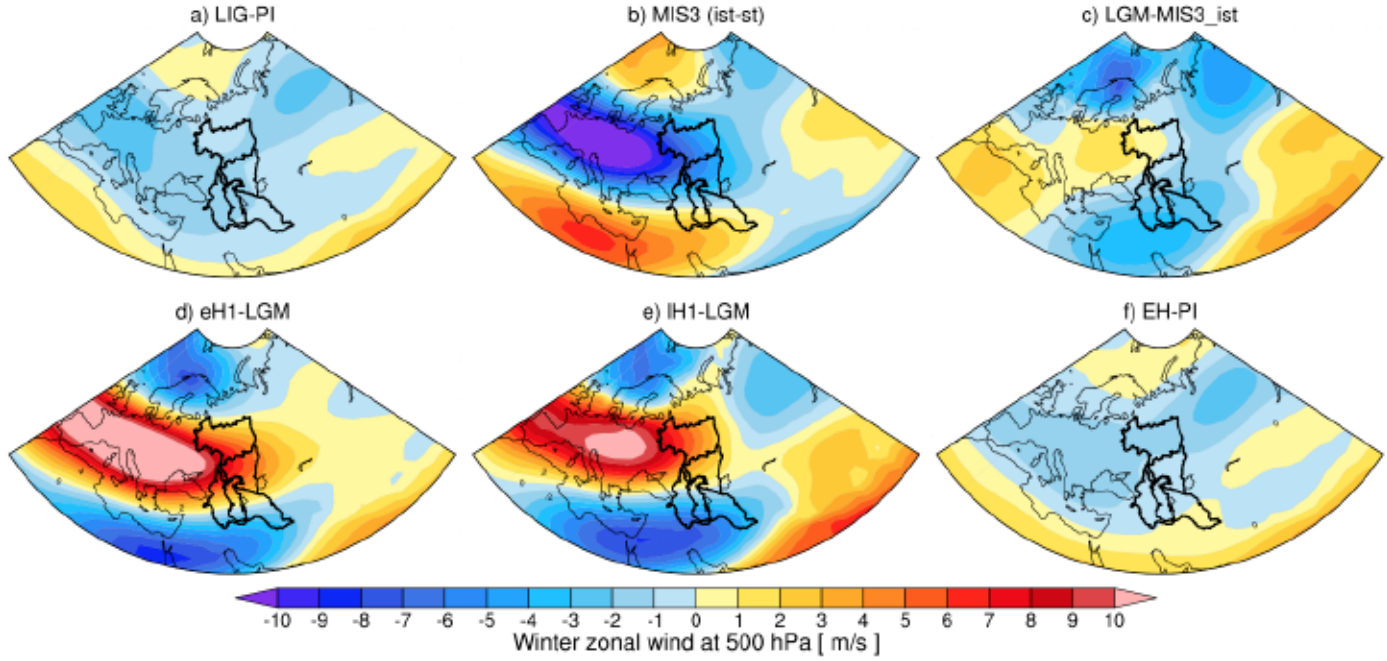

Figure S3.4: Mean winter zonal wind at 500 hPa level.

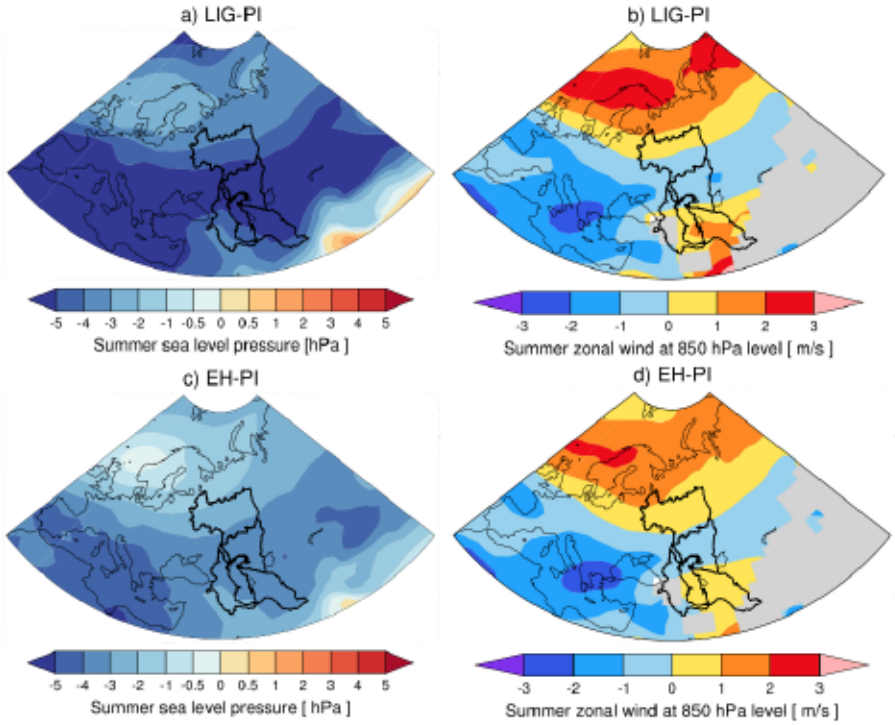

Figure S3.5: Summer mean differences in LIG minus PI conditions for a) summer sea-level pressure in hPa and b) zonal wind at the 850 hPa level and the same for (c-d) EH minus PI conditions.

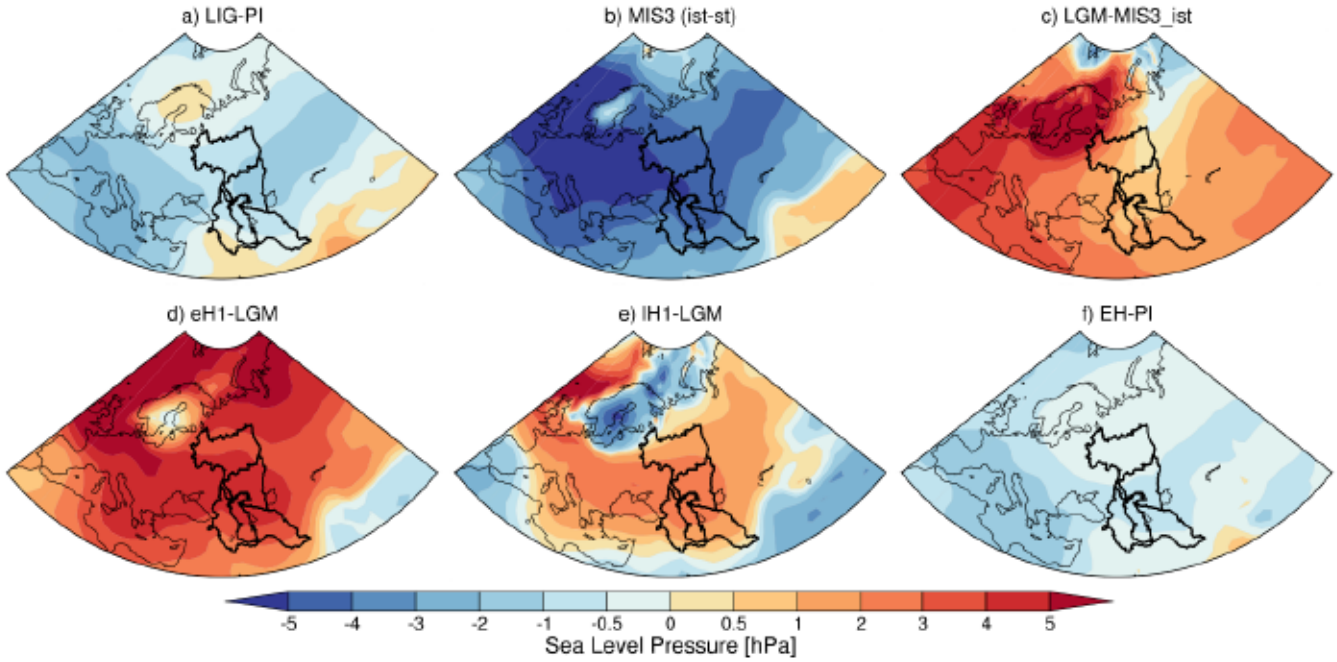

Figure S3.6: Annual mean sea level pressure in hPa.

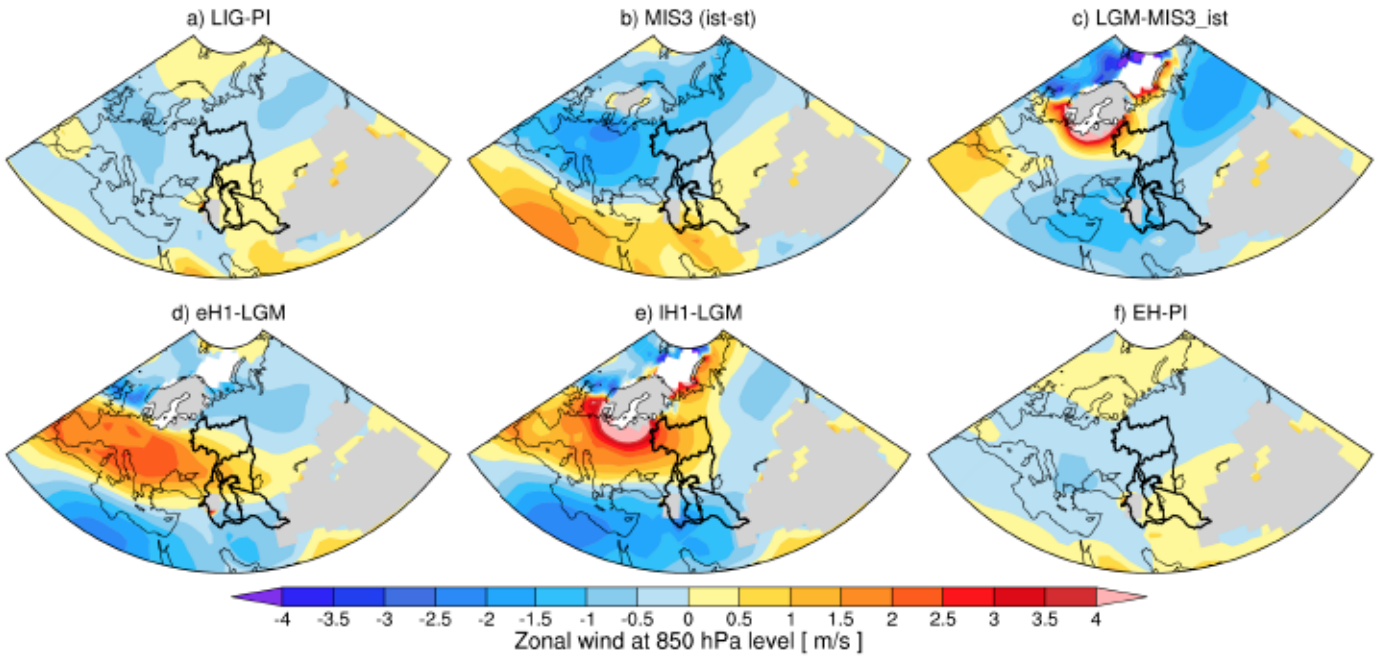

Figure S3.7: Annual mean zonal wind at 850 hPa level in m/s.

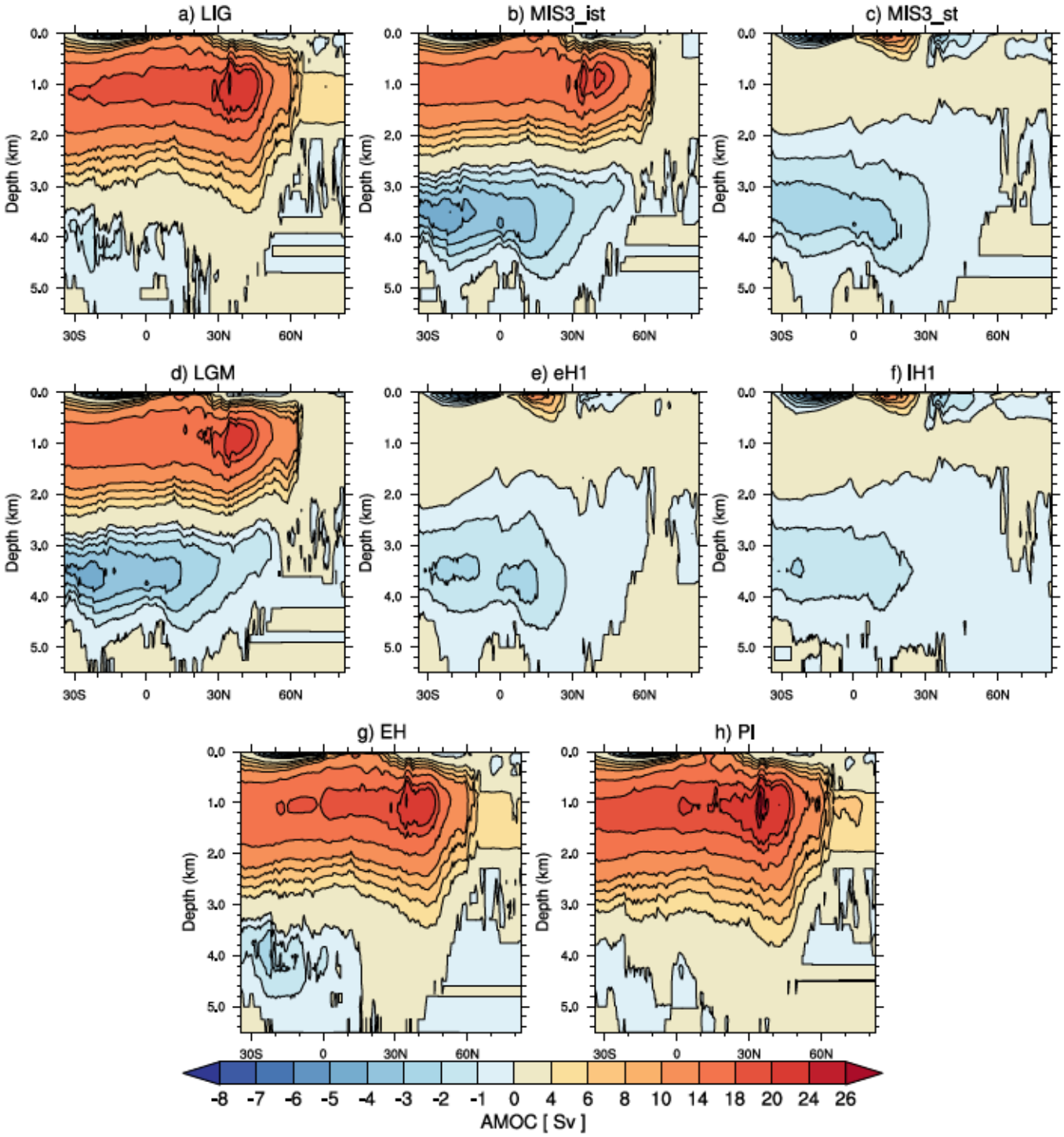

Figure S3.8: Annual mean strength of the Atlantic Meridional Overturning stream function (AMOC; Sv).

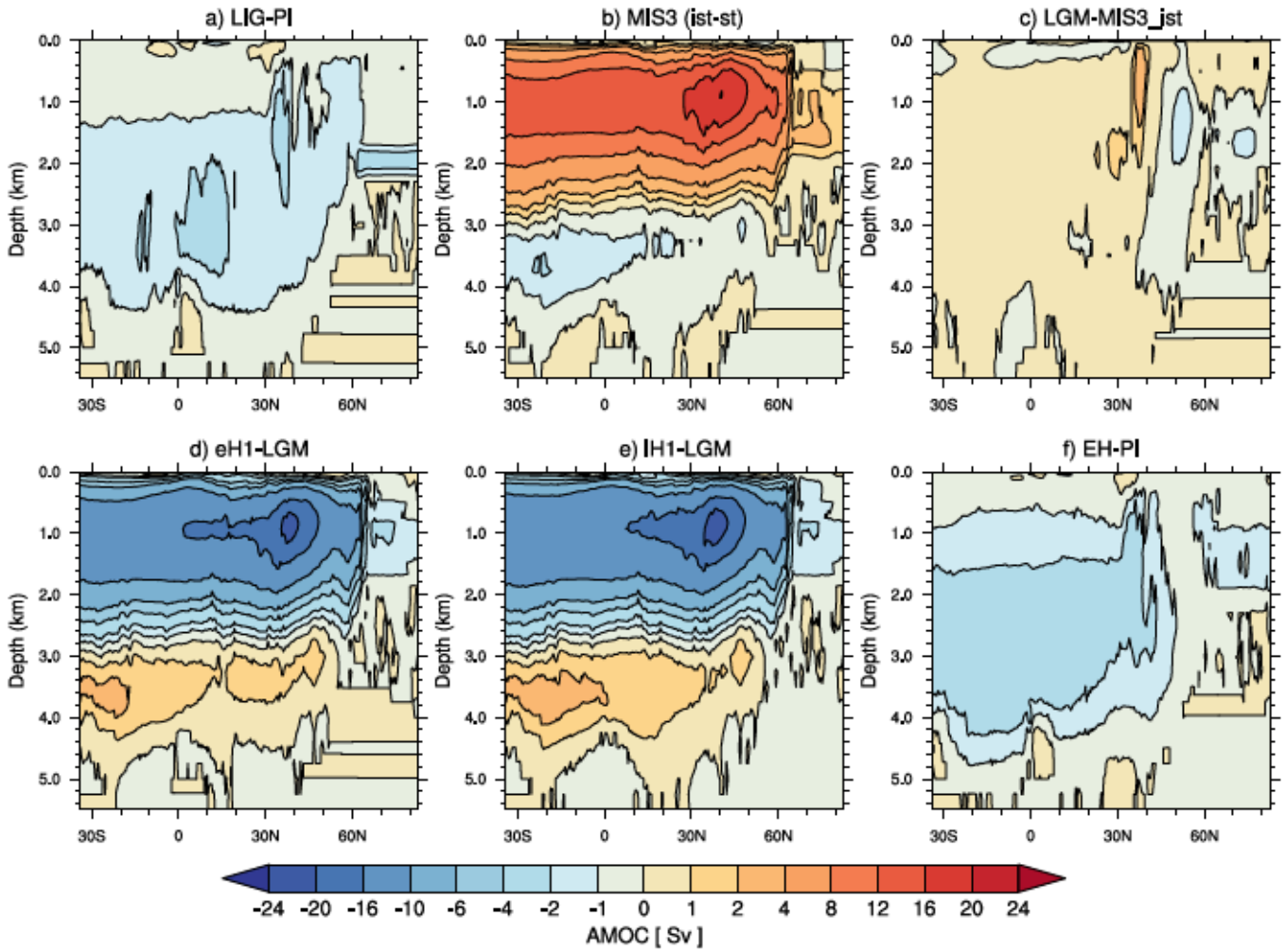

Figure S3.9: Annual mean differences between simulations the AMOC strength (Sv). The stronger AMOC under glacial conditions seen above is common in model simulations (Weber et al., 2007) and likely results from wind stress changes induced by larger ice sheets.

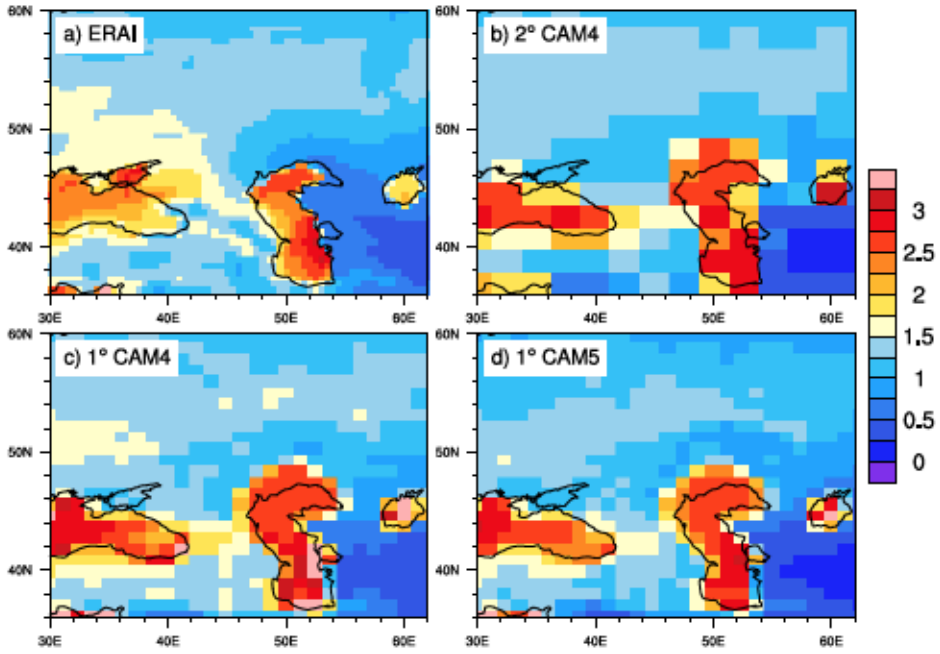

Figure S4.1: Annual mean evaporation (surface water flux) in mm/day from 1979-1999 for **(a)** 0.5° ERAI reanalysis and **(b-d)** the different CESM versions.

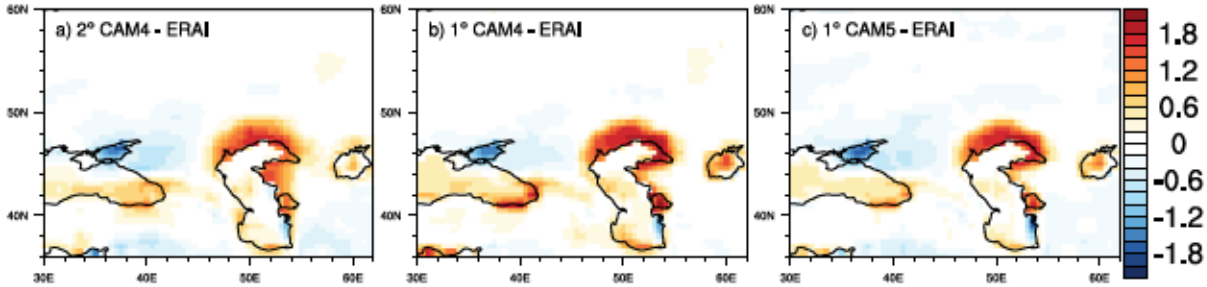

Figure S4.2: Difference in annual mean evaporation in mm/day from 1979-1999 between **(a-c)** different CESM versions and 0.5° ERAI reanalysis.

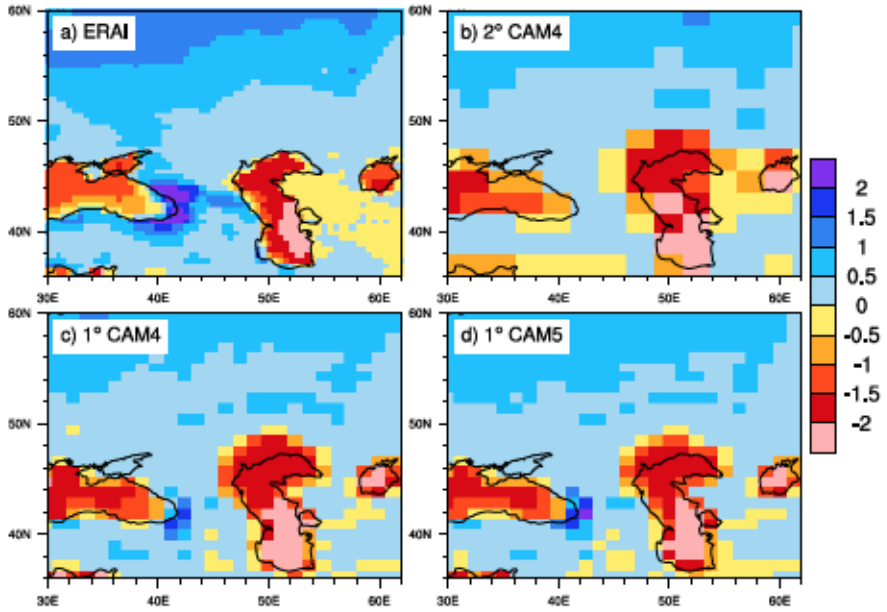

Figure S4.3: As Fig. S2.1, but for annual mean P-E in mm/day.

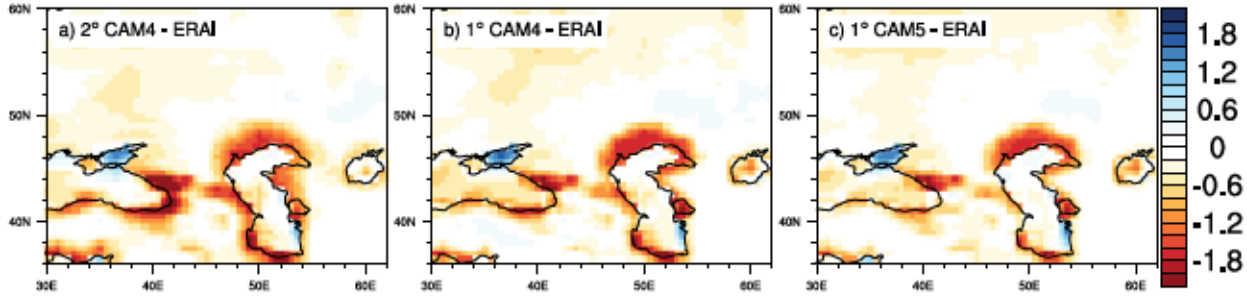

Figure S4.4: As Fig. S2.2, but for annual mean P-E in mm/day.

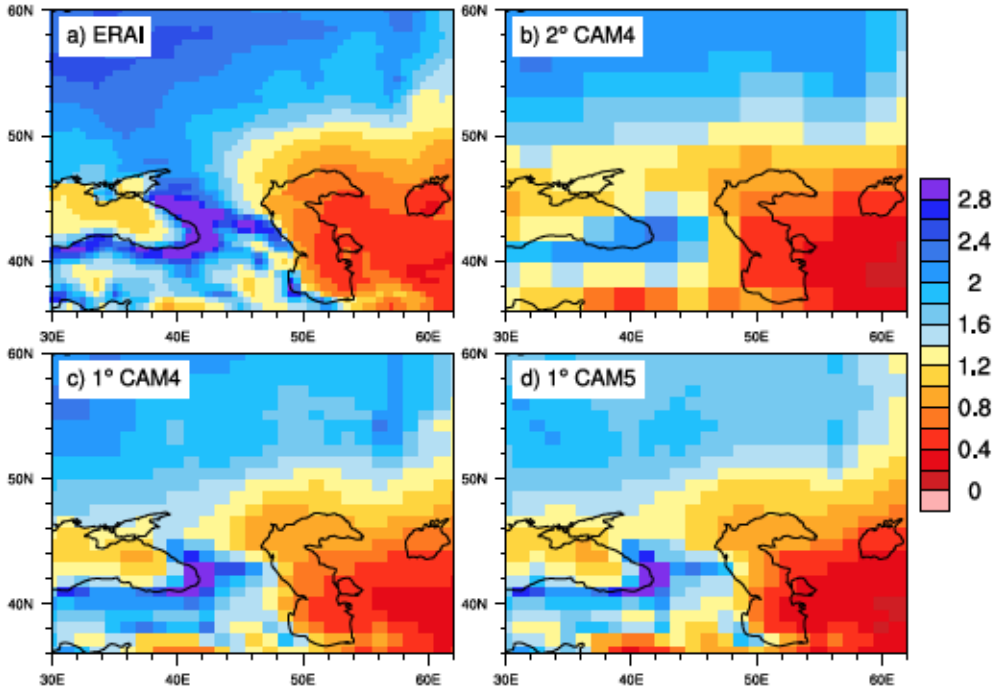

Figure S4.5: As Fig. S2.1, but for annual mean precipitation in mm/day.

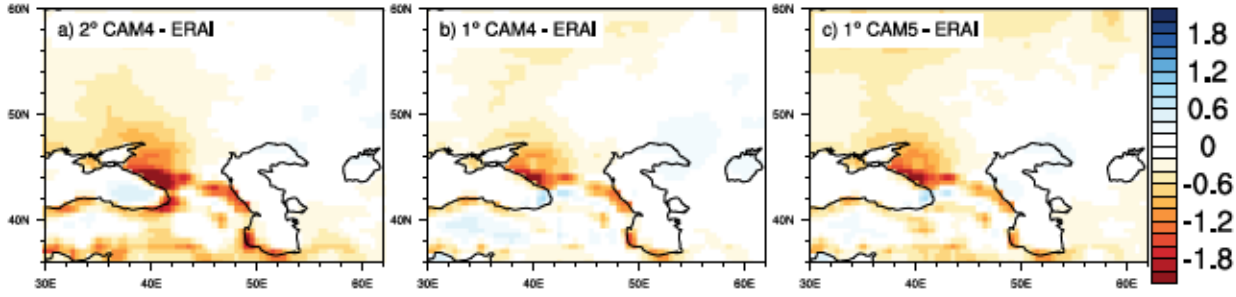

Figure S4.6: As Fig. S2.2, but for annual mean precipitation in mm/day.

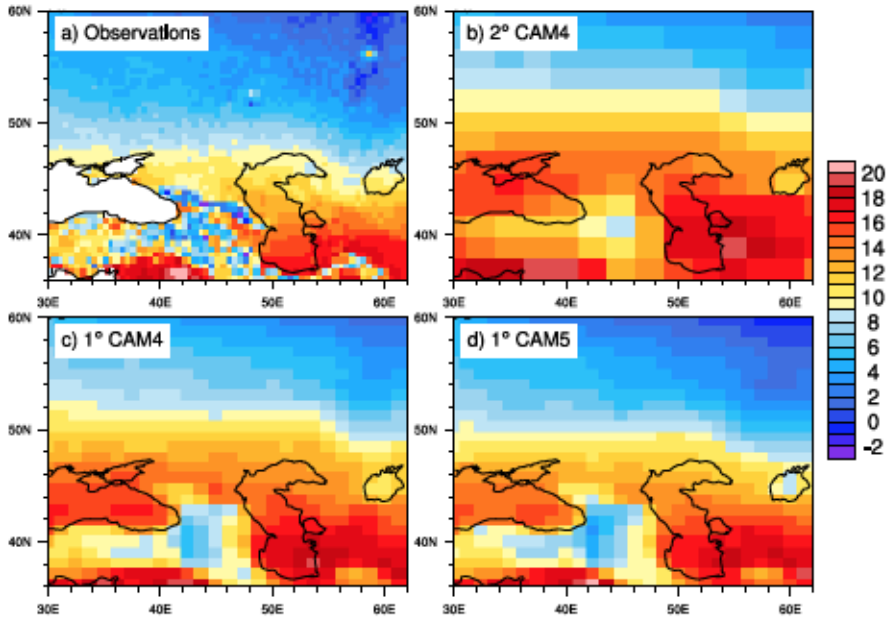

Figure S4.7: As Fig. S2.1, but for annual mean T2m in °C.

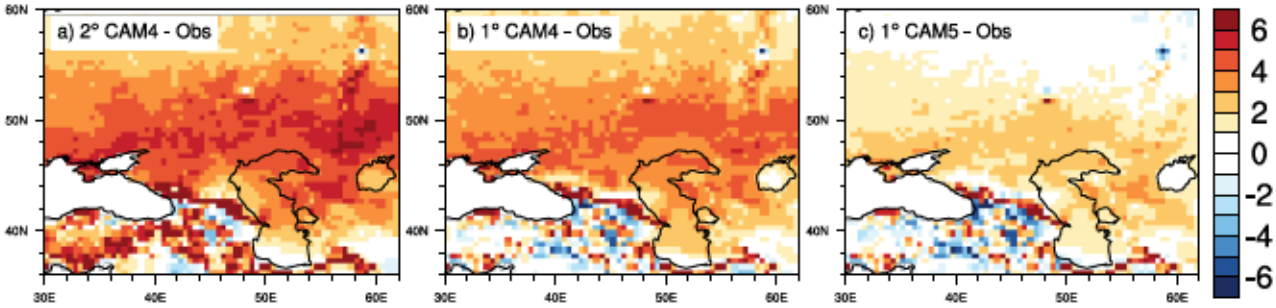

Figure S4.8: As Fig. S2.2, but for annual mean T2m in °C.

S3 Supporting Information for Chapter 5

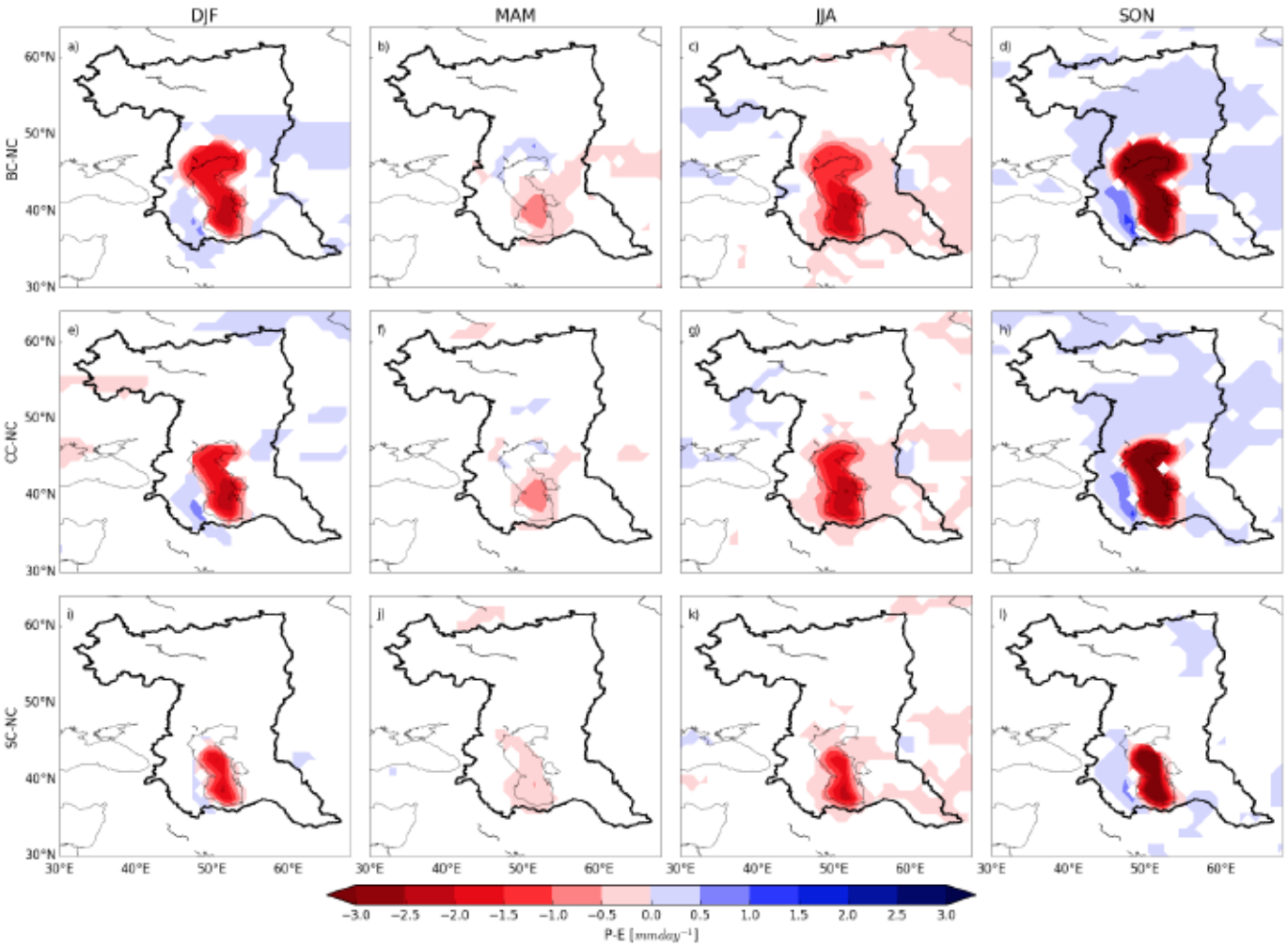

Figure S5.1: Statistically significant changes in seasonal mean P-E of large, current and small CS with respect to No-CS scenario. The shaded colours are areas were mean anomaly is different from zero with 95% confidence interval.

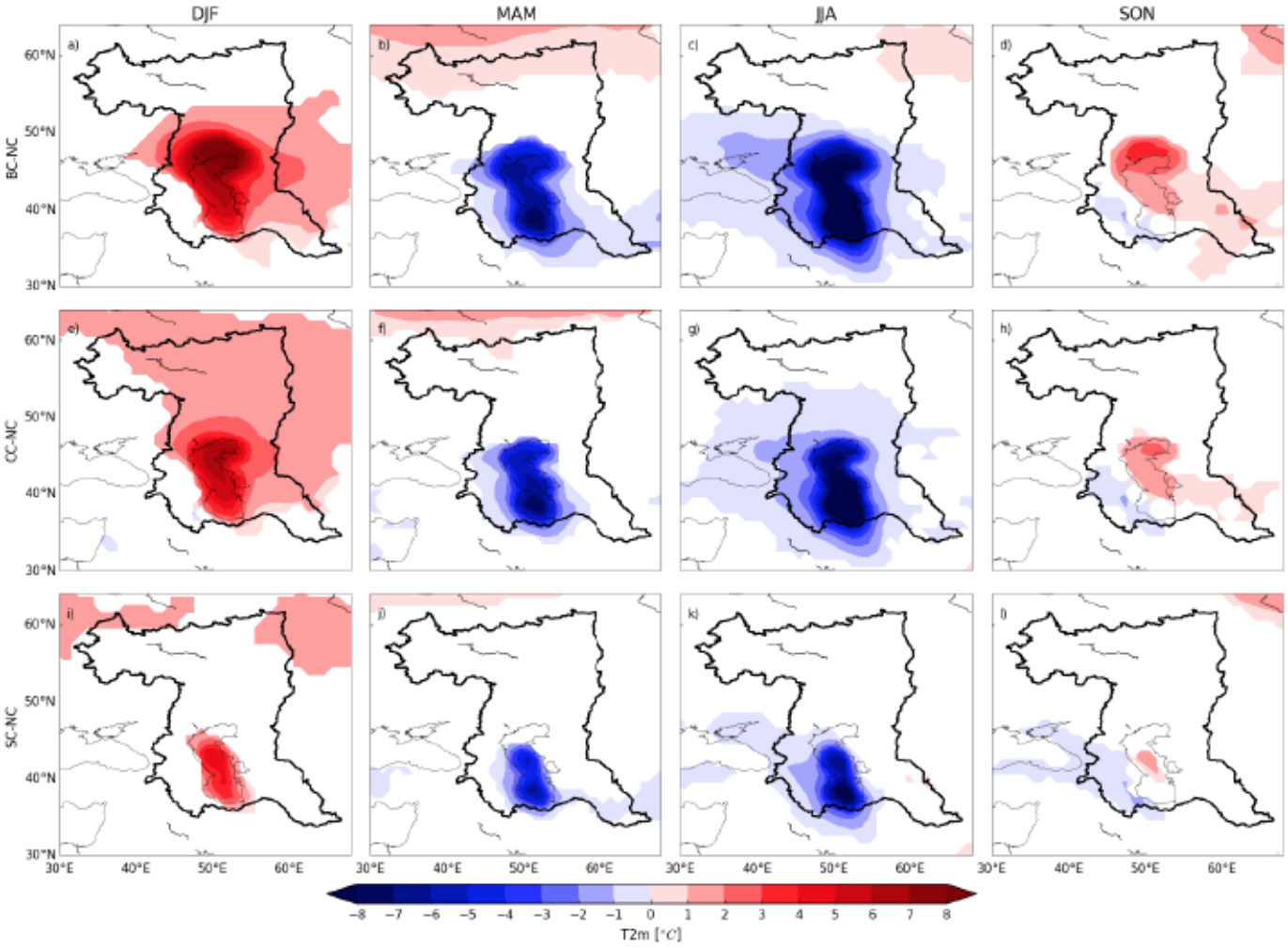

Figure S5.2: Same as Figure S5.1 but for near surface temperature changes.

Acknowledgments

First and foremost, I wish to thank my principal supervisor, Dr. Matthias Prange, for his trust and his invaluable guidance in the last years. I deeply enjoyed our sessions fuelled by your positive energy, inspiration, laughter and discussions. Heartfelt thanks are also due to Prof. Dr. Michael Schulz for ensuring the continued fruitful evolution of this thesis.

Genuine acknowledgements are due to Prof. Dr. Martin Claussen and Prof. Dr. Michael Schulz for reviewing this thesis. The entire project was completed at MARUM. Sincere appreciation goes to Prof. Dr. Klaus Arpe and Prof. Dr. Suzanne Leroy, for offering many invaluable discussions at our bi-annual Skype meetings.

This research was financed by the European Union funded Marie Curie Fellowship ITN-PRIDE project. My deepest gratitude to PRIDE for equipping me with the skills to become established as an early stage researcher in such an intense collaborative atmosphere during the past three years. I cherish the incredible experiences with network training trips to Russia, Azerbaijan, England, Netherlands, France, Germany; conferences throughout Europe (Austria, Spain) and USA and research stays in England and France. A very special thanks to my fellow PRIDE ESRs and especially to Dr. Frank Wesslingh for making this an extraordinary journey.

Andreas, I genuinely cherish our sessions of discussion filled with laughter. My gratitude goes to all members of my working group Anouk, Charlotte, Kerstin, Remi, Pepijn, Gerlinde and Ute for the rewarding discussions over my research. I am grateful to my colleague Sifan Koriche and Dr. Joy Singarayor for their support during my research stay at the University of Reading.

Ania, I deeply enjoyed our sessions of strange coffee encounters, running and yoga as well as your unending support and advice on my research. Sergei, I still remember the many times you uplifted me toward positive energy and inspiration in my darkest research times!

I am deeply indebted to my family for their support throughout my life. Most of all I especially wish to thank you, Thomas, for your endless measure of love throughout this phase.

Related co-author Publications and Contributions in the ITN-PRIDE project

A significant portion of the thesis research was carried out in the EU-funded Marie Curie Innovative Training Network focusing on raising awareness of the uniqueness of Black and Caspian Sea biodiversity and current biodiversity crises http://pontocaspian.eu/content/pride

The PRIDE (drivers of **P**onto Caspian biodiversity **RI**se and **DE**mise) project addressed these challenges through an integrated cross-disciplinary research involving all areas of natural sciences (climate, earth and bio-sciences). PRIDE encompasses a fully cohesive academic- industry training network of scientists who focuses on the evolution of the Black and Caspian lake systems and its biota over the past 2 million years to study the drivers of past and current biodiversity crisis and better understand the future biodiversity.

As part of being in the ITN-PRIDE project Cross-disciplinary training and collaborative work with other ESRs resulting in manuscripts include the following which further improved my career perspectives (working titles):

iv) Koriche, **Nandini-weiß** *et al.* (2018). Caspian lake modeling using CESM outputs for present and future climate. (in prep).

v) Koriche, **Nandini-weiß** *et al.* (2018). Caspian paleo-lake modeling using CESM outputs for past climates: Pleistocene-Holocene. (in prep).

vi) Jorissen, **Nandini-weiß** *et al.* (2019). Climate forcing of Caspian Sea-level changes during the Pleistocene under the influence of Milankovitch cycles. (in prep).

Most importantly, **I have contributed the following deliverables:** (1) snap-shot model simulations of key periods that serve as input for the Caspian Information System (PC-IS). I have contributed and fulfilled the expected deliverables from the A2 project of the ITN-PRIDE: (1) New climate simulations generate data for PC-IS; (2) P-E data to force the A3 lake model and (3) assessment of the impact of lake-surface area on regional climate. This will enable scientists, students and others interested to explore interactively the link between abiotic processes and faunal evolution in the Caspian region. All data generated from my research is prepared for the PANGAEA database (https://www.pangaea.de), and selected few for PC-IS (https://pridepcis.000webhostapp.com/sri.html) which is ready for downloading (temperature, evaporation, precipitation and precipitation minus evaporation). These climate data generated for different time slices were needed to answer the PRIDE questions; for other three ESRs in PRIDE and for PC-IS. This data contributes and answers questions regarding climate, geology and biodiversity evolution over the Caspian lake system.